Spring 2022

Testing Potential Triggering Mechanisms of Long-runout Catastrophic Rock Avalanches in the Nooksack River Basin, Whatcom County, Washington

Eric R. Brown
Western Washington University, ericbrown0027@gmail.com

Recommended Citation

Brown, Eric R., "Testing Potential Triggering Mechanisms of Long-runout Catastrophic Rock Avalanches in the Nooksack River Basin, Whatcom County, Washington" (2022). *WWU Graduate School Collection*. 1107.
https://cedar.wwu.edu/wwuet/1107

Testing Potential Triggering Mechanisms of Long-runout Catastrophic Rock Avalanches in the Nooksack River Basin, Whatcom County, Washington

By

Eric R. Brown

Accepted in Partial Completion
of the Requirements for the Degree
Master of Science

ADVISORY COMMITTEE

Dr. Douglas Clark, Chair

Dr. Robert Mitchell

Dr. Allison Pfieffer

GRADUATE SCHOOL

David L. Patrick, Dean

Master's Thesis

Eric R. Brown

May 26, 2022

Testing Potential Triggering Mechanisms of Long-runout Catastrophic Rock Avalanches in the Nooksack River Basin, Whatcom County, Washington

A Thesis
Presented to
The Faculty of
Western Washington University

In Partial Fulfillment
Of the Requirements for the Degree
Master of Science

by
Eric R. Brown
May 2022

Abstract

The Nooksack River basin in northwest Washington State contains a suite of five large long-runout rock avalanche deposits. Similarities in the deposits (i.e., volume, runout distance, H/L, and for four lithology) and their spatial proximity suggest that they may also share a common triggering mechanism. Two of the deposits, the Van Zandt Landslide Complex (VZLC) and the Church Mountain Sturzstrom (CMS) have published emplacement ages (1330-1270 cal. yr B.P. and 2700-2150 cal. yr B.P., respectively) that overlap with known regional or local prehistoric earthquake events, suggesting seismicity may be the cause. To test this idea further, I conducted detailed field- and lidar-based mapping to estimate the volume, surface area, runout distance, height-to-length ratio (H/L), and thickness of each deposit. Additionally, I attempted to determine the emplacement timings for the remaining three undated or poorly dated deposits (Racehorse Creek, Middle Fork, and Maple Falls). To establish ages for the slides, I used a combination of radiocarbon (^{14}C) dating of basal organics contained in sediment cores from bogs in the debris fields and cosmogenic radionuclide (CRN) exposure dating of large boulders in the debris fields (CRN ages are converted to “yr B.P.” to conform with calibrated ^{14}C dates).

Dating results indicate that there are at least five separate collapse events recorded within the debris fields of the three landslides. The most reliable new age constraints for the single-event Racehorse Creek deposit (5080 ± 1130 yr B.P., 4290 ± 1750 yr B.P., and 3800 ± 900 yr B.P.) are consistent with the previously published age estimate of Pringle et al. (4420-3990 cal. yr B.P.). The Middle Fork landslide debris field appears to record two separate events. Both ^{14}C constraints (10,170-9690 cal. yr B.P.) and CRN ages (7640 ± 1300 yr B.P. and 9230 ± 1400 yr B.P.) indicate that Middle Fork Event 1 is older than ~10 ka. CRN ages from the upper part of the debris field indicate that the age for Middle Fork Event 2 is 3600 ± 900 yr B.P. The Maple Falls landslide has at least two debris lobes occurring 3370 ± 740 yr B.P. for Event 1 and 630 ± 400 yr B.P. for Event 2.

The preponderance of evidence indicates that most likely triggers for these slides are (1) seismicity related to large magnitude earthquakes, (2) heavy rainfall events or prolonged precipitation, or (3) glacial debuttressing. All of the dated landslide events in this study overlap in time with one or more known Cascadia Subduction Zone (CSZ) earthquakes or ruptures of the nearby Boulder Creek fault; however, the relatively large dating uncertainties preclude confidence in these correlations. Because no detailed Holocene paleoclimate proxy records exist for the area, precipitation triggering remains an equally viable mechanism. Glacial debuttressing is a potential trigger for the oldest (Middle Fork) deposit, but a 4 kyr gap between deglaciation and the minimum age for the deposit suggests this mechanism is less likely than the options above. Furthermore, the fact that all the other deposits formed after ~5 ka clearly indicate that debuttressing is not a dominant mechanism. Other possible triggering mechanisms (e.g., eruptions of Mt. Baker, fluvial undercutting) are even less likely based on the age constraints and geographic setting of the source zones.

In summary, my mapping and dating results indicate that the most likely triggers for these landslides were either earthquakes or heavy precipitation events. The fact that all the landslides occur in a relatively narrow belt and all overlap with known earthquakes suggests that earthquakes are likely responsible for at least some of these failures. Furthermore, my results indicate that CRN exposure dating of large boulders in debris fields of such landslides can be a viable method of determining their timing of emplacement. More extensive dating of these deposits, both CRN exposure dating of boulders and opportunistic ^{14}C dating of organics in the slide deposits, may allow my results and interpretations to be refined and expanded.

Acknowledgements

I want to thank everyone who helped make this research possible, particularly those who assisted me with fieldwork: Spencer Winter, Kass Ulmer, Aiden Burdick, Alex Hernandez, Geoff Malick, and Greg Morrow. I owe thanks to Chantel Jensen who assisted me with establishing a method to calculate landslide volumes. Also, a big thank you Whatcom County Geologist Andy Wiser for assisting me with sediment coring and helping to improve my understanding of the local geology. Thank you to the Washington State Department of Natural Resources for allowing me access to several of my field sites located on state timber lands. I also want to acknowledge Sierra Pacific Industries for granting me permission to access to their property to investigate the Middle Fork landslide deposit.

Thank you to my advisor, Dr. Douglas Clark, who has assisted me with many aspects of my project, helped to improve my writing, and expanded my critical thinking skills as a geologist during my time at WWU. Thank you to my committee members, Dr. Allison Pfieffer and Dr. Robert Mitchell, who provided valuable insights and feedback on many drafts of this thesis. Also thank you to Ben Paulson at WWU’s Geology Department for technical support with various laboratory and project-related equipment. Thank you to Lee Corbett and Paul Bierman of the University of Vermont – Community Cosmogenic Facility in helping to process my CRN samples and for assisting me with questions related to cosmogenic dating.

Finally, I want to thank my wife, Rebecca, who has provided me with unwavering love and support throughout the duration of this project and for accompanying me on many of my outings to the landslides.

Funding for this research is provided by the National Science Foundation sponsored Awards for Geochronology Student Research (NSF-AGeS2) program, the Geological Society of America (GSA), the Northwest Scientific Association (NWSA), Western Washington University Research and Sponsored Programs (WWU-RSP), and Western Washington University’s Geology Department.

Table of Contents

List of Tables and Figures

List of Abbreviations

2-σ	2-sigma uncertainties
^{10}Be	beryllium-10
^{14}C	Carbon-14 (Radiocarbon)
B.P.	Before Present (1950)
ca.	circa
cal yr B.P.	calibrated years before present
CMS	Church Mountain Sturzstrom
CRN	Cosmogenic Radionuclide
CSZ	Cascadia Subduction Zone
DDMF	Darrington-Devils Mountain Fault
DEM	Digital Elevation Model
Fig.	figure
g	acceleration of gravity (9.8 m/s^2)
GEER	Geotechnical Extreme Events Reconnaissance
GPS	Global Positioning System
H/L	height to length ratio
ka	kilo annum (thousand years ago)
LIDAR	Light Detection and Ranging
Ma	mega annum (million years ago)
MF	Maple Falls landslide
MFN	Middle Fork Nooksack landslide
M_w	Moment Magnitude
PGA	Peak Ground Accelerations
PRIME	Purdue Rare Isotope Measurement Laboratory
RHC	Racehorse Creek landslide
SI	Supplemental Image
SEM-EDX	Scanning Electron Microscopy – Energy Dispersive X-ray Spectrometery
SR-520	State Route 520
WA	Washington State
WA DNR	Washington Department of Natural Resources
WGS	Washington Geological Survey
WWU	Western Washington University
USGS	United States Geological Survey
UVM-CCF	University of Vermont – Community Cosmogenic Facility
VZLC	Van Zandt Landslide Complex
yr	year

1.0 INTRODUCTION

The hazard presented by large, long-runout landslides was recently exemplified by the deadly SR-530 landslide near Oso, WA, on March 22, 2014 (43 fatalities). This loss of life has driven substantial scientific (e.g., The GEER Report; Keaton et al., 2014; Iverson et al., 2015; Wartman et al., 2016), legal (Larsen, 2015), and legislative (WA State Bill 5088, 2015) attention. The Oso disaster spurred a statewide effort to characterize and catalog the distribution of landslides throughout the state. Although most effort thus far has focused on slides initiated in unconsolidated glacial sediments, such as those at Oso (e.g., Shallow Landslide Hazard Forecast Map; WA DNR, 2014), relatively little attention has been given to possible triggering mechanisms associated with catastrophic rock avalanches.

The Nooksack River basin in central Whatcom County contains a notable concentration of large, long-runout rock avalanches (Fig. 1). Rock avalanches are large (>10^6 m^3), sudden rock slope failures characterized by rapid velocities and long-runout distances (Cook, 2017). Numerous residences and communities in the Nooksack Basin sit on or near the debris fields of these slides, presenting significant exposure to possible future failures.

The abundance of these slides in such a small geographic area suggests the potential for a common triggering mechanism. For example, the youngest two debris lobes of the Van Zandt Landslide Complex (VZLC; Fig. 5) collapsed nearly simultaneously (within 2-σ dating uncertainties) between 1330-1285 cal. yr B.P. (Malick, 2018). This timing overlaps with that of a known Cascadia megathrust (M_w > 9.0) earthquake (event T4; Goldfinger et al., 2012). Another nearby rock avalanche deposit, the Church Mountain Sturzstrom (CMS; Carpenter, 1993; Pringle, 1998), is less well dated but may also overlap with an earlier Cascadia earthquake (event T6; Goldfinger et al., 2012). However, because of dating uncertainties and the fact these deposits record effectively only two landslide events (two simultaneous at Van Zandt, and a separate one at Church Mountain), coincidence cannot be ruled out and triggering mechanisms other than seismic remain viable options.

In this study, by constraining the emplacement timing of the three undated rock avalanche deposits (Racehorse Creek, Middle Fork, and Maple Falls; Figs. 1, 2, 3, and 4, respectively), I test whether ground accelerations related to large paleoseismic events are a likely triggering mechanism for these catastrophic failures, or whether other mechanisms (e.g., precipitation, erosional debuttressing, or others) must be invoked. If large paleoseismic events are the dominant trigger, most or all of the collapse ages obtained from these landslides should overlap with major events from the Cascadia Subduction Zone (CSZ) (Fig. 6; Goldfinger et al., 2012) or from local crustal faults such as the Boulder Creek Fault (Sherrod et al., 2013) or the Birch Bay Fault (Kelsey, 2012). If these landslides were triggered by other mechanisms, collapse dates should display different temporal patterns. For example, collapses associated with late-Pleistocene glacial debuttressing should cluster towards the beginning of glacial recession, whereas collapses related to either fluvial undercutting or precipitation events should present a more stochastic temporal pattern (e.g., Fischer et al., 2010; Yin et al., 2011; LaHusen et al., 2020).

The primary objectives of this research are to (1) characterize the morphology and map the extent, source zone, and volume of each landslide, (2) determine the collapse age of each deposit using a combination of ^{14}C dating and ^{10}Be-CRN exposure dating, and (3) compare the collapse ages with the dates of known large earthquakes originating from the CSZ and nearby crustal faults in order to determine potential earthquake triggering mechanisms of the large rock avalanche deposits in the Nooksack basin.

2.0 BACKGROUND

2.1 Catastrophic Rock Avalanches

Landslides are defined as the movement of a mass of rock, soil, or debris, down a slope under the influence of gravity (Valagussa, 2019). They can be categorized based on the type of material involved (rock or soil), the velocity of movement, and the nature of the failure surface (e.g., rotational, planar; Varnes, 1978; Hungr et al., 2014). They can be slow and gradual, occurring over tens or hundreds of years, or nearly instantaneous, failing in a matter of minutes or seconds.

This study focuses on a specific subset of landslides, catastrophic long-runout rock avalanches, sometimes referred to as *Sturzstroms* (literally "fall-stream" in German; Heim, 1932; Hsü, 1975). To be considered "catastrophic" a landslide must initiate suddenly, have a high velocity (100–250 km/h), and possess a large volume (>10^6 m^3) of rock debris (Hewitt et. al., 2008). "Long-runout" describes higher-than-expected mobilities and runout distances (typically five to ten times the total fall height; Hewitt et al., 2008) that results in a debris field that extends horizontally much further than would be expected from a slide experiencing a normal coefficient of friction (Hsü, 1975). This phenomenon led Heim (1932) to the realization that an inverse relationship exists between rock avalanche volume and friction, with larger slides possessing a lower coefficient of friction (~0.3) and smaller slides (<0.5 x 10^6 m^3) possessing a more normal friction coefficient (~0.6). Hypotheses to explain the kinematics responsible for these longer than expected runouts are still widely debated (e.g., Hungr and Evans, 2004; De Blasio and Elverhøi, 2008; Johnson et al., 2016), but include acoustic fluidization (Melosh, 1979), vaporized pore water (Habib, 1975; Goguel, 1978), and dispersive forces (Hsü, 1975).

2.2 Study Area and Previous Work

The Nooksack River basin in the western foothills of the North Cascades preserves five large (each >10^6 m^3) catastrophic rock avalanche deposits along State Route 542 (Mount Baker Hwy) ~25 km east of Bellingham, WA (Fig. 1). These include the Van Zandt Landslide Complex (VZLC), the Church Mountain Sturzstrom (CMS), and the Racehorse Creek, Middle Fork, and Maple Falls landslides (Carpenter, 1993; Pringle et al., 1998; Malick, 2018; Mickelson et al., 2020). Previous WWU graduate students have studied two of these five deposits: Malick (2018) characterized and dated the two younger lobes of the VZLC, and the CMS was described and dated by Carpenter (1993).

The VZLC (Fig. 5) is characterized by three distinct crosscutting debris lobes each composed of Chuckanut Formation sandstone debris. Malick (2018) quantified the volumes of each of the three debris lobes (Debris Lobe 1 = 16.7 x 10^6 m^3; Debris Lobe 2 = 51.4 x 10^6 m^3; Debris Lobe 3 = 6.5 x 10^6 m^3), totaling 74.8 x 10^6 m^3 for the whole complex. Radiocarbon dating of in-situ logs and woody debris embedded and preserved in basal sediments of several natural and human-made exposures, along with twigs in sediment cores from several small bogs formed on the debris lobes, constrained the ages of the two younger debris lobes to 1330-1285 cal. yr B.P. for lobe 2 and 1300-1285 cal. yr B.P. for lobe 3 (Malick, 2018). These age ranges overlap with the age of a megathrust earthquake (event T4) from the CSZ (Fig. 6; Goldfinger et al., 2012), suggesting that seismicity may have triggered the rock avalanche.

The town of Glacier, WA, ~30 km upstream from the VZLC along the North Fork Nooksack River, is largely built on top of the debris field of the Church Mountain Sturzstrom deposit. In contrast to the other rock avalanche deposits in the basin, the CMS involves Paleozoic metasedimentary rocks of the Chilliwack Group and Mesozoic marine sedimentary rocks of the Nooksack Formation (Carpenter, 1993). Extensive exposures in slide debris formed by contemporaneous flooding along the Nooksack River allowed Carpenter (1993) to quantify the geometry, calculate a total volume of slide debris, and sample datable organic material related to initial landslide emplacement. Carpenter estimated the total original slide volume to be ~280 x 10^6 m^3 based on the areal extent of the debris field and the average thicknesses of multiple exposures. She also collected and radiocarbon-dated two separate in-situ logs buried within the landslide deposit that yielded age ranges of 2725-2350 and 3060-2710 cal. yr B.P. The former date overlaps with CSZ event T6, while the latter does not (Goldfinger et al., 2012). Pringle et al. (1998) subsequently dated the outer rings of two logs embedded in CMS debris, each yielding date ranges of 2700-2150 cal. yr B.P. (2-σ), consistent with CSZ event T6 (Goldfinger et al., 2012).

Of the three remaining rock avalanche deposits in the Nooksack River basin (Racehorse Creek, Middle Fork, Maple Falls) only Racehorse Creek has published descriptions or age control (Moen, 1962; Kovanen, 1996; Dragovich, 1997; Pringle, 1998). Pringle et al. (1998) provide a brief description of the deposit and a single limiting age of 4420-3995 cal. yr B.P. (2-σ). This age was on a cedar log embedded in a silty sand layer ~20 cm below the basal contact of the landslide deposit; it therefore represents a maximum limiting age for the landslide. Pringle et al. (1998) argued that irregular oxide staining in the silt between the log and the overlying landslide deposit represents soil disturbances during landslide emplacement, concluding that the tree was moved and buried by landslide runout. If borne out by subsequent dating, this interpretation would indicate that the log provides a direct date of the slide, rather than a limiting date. Engebreston et al. (1996) estimated the volume of the Racehorse Creek deposit as 2.5 km^3

(2.5×10^9 m^3); this estimate, however, appears to be a significant overestimate (by several orders of magnitude) based on comparison to Malick's more rigorous lidar-based volume estimate for the similarly extensive VZLC complex (74.8×10^6 m^3).

2.3 Geologic History

The geologic source material for the Racehorse Creek, Middle Fork, Maple Falls, and Van Zandt landslide deposits, is the Chuckanut Formation. This Eocene age (~45-55 Ma; Mustoe et al., 2007) deposit is described as a thickly bedded arkosic sandstone unit interbedded with thinner layers of conglomerate, shale, mudstone, and coal (Johnson, 1984; Mustoe et al., 2007). Throughout the late-Eocene, the Chuckanut Formation was extensively folded and faulted by east-west compression resulting in a series of steeply dipping (45˚-75˚) N-NW trending anticlines (Badger, 2002). The high degree of tectonic strain experienced by this Formation has left it extremely vulnerable to failure because mechanically weak bedding planes (i.e., shale and coal layers) and persistent jointing fractures provide abundant failure planes and lateral release surfaces for sliding to occur (Badger, 2002).

Throughout the Pleistocene, the Nooksack River basin was repeatedly overrun and heavily scoured by both alpine glaciers and the Cordilleran ice sheet (Porter and Swanson, 1998; Booth et al., 2003; Riedel et al., 2007; Clark and Clague, 2021). Ice thicknesses here are estimated to have reached up to 1600 m during the maximum extent of the Puget ice lobe ca. 15 ka (Porter and Swanson, 1998). Extensive erosion related to these advances carved deep valley floors and oversteepened valley walls (McColl, 2012). Upon deglaciation, this oversteepening can destabilize hillslopes by increasing the shear stresses acting on a slope (McColl, 2012).

2.4 Triggering Mechanisms

Landslides are activated by a wide variety of natural and anthropogenic processes. These processes are more commonly referred to as triggering mechanisms (Highland and Bobrowsky, 2008). A trigger is defined as any external forcing that results in the sudden release of rock or soil either by increasing the shear stress on or reducing the shear strength of slope materials beyond a certain threshold (Wieczorek, 1996). Common triggering mechanisms include ground accelerations generated by large magnitude earthquakes, increases in pore-water pressure and slope mass due to heavy precipitation, and glacial or fluvial debuttressing of hillslopes. Because this study considers landslide deposits that precede large-scale industrial activities (e.g., logging or mining) in western Washington, anthropogenic causes are not considered.

2.4.1 Seismic Triggering

Ground accelerations related to earthquakes have long been understood as a potential trigger for landslides (Keefer, 1984; Kramer, 1996). Seismogenic shock waves travel through bedrock and propagate until their energy eventually dissipates. Hillslope failure may occur due to initial or peak ground accelerations as seismic waves pass through a region, or as the result of rapid substrate weakening due to rock mass fracturing (Harp and Jibson, 1996; Meunier et al., 2007; Lin et al., 2008). Furthermore, steep topography has the potential to amplify seismic waves from an earthquake. During the 1994 Northridge, CA, earthquake ($M_w = 6.7$), seismometers at the top of the ridge above Pacoima Canyon recorded larger peak ground accelerations (1.58g) than those located in the surrounding area and bottom of the canyon (0.50g) (Sepúlveda et al., 2005). This effect may also have influenced the source zones for the rock avalanches in the Nooksack basin, all of which extend to the local ridgelines.

Landslide response to earthquakes originating from shallow crustal faults typically scales with increasing magnitude and inverse distance from the epicenter (Keefer, 1994), but large subduction zone earthquakes appear to produce a more variable response. Two such subduction zone earthquakes, the 2011 Tohoku earthquake (M_w 9.0; Wartman et al., 2013) and the 1960 Chilean earthquake (M_w 9.5; Veblen and Ashton, 1978), resulted in considerably different responses of landslides in their respective regions. The Tohoku earthquake produced 18×10^6 m^3 of landslide debris whereas the Chilean earthquake produced thousands of times that amount (Perkins et al., 2018). This difference suggests that the incidence of coseismic landslides in response to subduction zone earthquakes is dominantly influenced by other variables (e.g., local lithology, distance to epicenter, offshore dampening, and antecedent hydrologic conditions). For example, the relative lack of wide-spread landslides related to the 2001 Nisqually earthquake (M_w 6.8; McDonough, 2002; Highland, 2003), which occurred during an unusually dry winter, demonstrates the importance of antecedent precipitation on landslide susceptibility.

2.4.2 Precipitation Triggering

Another common cause of landslides is excess precipitation, especially on the western slopes of the North Cascades where abundant rain and snow is prevalent during most winters (Mock, 1996). Precipitation triggering occurs when a hillslope fails as a result of a high flux of water to the subsurface. Large quantities of water filling pore spaces and fractures in rock or soil can add a significant amount of mass to a slope, increasing the forces that drive failure. Water can also destabilize slopes by imparting a buoyancy force between individual grains in the subsurface. This added water results in a reduction of friction and cohesion and can thereby reduce the shear strength of the slope material. Precipitation events that have the potential to provide abundant amounts of water to the subsurface include atmospheric river systems, rain-on-snow events, and sustained precipitation (Fischer et al., 2010; Yin et al., 2011; Marc et al., 2019).

Precipitation triggering is predominately correlated with shallow landslides in unconsolidated sediments or soils (e.g., Crozier, 1986; Crosta and Frattini, 2001; Roccati et al., 2019). In the Pacific Northwest, where shallow landslides are common (especially during the rainy winter months), few studies have focused on the potential for precipitation to trigger deep-seated bedrock landslides such as those in the Nooksack River basin. One study that has assessed this possible relationship (LaHusen et al., 2020) compares the timing of deep-seated bedrock landslides in the Oregon Coast Range to mean annual precipitation and the occurrences of subduction zone earthquakes over the past 1,000 years. They determined that whereas landslide frequency correlated with precipitation, it did not correlate with modeled peak ground accelerations or distance from the epicenter (LaHusen et al., 2020); they thus concluded that precipitation may play a significant role in the failure of these bedrock landslides.

2.4.3 Glacial and Fluvial Debuttressing

Another potential triggering mechanism is the erosional debuttressing of hillslopes following deglaciation. Debuttressing is described as the removal of resisting, or slope-stabilizing forces either by anthropogenic or natural processes (Highland and Bobrowsky, 2008). For the landslides in this study potential debuttressing processes include: (1) glacial scour followed by rapid deglaciation and (2) post-glacial fluvial undercutting at the base of steep slopes.

Throughout the Pleistocene large masses of glacial ice have repeatedly filled and retreated from mountain valleys of the Nooksack River basin. During periods of glaciation valley-filling glaciers abut and physically support adjacent hillslopes, potentially preventing the failure of an otherwise unstable slope (Ballantyne, 2002). Simultaneously, the glaciers act to scour the hillslopes and deepen the valleys, generating relief and over-steepened valley walls in the process (e.g., Anderson et al., 2006). As the glacier eventually melts and recedes, the removal of the ice support may result in slope failures (McColl, 2012). Landslides associated with such glacial debuttressing are most likely to occur shortly following deglaciation (~15 ka for the Puget Lobe of the Cordilleran ice sheet; Porter and Swanson, 1998; Booth et al., 2003; Clark and Clague, 2021). For example, in the Upper Durance catchment of southeastern France a high concentration of rock slope failures occur in areas where glacial loading stresses and therefore the subsequent stress release was particularly high (Cossart et al., 2008). It is worth noting, however, that this area was affected dominantly by deep valley glaciers that loaded only the lower valleys between unglaciated ridgelines; the Nooksack basin was completely overridden by a continental ice sheet during the late Pleistocene, so that differential stresses between valley bottoms, valley walls, and ridgelines would have been smaller than in the Alpine setting of Cossart et al. (2008).

Unlike glacial debuttressing that affects an entire slope, fluvial debuttressing concentrates erosion and slope steepening at the base of a valley wall as lateral channel migration intersects and undercuts the slope. Such slope-steepening locally increases the shear stress, increasing the potential for failure to occur. In addition, such fluvial undercutting can expose or “daylight” failure planes, further increasing the risk of slope failure (Leith et al., 2013).

2.4.4 Volcanic Eruptions

Volcanic eruptions may also trigger landslides (e.g., Mount St. Helens; Voight et al., 1983), even on slopes that are not directly located on the volcanic edifice (e.g., Waythomas, 2013). For example, sustained seismicity (McNutt and Roman, 2015) associated with the movement of magma towards the surface may generate enough ground accelerations to trigger slope failure. Additionally, changes in slope stability caused by the deposition of tephra can trigger landslides even years after an eruption (e.g., forest mortality, soil permeability; Korup et al., 2019). All five of the rock avalanche deposits in this study are within ~25 km of an active stratovolcano, Mount Baker. Periodic eruptions since deglaciation likely generated significant seismic tremors, ejected tephra, and produced multiple pyroclastic, debris, and lava flows (Hyde and Crandell, 1979; Scott et al., 2020). Mount Baker's most recent magmatic eruption (~6.7 cal. ka B.P.; Scott et al., 2020) may have generated enough seismicity to trigger nearby rock slope failure.

2.5 Local and Regional Tectonics

For the Nooksack River basin there are two primary tectonic sources capable of generating enough seismicity to prompt failures: (1) The CSZ and (2) nearby shallow crustal faults, especially the Boulder Creek Fault (Sherrod et al., 2013; Fig. 1). The CSZ is the east-dipping interface between the subducting Juan de Fuca plate and the overlying North American plate. Its surficial trace is located ~120 km off the west coast of North America and stretches north to south ~1000 km from Vancouver Island, B.C. to Mendocino, CA (Goldfinger et al., 2012). Periodic (300 to 500-year recurrence) slip along the plate boundary can result in the generation of large ($M_w \geq 9.0$) megathrust earthquakes (Goldfinger et al., 2012). Seismic modeling by the USGS (ShakeMap 4.0; Worden et al., 2020) indicates that ground accelerations from these earthquakes could be significant throughout the region up to ~300 km away. Peak ground accelerations in the Nooksack basin during a M_w 9.3 CSZ earthquake event are estimated at ~0.1-0.2 g (Worden et al., 2020).

Although the most recent CSZ earthquakes are documented in various terrestrial and coastal records (e.g., Atwater and Hemphill-Haley, 1997; Atwater et al., 2004), longer term records that span the Holocene rely primarily on turbidite records from marine sediment cores collected from the abyssal plain west of the subduction zone (Goldfinger et al., 2012). Turbidites are submarine sediment gravity flows, essentially underwater landslides. Although turbidites can be triggered by other mechanisms, a common cause near subduction zones are large magnitude earthquakes. By establishing the sequence and timing of turbidites in the region, a paleoseismic record for the subduction zone can be established (e.g., Adams, 1990; Nelson, C.H. et al., 1996; Nelson, C.H., and Goldfinger, 1999; Blais-Stevens and Clague, 2001; Goldfinger et al., 2003a, 2003b; and Goldfinger et al., 2008). Goldfinger et al. (2012) tested this relationship for the CSZ by collecting sediment cores of turbidites in submarine channels off the coasts of Washington, Oregon, and Northern California. By correlating the ages of planktonic foraminifera sampled within each turbidite core, they were able to establish a paleoseismic record for the CSZ that spans the Holocene. Although some question the veracity of this record (e.g., Atwater et al., 2014), it remains the most robust continuous, long-term record of earthquakes along the CSZ.

In addition to seismicity related to the CSZ, the other most likely source for high acceleration seismic waves is from Holocene earthquakes along local crustal faults, many of which were recently identified with the introduction of high-resolution lidar data in northwestern Washington (e.g., Kelsey et al., 2012; Sherrod et al., 2013).

Of all the crustal faults in the vicinity of the study area, the Boulder Creek Fault (Fig. 1) is the most likely to have triggered one or more of these landslides. The Boulder Creek Fault, formed in the early- to mid-Tertiary as a south-dipping normal fault, has since reactivated as a reverse fault in response to north-south shortening of the North American Plate in western

Washington (Sherrod et al., 2013). Trenching and dating by Sherrod et al. (2013) indicates that there have been at least three Holocene ruptures (all $M_w > 6.3$) along the Boulder Creek Fault (Fig. 1): 8050-7250 cal. yr B.P., 3190-2980 cal. yr B.P., and 910-740 cal. yr B.P. The immediate proximity of this fault to the rock avalanche deposits in this study, particularly the Maple Falls landslide (which crosses the projection of the fault scarp; Fig. 4), makes it a particularly viable candidate for triggering one or more of the Nooksack basin landslides. Peak ground accelerations due to a M_w 6.8 rupture along the Boulder Creek fault are expected to range from 0.34-0.65 g (Seismic Scenario Catalog; WGS, 2017).

Two other shallow crustal faults in the vicinity of the study area, the Birch Bay Fault and the Darrington-Devils Mountain Fault (DDMF). While the timing of their most recent ruptures are poorly constrained, both have the potential to generate strong seismic ground shaking in the region. The Birch Bay Fault is located ~40 km west of the study area. Kelsey et al. (2012) estimated the most recent rupture date to 1280-1070 cal. yr B.P. with an estimated M_w of ~6.0-6.5. The DDMF is located ~50 km south of the study area. Two previous ruptures were estimated to have occurred around ca. 8000 cal. yr B.P. and ca. 2000 cal. yr B.P. each with M_w values of ~6.7-7.0 (Personius et al., 2014). Seismic modeling of a M_w 7.1 earthquake initiated at the DDMF results only in moderate shaking (PGA = 0.04-0.1 g) at the study area (Seismic Scenario Catalogue; WGS, 2017), making the DDMF a less likely source to have initiated the collapse of these rock avalanches. The distance of both faults from the study area makes them unlikely candidates for triggering the collapse of the large rock avalanches deposits in the Nooksack River basin. Conversely, uncertainties in both the potential rupture lengths (and therefore magnitudes) and in the timing of past events do not allow earthquakes from these faults to necessarily be ruled out.

3.0 METHODOLOGY

This project combines detailed lidar- and field-based geomorphic mapping with targeted bog sediment coring and boulder sampling to establish both the geomorphic characteristics and the collapse ages of three large rock avalanche deposits in the Nooksack River basin (Fig. 1). I used two independent dating methods to determine landslide collapse ages: radiocarbon dating (^{14}C) and beryllium-10 cosmogenic radionuclide exposure dating (^{10}Be-CRN).

3.1 Landslide Mapping

Lidar (light detection and ranging) provides a crucial source of data for this project. The most recent lidar-based Digital Elevation Model (DEM) that includes the study area (2017 North Puget Sound; https://lidarportal.dnr.wa.gov/) has a resolution of 0.9 m captured at 12.3 pulses/m^2. The resolution of this dataset enables detailed and precise geomorphic mapping of landslide deposits even in densely vegetated forest cover that would otherwise be impossible with traditional mapping techniques.

For this study, I combined field observations with lidar data to map and characterize each of the three landslide deposits in detail (Racehorse Creek, Middle Fork, and Maple Falls; Figs. 1, 2, 3, and 4, respectively). This mapping allows for qualitative descriptions of debris field morphologies, estimates of debris field volumes, and provides context critical to sampling for both ^{14}C and ^{10}Be-CRN dating methods. I followed landslide mapping protocols (e.g., Burns and Madin, 2008; Burns and Mickleson, 2016; Slaughter et al., 2017) established by the Washington Geological Survey (WGS) to ensure that my mapping is compatible with the recently published landslide inventory mapping in Whatcom County (Mickelson et al., 2020). To further supplement lidar-based mapping, I conducted targeted field mapping to confirm the outer extents and geomorphic characteristics of each of the three landslides investigated in this study. I used a hand-held GPS system (mapping-grade Trimble GeoXH 6000 GNSS) with sub-meter accuracy for navigation and accurate data collection in dense second- and third-growth forests.

3.2 Volume Calculations

To estimate the volumes of each landslide deposit I used the ArcMap tool *Cut-Fill* to calculate the volumetric difference between two DEMs, one representing the hillslope prior to failure and a second representing hillslope topography after collapse. I created a custom DEM for the pre-landslide topography by projecting surfaces from surrounding morphology (e.g., terraces, slopes). For the post-failure topography, I used the most recent lidar-based DEM provided by the WGS (2017 North Puget Sound). To validate the estimations, I also calculated the volume of void space left by the evacuation zones. In each case, both had similar volumes, however, because river erosion has removed an unknown volume of landslide debris, the volumes for the source hollows were slightly larger than that of the debris fields. All debris field volume calculations should be considered minimum estimates.

3.3 Geochronology – Radiocarbon Dating

Radiocarbon (^{14}C) dating remains the most reliable and best understood means of dating relatively young (< 40 ka) geologic deposits that incorporate organic material (Balco, 2011). The rock avalanche deposits in the Nooksack River basin offer excellent potential for ^{14}C dating because in each case landslide debris likely overran extensive forests with abundant vegetation, incorporating trees, branches, and other organic material. Malick (2018) confirmed the viability of such ^{14}C dating of Nooksack rock avalanche deposits by successfully constraining the timing (within analytic uncertainties) of the two youngest lobes of the nearby VZLC (Fig. 5).

Furthermore, all deposits are post-glacial in age, well within the datable time range for ^{14}C. Cross-cutting relationships clearly indicates that each deposit post-dates the retreat of the Cordilleran ice sheet in the area (~15 ka; Porter and Swanson, 1998; Clark and Clague, 2021).

There are two primary sources for obtaining suitable organic macrofossils (e.g., twigs, branches, logs, etc.) from landslide deposits: (1) exposures in landslide debris caused by river incision or human excavations and (2) basal sediments of bogs formed on top of landslide debris fields (Malick, 2018).

All three landslides in this study have debris fields that extend across the main river valleys and in each case may have temporarily dammed that portion of the Nooksack River. The river has subsequently incised each of the three debris fields and seasonal flooding occasionally creates fresh exposures (e.g., SI. 1), potentially exposing organic macrofossils buried and preserved in slide debris. Dating these materials can provide close proxies for the landslide collapse age by revealing the kill dates of the trees or other organic material entrained in the debris (Malick, 2018). For each deposit I identified potential debris exposures using lidar imagery and further investigated each in the field to recover suitable organic material. Although river incisions of slide debris have provided valuable ^{14}C age constraints in other situations (e.g., Pringle et al., 1998; Malick, 2018), limited exposures and lack of entrained organics associated with the failures precluded obtaining any dates for the landslide events.

Organic material preserved in the basal sediments of lakes and bogs formed on the surface of landslide debris fields can also provide age control for the timing of landslide collapses. Bogs are useful in this regard because they typically form shortly after landslide emplacement and commonly develop low-oxicity environments that inhibit deterioration of organic material contained within them. Collecting and dating organic material contained within the oldest and most basal bog sediments should provide close minimum limiting ages for the collapse of the landslide. Furthermore, organic material entrained by the landslide may be recovered from the slide debris located directly beneath the bog deposit. Malick (2018) demonstrated this by coring through bog sediments into the underlying slide diamicton, and recovered several datable organic macrofossils contained within it. Radiocarbon dates from these samples closely matched those from logs exposed in the landslide debris elsewhere. Dating such materials should provide direct ages of the landslide event rather than just minimum limiting ages.

Two of the three landslide deposits (Middle Fork and Racehorse Creek) possess bogs suitable for sediment coring. I collected a total of five cores (RHCLS-01, -02, -03, -04, -05) from two bogs on the Racehorse Creek debris field (Fig. 2) and a single 6-meter-long core (MFNLS-01) from a large bog on the Middle Fork deposit (Fig. 3). The absence of any natural bog or lake deposits on the debris field of the Maple Falls landslide (Fig. 4) precluded collecting any sediment cores from it.

I collected each sediment core using a hand-operated Livingston piston corer (Wright, 1967) and pushed to refusal in the approximate center of each bog. Refusal in nearly all cases was in coarse sediment (cobble or gravel). Unlike Malick's (2018) cores, this coarse basal debris was not definitively landslide diamicton (e.g., larger angular cobbles) and therefore ^{14}C dates from my sediment cores should be considered minimum limiting ages, not direct.

After transport back to the lab, I extruded the cores, analyzed each for magnetic susceptibility then split, photographed, logged visual stratigraphy, and sampled suitable organic macrofossils for ^{14}C dating. All ^{14}C samples were analyzed at DirectAMS in Bothell, WA following standard ^{14}C treatment protocols (e.g., Brock et al., 2010). I calibrated all ages with the CALIB v.8.2 online calibration calculator (Stuiver et al., 2020) and report all ages to 2-σ analytic uncertainties (Table 1).

3.3 Geochronology – Cosmogenic Exposure Dating

Cosmogenic radionuclide exposure dating (CRN) provides an independent, and relatively novel means of dating the collapse ages of rock avalanche deposits. In combination with ^{14}C dating, this method presents an excellent opportunity to test its viability in determining the collapse ages of bedrock landslides.

CRN dating relies on the steady buildup of beryllium-10 (^{10}Be) isotopes in the crystal structure of quartz as a result of near-constant bombardment of Earth's surface by high-energy cosmic rays from outer space (Balco, 2011). Because these rays only penetrate the uppermost 1-2 meters of rock (Balco, 2011), ^{10}Be isotopes only begin to accumulate once a rock is at or very near the surface. If a rock at depth is suddenly exposed at the surface (e.g., by a landslide) the net accumulation of ^{10}Be in the rock will directly relate to the timing of that event. Because the rates of ^{10}Be production (and loss due to radioactive decay) are known (Marrero et al., 2016), measurements of the abundance of in-situ ^{10}Be in a sample provides a means to calculate the length of time since the rock was first exposed at the surface by the landslide.

The Nooksack basin rock avalanche deposits are excellent candidates for dating via CRN for the following reasons: (1) each debris field contains multiple open-network boulder fields; (2) most boulders are very large (>2 m diameter) and in stable positions; (3) boulders are all sandstone originating from the Chuckanut Formation and generally contain a high quartz content

(>20%); (4) debris fields and boulders do not show evidence of significant post-emplacement weathering or erosion, or having been covered by soil since initial landslide emplacement; (5) the Chuckanut Formation is old enough (~45-55 Ma; Mustoe et al., 2007) and the half-life of ^{10}Be is short enough (1.39 x 10^6 yrs; Chmeleff et al., 2010) that any ^{10}Be generated during the initial erosion, transport, and deposition of sand grains that comprise the Chuckanut Formation should have decayed to insignificant values by the post-glacial age of the landslides; and (6) the chaotic nature of rock avalanche runout and the large volumes of each deposit makes it extremely unlikely (<5%) that any rock now exposed at the surface was also exposed at the surface prior to slope failure.

Despite these advantageous conditions, careful sample selection remains crucial to ensure the most accurate dates possible. I assessed each prospective boulder to ensure it met the following criteria:

(1) A high quartz content (>20%). This is necessary to reduce potential error associated with laboratory procedures (i.e., quartz purification and ^{10}Be isolation) and to reduce the size (and thickness) of sample required. I estimated quartz percentages both in the field with a hand lens and in the lab with thin section microscopy. All analyzed samples had 30% or greater quartz grains.

(2) Minimal post-emplacement weathering. Sampling an unweathered surface reduces the potential for dating error associated with the exponential reduction of cosmic ray flux as the rays penetrate into a rock (Balco, 2011). Any significant post-emplacement weathering of landslide boulders could result in CRN ages younger than the actual date of collapse. The boulders I sampled on each of the Nooksack basin deposits all

displayed a relatively unweathered appearance with only minor amounts (<1 mm) of grus accumulation in small hollows on boulder surfaces.

(3) Large and stable on low-gradient slopes. Because cosmic rays only penetrate the uppermost ~1-2 meters of a rock (Balco, 2011), any post-emplacement rotation or toppling of boulders could result in a model age younger than the actual collapse event. To avoid this issue, I sampled only from the tops of very large (>3 m diameter) boulders in stable positions. I also used a lidar-based slopeshade map (e.g., Slaughter et al., 2017) to target boulders resting on low-gradient slopes of 20° or less.

(4) Lacking evidence of significant tree growth. The Nooksack basin rock avalanche deposits are located in a region characterized by dense forest cover. Though most vegetation growth is considered negligible in terms of blocking or absorbing cosmic rays (due to an insignificant mass), larger trees (e.g., Douglas Firs) can grow to substantial widths and heights and possess a mass large enough to absorb a considerable portion of cosmic rays that would otherwise be absorbed by the boulder. To avoid this issue, I only sampled boulders that lacked evidence of past coverage by large trees (e.g., stumps, large roots, root-spalled slabs, etc.).

(5) Distal from areas of potential rockfall. To avoid the possibility of collecting samples unrelated to initial landslide emplacement, I only sampled from boulders that were far from potential sources of post-emplacement rockfall. Any such samples would result in ages younger than the primary collapse age of interest.

I collected and analyzed a total of 16 samples (each >1 kg) from prominent boulders following established protocols (Ivy-Ochs et al., 2009; Balco, 2011). For each sample, I recorded geographic coordinates, elevation, sample thickness, the orientation and dip angle of the sampled surface, and the position of the horizon relative to the sample (Appendix A). I crushed and sieved all rock samples at WWU's Geology Department rock lab and sent the 250-850 μm fraction to the University of Vermont – Community Cosmogenic Facility (UVM-CCF) for magnetic separation, quartz purification, and ^{10}Be isolation. Final analyses were performed at Purdue University's AMS facility, PRIME (Purdue Rare Isotope Measurement Laboratory). I calibrated all ages to calendar years with 2-σ uncertainties (CRONUScalc; Marrero et al., 2016) and compared them to the age constraints of known paleoseismic events (e.g., Goldfinger et al., 2012; Kelsey et al., 2012; Sherrod et al., 2013) significant volcanic events at Mount Baker (Scott et al., 2020) and age constraints of deglaciation of the region (Porter and Swanson, 1998; Clark and Clague, 2021).

To compare the timings from both ^{14}C and CRN dating methods, I convert all CRN-derived dates from "years before 2021" to "years before 1950" to better align with standard ^{14}C dating convention of "yr B.P." Dates that were established with ^{14}C dating are listed as "cal. yr B.P." and ages derived from CRN dating are denoted as "yr B.P.", or "years before 1950". All ages are rounded to the nearest decade and reported to 2-σ calibrated uncertainties. Both original "years before 2021" and adjusted "yr B.P." CRN dates are provided in Table 2. I also provide all data used (AMS spectrometry results, topographic shielding inputs, corrected and uncorrected ^{10}Be concentrations, and production rate calibration input) to calculate CRN ages in Appendix A.

4.0 RESULTS

Although the landslides investigated in this study have similar morphologies, ^{14}C and CRN dating techniques yielded a range of possible ages that span the post-glacial period. Most slides also appear to have experienced multiple recurring or overlapping failures, adding to the complexity of these results. Below I describe landslide morphologies, sampling locations, and dating results for each of the rock avalanches investigated in this study (Racehorse Creek, Middle Fork, and Maple Falls; Figs. 1, 2, 3, and 4, respectively). The VZLC and the CMS deposits have been fully characterized in previous studies (i.e., Malick, 2018 and Carpenter, 1993, respectively) and are both excluded from my morphologic descriptions. Additionally, dating results discussed in this section are limited to those collected for this study.

4.1 Landslide Morphologies

The Nooksack basin rock avalanche deposits possess many notable similarities. They are all relatively young (post-deglaciation, ~15 ka), derived from the same bedrock formation, and have similar geometries (area, volume, thickness, and runout distance). Below I describe the debris field and source zone morphologies, as well as ^{14}C and CRN sampling locations, for three of the Nooksack basin rock avalanche deposits (Racehorse Creek, Middle Fork, and Maple Falls). A summary of the various landslide statistics (i.e., volume, runout distance, etc.) is provided as Table 3.

4.1.1 The Racehorse Creek Landslide Morphology

The Racehorse Creek landslide is located ~5 km north of the confluence between the Middle and North forks of the Nooksack River (Figs. 1 & 2). The source zone for the deposit is a broad hollow in a northwest facing hillslope in the Chuckanut Formation (Fig. 2). It has total surface area of 0.73 km^2, a maximum estimated depth of ~60 m, an approximate bedrock orientation of 230°/28°, and an approximate void volume of 20.3 x 10^6 m^3.

The Racehorse Creek debris field comprises 19.5 x10^6 m^3 of landslide debris covering over 2.7 km^2. It also has a Height-to-Length runout ratio (H/L) of 0.17, a maximum runout distance of 3.3 km, and a maximum apparent thickness of ~30 m. The debris field consists of a single lobe of debris overlying both Holocene river alluvium and Pleistocene glacial outwash (Lapen, 2000). The hummocky northeastern margin of the lobe is partially buried by younger fluvial deposits emanating from Racehorse Creek (a Nooksack River tributary for which the landslide is named). The largest debris exposure along the Nooksack River (Site X; Fig. 2; SI. 2) reveals ~3 m of landslide diamicton overlying ~9 m of older floodplain deposits separated by an undulating oxidized contact. The landslide debris is poorly sorted with angular sandstone clasts embedded in a matrix of coarse to medium sand. The underlying floodplain deposit consists of weakly bedded silt with fine to medium sand that extends below the modern riverbed.

I subdivide the debris lobe into two sections (a primary debris mass and a smaller lateral debris mass) based on their distinct morphologies; however, the lack of any cross-cutting relationships suggests both sections formed during a single event. The primary debris mass forms a large tongue-shaped mass totaling an estimated 9.9 x 10^6 m^3 of rock and debris stretching over ~1 km^2. This lobe is unusual because of its sharply defined mounds, extensive open-network boulder fields, and notable symmetry of radiating hummocks (Fig. 2). The center of this mass is dominated by two large mounds (or hillocks) each rising more than 25 m above the surrounding topography. Longitudinal hummocks radiate outwards from the two central mounds with relief diminishing from the center of the mass towards the debris field margins. This section also contains many boulders (some >8 m in diameter; e.g., SI. 3) scattered throughout the debris field and in several locations, boulders are grouped into closely packed, open-network boulder fields. The most extensive of these boulder fields is located ~200 m north-northwest of the northern-most central hillock (Fig. 2). Boulders here are all poorly bedded to massive Chuckanut Formation sandstone and range in size from ~0.5 m to >8 m (avg. ~1-3 m) in diameter. Samples collected from this section include four CRN boulder samples (RHC-01, -02, -03, and -06) and two sediment cores from RHC Large Bog (RHCLS-04 and -05).

The smaller lateral mass consists of a lower, apparently thinner layer of debris that extends to the southwest and crosses the valley floor where it is incised by the North Fork Nooksack River (Fig. 2). This mass likely created (at least briefly) a landslide debris dam that may have resulted in the formation of a short-lived lake immediately upstream of the blockage. No direct evidence for this interpretation was recovered (e.g., drowned trees or lake sediments), although progressively incised fan deposits immediately downstream (south) of the debris crossing (Fig. 2) may be the result of breakout flooding associated with the overtopping and rapid erosion of the landslide debris dam. The lateral mass also contains a prominent ~1.7 x 10^6 m^3 mound of debris near its eastern edge (dashed line; Fig. 2). The WGS landslide inventory program (Mickelson et al., 2020) delineates this mound as a separate deposit with a separate headwall (implying a separate collapse event) from the main Racehorse Creek deposit; the reasoning for making this a distinct deposit, however, is unclear. Samples collected from the lateral debris mass include sediment core RHCLS-03, along with two others, RHCLS-01 and RHCLS-02. Because RHCSL-03 penetrated the deepest into the bog sediments, it was selected for ^{14}C sampling and dating.

4.1.2 The Middle Fork Nooksack Landslide Morphology

The Middle Fork landslide is located ~1 km east of the confluence of the North and Middle forks of the Nooksack River (MFN; Figs. 1 & 3). The landslide extends over 4 km from the top of the headscarp at an elevation of ~1200 m to below modern river level (at ~100 m elevation). The source zone is located on the west facing slope extending ~0.8 km downslope of the prominent dipslope failure plane exposed just beneath the modern ridgeline at an elevation of ~1200 m and down to a minimum elevation of ~700 m where the source zone meets the debris field (Fig. 3). The source zone has a total surface area of 0.75 km^2, a maximum estimated depth of ~100 m, an approximate bedrock orientation of 135°/51°, and an estimated void volume of 32 x 10^6 m^3. Additionally, the source hollow contains the only notable boulder field in the entire deposit where samples MFN-02 and MFN-03 were collected (Fig. 3).

Debris associated with the Middle Fork landslide occupies the area from the base of the source zone to ~3 km west where it extends across the river and abuts directly against Chuckanut Formation bedrock of the valley wall west of the river (Fig. 3). The debris field has an estimated volume of 34 x 10^6 m^3, a total surface area of 4.0 km^2, a H/L ratio of 0.25, a maximum runout distance of 4.4 km, and a maximum apparent thickness of ~80 m.

The upper third of the debris field begins at the base of the source zone and continues downslope for ~1.75 km until meeting a roughly 20 m rise in the debris that appears to extend across the entire north-south length of the debris field. In places along this boundary, debris from the upper third appears to overlap debris in the middle third of the debris field. It is unclear whether this is a localized internal failure or indicative of separate overlapping debris lobes that could represent multiple failure events. There are differences in surface expression east and west of this boundary. Debris to the east appears much more muted when compared to the hummocky debris to the west (Fig. 3). Further, the upper third lacks any clearly defined or notable hummocks, but instead is generally characterized by smoother morphologies with a single large mound in its approximate center. This mound comprises the majority of debris volume for the upper third of the debris field, rising ~30-40 m above the surrounding topography. In addition, this section has a noticeable absence of any large boulders such as those found in places across the middle third of the debris field and the source hollow. No suitable ^{14}C or CRN samples were located in this section.

The middle third extends ~0.8 km west from the north-south rise and ends along several prominent hills of Chuckanut Formation bedrock (Fig. 3). Although not obvious in lidar imagery, field investigations and published geologic maps (Dragovich et al., 1997; Lapen, 2000) reveal that most of these hills are outcrops of Chuckanut Formation protruding through landslide debris. Similarly, the prominent N-S escarpment immediately east of Mosquito Lake Rd. appears to be only shallowly covered by landslide debris in some localities and is largely void of debris along the western facing slope. This portion of the debris field displays considerably more variation in topography with numerous hummocks and large (~4-8 m) boulders scattered throughout. Boulders here are widely spaced, separated by tens or hundreds of meters. Samples collected from this area include two CRN boulder samples, MFN-04 and MFN-05, both collected from the tops of large (3-4 m) boulders resting on top of individual hummocks.

Also located within the middle third of the deposit, a sizable (4.3×10^4 m^2) bog deposit (here named the Middle Fork bog; Fig. 3) represents a critical sampling source for ^{14}C dating. A 6.15 m-long sediment core collected from the center of the bog (MFNLS-01; SI. 4a-4c), reveals 2.4 m of organic muds overlying 0.65 m of a white carbonaceous sediment with disarticulated shell fragments and 3.10 m of laminated silts and clays. At a core depth of 1.40 m the sediment is interrupted by a 4 cm thick pale-orange layer of ash (SI. 5) determined to be Mazama ash (7780-7590 cal. yr B.P.; Zdanowicz et al., 1999) by SEM-EDX major oxide analysis (SI. 6). Near the base of the core, two small twigs (samples M and P8-71A) were collected for ^{14}C dating analyses (Table 1).

The lower third of the debris field comprises debris to the west of the prominent bedrock hills, including debris occupying both west and east banks of the river within and adjacent to the modern floodplain (Fig. 3). This section displays a more muted topography than do the middle or upper thirds, but also has sizable mounds of landslide debris along the southern margins of the deposit near the river. At Site X (Fig. 3), on the east bank of the river, a large mound of incised landslide debris reveals a ~5 m section of landslide diamicton with angular boulders of Chuckanut Formation sandstone (~0.5 m diam.) that extends downward to the modern riverbed (SI. 7). Similarly, on the west bank of the river (Site Y; Fig. 3), river incisions reveal ~2-3 m of landslide debris that extends to the riverbed. The presence of large blocks of Chuckanut sandstone on the west side of the river, impounded against intact bedrock on the valley wall, clearly indicates that the landslide spanned the entire valley, and likely dammed the river for some length of time. No suitable samples from this portion of the debris field were located.

The riverbank immediately south of the landslide margin (Site Y; Fig. 3) also exposes the Middle Fork Lahar (Hyde and Crandell, 1978; Scott et al., 2020), the largest (240 x 10^6 m^3) post-glacial lahar from Mount Baker; the lahar deposit overlies landslide debris in several exposures along the river (e.g., SI. 8). This lahar thus provides a minimum limiting age for the timing of the landslide at ~6.7 ka (6890-6530 cal. yr B.P.; Scott et al., 2020). More lahar exposures occur north and south of this debris mound, but do not directly overly it, suggesting that the lahar did not completely override and cover the preexisting landslide debris mound. Partial infilling of the landslide debris by the lahar may explain in part the more muted relief of the slide debris adjacent to the modern river channel.

In addition to the lahar deposit, another river exposure ~100 m south of Site X (Fig. 3) reveals a 2-3 cm thick whitish-orange ash layer that overlies landslide diamicton (SI. 9). Major oxide analysis using SEM-EDX indicates that this tephra is Mazama ash and further demonstrates consistent stratigraphy between this location along the river and that of the Middle Fork bog.

4.1.3 The Maple Falls Landslide Morphology

The Maple Falls landslide is located ~1 km east of the town of Maple Falls, WA (Fig. 4). The source zone for this deposit is the bedrock hollow on the north facing slope of Slide Mountain (Fig. 4). The headscarp is defined by a steep bedrock wall (~150 m tall) along the southern margin of the source zone reaching a maximum of ~1020 m in elevation. The source zone is bounded to the west by an intact Chuckanut Formation dip-slope plane oriented approximately 315°/38° and to the east by the eastern lateral margin of a detached bedrock slump block (adjacent slump block; Fig. 4). The source zone also contains two distinct sections of debris, the upper third of the main Maple Falls deposit, and a detached bedrock slump block mapped as distinct from the main slide to the east (Fig. 4; Mickelson et al., 2020). The source zone (excluding the adjacent slump block) has a total area of 0.38 km^2, an estimated maximum depth of ~50 m, and an estimated void volume of 11.4 x 10^6 m^3.

The debris field for the landslide spans from the base of the headscarp and down to and across the North Fork Nooksack River (Fig. 4). Altogether, the debris field has a total estimated volume of 15 x 10^6 m^3, a total surface area of ~1.8 km^2, a H/L ratio of 0.31, a maximum apparent thickness of ~50 m, and a maximum runout distance of 2.8 km.

Contained almost entirely within the source zone, the upper third of the debris field is located between the base of the headscarp and ~1 km further downslope. This section has two lobe-shaped debris mounds with well-defined toes clearly visible on lidar hillshade imagery (Fig. 4). Additionally, the most extensive boulder field of all the Nooksack basin deposits is located in the upper-most portion of this section (SI. 10). Boulders here vary in size from ~2 m up to >8 m in diameter and exhibit an open-network framework with no evidence of significant post-depositional erosion. About 100 m north of this boulder field, CRN sample MF-03 was collected from a ~5 m diameter boulder partially embedded in the slide debris that comprises the upper of the two lobes within this section.

The deep-seated slump block to the east of this section (adjacent slump block; Fig. 4) is mapped as separate from the main Maple Falls deposit by the WGS (Mickelson et al., 2020) and appears distinct from the main slide mass on lidar imagery (Fig. 4). Because this block does not appear to be directly related to the main long-runout slide mass, I did not include it in volume estimates or conduct any field mapping or sampling in this area. It is possible, however, that this slump failed simultaneously with the main slide event(s) but exhibited different runout dynamics.

The middle third of the debris field extends from the lower of the two lobe-shaped mounds within the upper section and ~1 km downslope to the left (south) bank of the river (Fig. 4). Debris here displays overall larger and somewhat smoother hummocks with many poorly developed and discontinuous cross-slide convex debris lobes. Several open-network boulder fields also occur in this section. I collected two CRN samples, MF-01 and MF-02, from two large boulders in this location (Fig. 4).

The lower third of the debris field encompasses an area north of the North Fork Nooksack River (Fig. 4). This section spans from the right (north) bank of the river to ~300-500 m north where it meets a ~15 m tall, incised terrace. The debris field north of the river comprises a distribution of 2-4 m tall hummocks and scattered boulders covering ~0.5 km^2. The hummocks are most pronounced towards the middle of this area, with more muted hummocks both to the northwest and the southeast. Many large (~5-6 m diameter) isolated boulders are scattered throughout this section, each separated by about 50-100 m. No open-network boulder fields occur north of the river. Samples collected from this section include CRN boulder samples MF-04 and MF-05 (Fig. 4).

4.2 Radiocarbon and Cosmogenic Radionuclide Exposure Ages

To test potential triggering mechanisms of the Nooksack basin deposits, each landslide must have well-constrained age control. I constrain the timings of the previously undated or poorly dated deposits using both ^{14}C dating and CRN exposure dating. Despite the potential of datable material exposed in exposures along the modern river channels (e.g., Malick, 2018), no viable samples were located during this study.

4.2.1 The Racehorse Creek Landslide Ages

Although Pringle et al. (1998) located and dated a log underlying slide debris related to the Racehorse Creek slide, I was unable to locate any further reliable organic samples from bank exposures along the Nooksack River. Instead, I was able to provide new age constraints on the slide from organic materials in sediment cores recovered from two bogs formed on the landslide debris field (e.g., Malick, 2018). I collected a total of five sediment cores on the Racehorse Creek debris field: three from a small bog on the lateral debris mass (RHC small bog; Fig 2) and two from a larger bog located at the base of the source hollow (RHC large bog; Fig. 2). The smaller bog is bounded by a steep slope to the east, a large block of landslide debris to the south, and irregular hummocky terrain to the west and north (Fig. 2). The larger bog is formed in a depression between the base of the source zone and the primary debris mass (Fig. 2). Many fallen trees and other recent woody debris litter the base of the bog below the water surface.

Of the three cores collected from the smaller bog (RHCLS-01, RHCLS-02, and RHCLS-03), only RHCLS-03 was analyzed because it reached the deepest stratigraphic level at ~1 m below the bog surface. The upper 0.75 m of sediment in RHCLS-03 comprises peat and organic-rich mud, with the most basal section consisting of 0.27 m of reduced greenish-gray clay. A ~2 mm twig embedded in the clay layer 0.85 m below the bog surface, Sample M, returned an age of 1390-1310 cal. yr B.P. (1480 ± 21 ^{14}C yr B.P.; Table 1). Because the core did not bottom in slide diamicton, this age represents a minimum limiting age for the landslide.

Both cores from the larger bog (RHCLS-04 and RHCLS-05) encountered buried logs, which prevented penetration to landslide diamicton. Core RHCLS-04 met refusal ~1 m below the bed of the bog and core RHCLS-05 penetrated a total of ~3 m into bog sediments before refusal. The entire ~2 m of recovered sediments in RHCLS-05 comprise organic matter, mud, and several sections of wood. A ~3 cm twig (Sample V) embedded in the mud at a depth of 2.87 m yielded an age of 3360-3190 cal. yr B.P. (3065 ± 26 ^{14}C yr B.P.; Table 1). Again, because we did not recover any material identifiable as landslide diamicton, the age for this sample represents a minimum limiting age for the emplacement of the landslide.

For CRN dating, I collected samples from four boulders in the Racehorse Creek deposit, all from within the primary debris mass. Two samples, RHC-01 (SI. 11) and RHC-02 (SI. 12), are from a pair of closely spaced (~10 m apart) boulders (~7 m and ~3 m diameters, respectively) located within the expansive open-network boulder field described in section 4.1.1. RHC-03 (SI. 13) was collected from a 5 m diameter boulder located ~100 m southeast of RHC-01 and RHC-02. RHC-06 (SI. 14) is a ~4 m diameter boulder located ~500 m south of the first three samples. Boulder RHC-01 returned an age of 8810 ± 1590 (10390-7220) yr B.P. and ~10 m to the east of the first boulder, RHC-02 yielded an age of 5080 ± 1130 (6210-3950) yr B.P. RHC-03 yielded an age of 4290 ± 1750 (6040-2540) yr B.P. RHC-06 returned an age of 3800 ± 900 (4700-2900) yr B.P. (Table 2).

4.2.2 The Middle Fork Nooksack Landslide Ages

For ^{14}C dating, two samples were collected near the base of sediment core MFNLS-71A701 (SI. 4c). Both samples (F and P8-71A; Table 1), were small twigs (~2-4 mm) embedded in the clay and silt layer at core depths of 6.13 m and 6.11 m, respectively. Sample F was dated to 10150-9690 cal. yr B.P. (8816 ± 41 ^{14}C yr B.P.) and sample P8-71A was dated to 10170-9760 cal. yr B.P. (8855 ± 39 ^{14}C yr B.P.; Table 1).

For CRN dating, I collected a total of four samples from two pairs of boulders on two morphologically distinct sections of the debris field. The upper pair, MFN-02 (SI. 15) and MFN-03 (SI. 16), are from two boulders separated by ~50 m in a boulder field on a gently sloping bench located near the base of the source zone and ~400 m below the main headscarp (Fig. 3). The lower pair, MFN-04 (SI. 17) and MFN-05 (SI. 18), were collected from two prominent and isolated boulders located within the hummocky section of the middle third of the debris field

(Fig. 3). Boulder samples MFN-02 and MFN-03 returned analytically identical ages of 3610 ± 900 (4510-2710) yr B.P., 3580 ± 880 (4460-2700) yr B.P., respectively. MFN-04 returned an age of 7640 ± 1300 (8940-6330) yr B.P. and MFN-05 returned an age of 9230 ± 1400 (10630-7830) yr B.P. (Table 2). Despite the age discrepancy between MFN-04 and MFN-05, both boulders (along with the Middle Fork bog) occupy the same geomorphic zone of hummocks and debris (see discussion).

4.2.3 The Maple Falls Landslide Ages

No viable bog deposits occur within the debris field of the Maple Falls landslide and although the North Fork Nooksack River exposes portions of the landslide along its banks, the exposures are all either covered with heavy vegetation, or armored with large slide boulders (SI. 19) or human-placed riprap, precluding collection of ^{14}C samples related to the emplacement of the landslide.

For CRN dating, I sampled a total of five boulders from the debris field of the Maple Falls landslide deposit. Samples MF-01 (SI. 20) and MF-02 (SI. 21) are from two closely spaced boulders (3 m and 6 m diameters, respectively) within a small boulder field in the approximate center of the debris field (Fig. 4). Sample MF-03 (SI. 22) is from a ~3 m diameter boulder embedded in a lobe-shaped mound of debris below the source zone about 500 m upvalley of MF-01 and MF-02 (Fig. 4). The lowest two samples, MF-04 (SI. 23) and MF-05 (SI. 24), were collected on two prominent boulders in the lowest third of the debris field, separated by ~120 m and located ~400 m north of the NF Nooksack River and ~2.5 km from the main landslide headscarp. Boulders MF-01 and MF-02 yielded analytically indistinguishable ages of 3370 ± 740 (4110-2630) yr B.P. and 3310 ± 710 (4010-2600) yr B.P., respectively. Boulder MF-03 returned an age of 630 ± 400 (1030-230) yr B.P., the youngest age in this study. Boulders MF-04 and MF-05 returned ages of 5330 ± 1140 (6470-4190) yr B.P. and 7130 ± 1190 (8310-5940) yr B.P., respectively (Table 2).

4.2.4 The Van Zandt Landslide Complex Ages

The emplacement timing of the VZLC is already established with reliable ^{14}C age control (Malick, 2018). Because the VZLC is similar to the landslides in my study in most ways (source rock type, location, long-runout, etc.), I collected three additional boulder samples from the VZLC debris field to provide a controlled test of the reliability of CRN dating for the Nooksack basin rock avalanche deposits. All three samples were collected from large, isolated boulders embedded in a large debris mound located immediately downslope of the source hollow and within Debris Lobe 2 of Malick (2018; Fig. 5). The first sample, VZLC-01 (SI. 25), was collected from a ~3 m boulder and yielded an age of 2110 ± 750 (2860-1350) yr B.P. Samples VZLC-02 (SI.26) and VZLC-03 (SI. 27) were collected from the tops of two exceptionally large (~8 m diameter) boulders, separated by ~130 m and yielded ages of 1580 ± 590 (2170-990) yr B.P. and 1550 ± 800 (2340-750), respectively. Although VZLC-01 is slightly older than the other two, all three dates overlap within analytic uncertainty of the independent ^{14}C control for the slide (1530-1260 cal. yr B.P.; Malick, 2018). Furthermore, the ages for VZLC-02 and VZLC-03 also overlap with Malick's (2018) most reliable ^{14}C sample that further constrains the timing for Debris Lobe 2 to 1330-1270 cal. yr B.P.

5.0 DISCUSSION

The five rock-avalanche deposits in the Nooksack River basin have similar volumes, runout distances, surface morphologies, and source lithologies (except CMS). The presence of five such remarkable deposits in a such a small geographic area make these landslides excellent candidates to test whether they also share a common triggering mechanism. The key to such tests is accurate and precise dating of the landslide events; below I assess the quality and uncertainties of my numerical dates (^{14}C and CRN) for the four landslides that involve Chuckanut Formation bedrock.

Radiocarbon results in this study provided valuable age constraints for several of the landslides, however, because none of the ^{14}C analyses were on organics preserved in the actual landslide debris (e.g., Malick, 2018), they provide only limiting ages for the various slides. In contrast, the CRN analyses, which theoretically should provide direct ages of each major slope failure, instead suggest a more complex picture of landslide behavior, including emplacement timing, post-slide weathering, and pre-slide exposure history; the lattermost aspect may potentially provide insight into emplacement dynamics of the slides. Although the timing constraints allow earthquakes as a possible trigger, the analytic and geologic uncertainties associated with both dating methods precludes linking the slides to specific earthquakes with any confidence.

Despite the variability and large uncertainties associated with my CRN model ages, they can be a viable method for dating rock avalanche deposits such as those in the Nooksack River basin. Although significant problems affect some of the samples (e.g., cosmogenic inheritance; see section 5.3), the fact that three closely located pairs of boulders on three of the four deposits have CRN ages that are essentially identical to each other (MF-01 and MF-02; MFN-02 and MFN-03; VZLC-02 and VLZC-03) indicates that they are likely to be accurate for the emplacement age of each, and by extension, that CRN dating can be used to estimate the collapse timings of such landslides. The CRN ages and surface morphologies for each landslide indicates that three of the deposits (MFN, MF, and VZLC) are composed of multiple overlapping debris lobes, demonstrating that these sites experienced recurring failures. Apparent cosmogenic inheritance in several CRN samples suggests that such rock avalanches may experience some degree of "block rafting" where large blocks of debris may be supported by more turbulent debris beneath. This, in theory, could result in less block rotation than would otherwise be expected. If this is true, then the chances of sampling a boulder with prior cosmic ray exposure (and inherited ^{10}Be) may be higher than would be predicted by debris deposited by highly turbulent flows. Each of these ideas are discussed in more detail below.

5.1 Debris Lobes and Emplacement Timings

5.1.1 The Racehorse Creek Landslide

The debris field of the Racehorse Creek landslide consists of a bifurcated lobe related to a single failure event. Although the WGS landslide group (Mickelson et al., 2020) mapped a secondary landslide deposit located within the lateral debris mass (dashed line; Fig. 2), there is no distinct source zone immediately upslope of this hummock and therefore I interpretate it as part of the main deposit.

A minimum age limit for the Racehorse Creek landslide is provided by a ^{14}C age on a small twig collected ~2 m below the bed of RHC large bog (Sample V; 3360-3190 cal. yr B.P.; Table 1). The maximum limit is from a ^{14}C age (4420-3990 cal. yr B.P.; Pringle et al., 1998) from a log embedded ~20 cm below the basal contact of the landslide that was exposed in a cutbank along the Nooksack River. Pringle et al. (1998) contend that the log was emplaced by the landslide and is therefore a direct age, not a minimum for the event. CRN ages from boulders RHC-02 (5080 ± 1130 [6210-3950] yr B.P.), RHC-03 (4290 ± 1750 [6040-2540] yr B.P.), and RHC-06 (3800 ± 900 [4700-2900] yr B.P.) all fall within the window (4420-3990 cal. yr B.P) established by Pringle et al. (1998). The relatively large uncertainties of the three CRN ages, however, do not provide improved constraints for the timing of this landslide. The age for boulder RHC-01 (8810 ± 1590 [10390-7220] yr B.P.) is significantly older than the minimum age established by Pringle et al. (1998) and most likely is indicative of cosmogenic inheritance. I therefore consider Pringle et al.'s (1998) ^{14}C age of 4420-3990 cal. yr B.P. (Table 1) the best available date for the timing of the Racehorse Creek landslide, particularly if their interpretation that the dated log was killed and entrained by the landslide.

5.1.2 The Middle Fork Nooksack Landslide

The Middle Fork Nooksack deposit appears to comprise at least two overlapping debris lobes that represent distinct collapse events (lower and middle thirds together as Event 1 and the upper third as Event 2; Fig. 3). My interpretation of two debris lobes (Event 1 and Event 2) is based primarily on the difference in dating results from boulders and sediment core MFNLS-01, and their locations in the deposit; complex hummocky terrain between the dated boulders do not indicate a clear morphologic boundary between the deposits. The older deposit (Event 1) occurred before 10170-9690 cal. yr B.P. This timing is based on ^{14}C dates from two twigs recovered near the base of sediment core MFNLS-01 (Samples F and P8-71A; Table 1). Because the samples were collected close to (< 4 cm) the base of the core, and core refusal was met on a solid surface (potentially coarse debris related to the landslide), I interpret this age as a close minimum limiting age for the collapse of the landslide. CRN boulder ages from the two samples collected north of the bog, MFN-04 (7640 ± 1300 [8940-6330] yr B.P.) and MFN-05 (9230 ± 1400 [10630-7830] yr B.P.), also appear to provide minimum ages for the slide (Table 2). The age for boulder MFN-04 is significantly younger than the basal ^{14}C ages from MFNLS-01 and may indicate post-depositional spalling or weathering of the sampled boulder. The age for MFN-05 is consistent with the ^{14}C age constraints and may support an early Holocene (or late Pleistocene) collapse age; the apparent weathering (and partial resetting) of MFN-04, however, suggests that MFN-05 may also have experienced some post-emplacement weathering so this age may also represent a minimum for the event. Ultimately, the timing for Event 1 is bounded between deglaciation (~15 ka; Clark and Clague, 2021) and the minimum timing from the base of sediment core MFNLS-01 (10170-9690 cal. yr B.P.) although I consider the minimum timing from MFNLS-01 to be closer to the actual timing of landslide emplacement.

The emplacement timing for Event 2 is based on CRN model ages from two adjacent boulders resting on the gently dipping bench within the source zone of Event 1 (MFN-02 and MFN-03; Fig. 3). The two boulders returned ages of 3610 ± 900 (4510-2710) yr B.P. and 3580 ± 890 (4460-2700) yr B.P., respectively (Table 2) and together provide evidence that they record a collapse event occurring at this time.

5.1.3 The Maple Falls Landslide

The Maple Falls deposit has at least two overlapping debris lobes that represent distinct collapse events. Debris in the lower and middle thirds (distal and medial zones, respectively; Fig. 4) geomorphically appear to represent a single emplacement event (Event 1), whereas two smaller lobes closer to the source headwall represent one or two younger events. The best age constraint for the oldest event is provided by CRN dating of a pair of boulders in the middle third (MF-01 and MF-02) with closely overlapping exposure ages of 3370 ± 740 (4110-2630) yr B.P. and 3310 ± 710 (4010-2600) yr B.P. (Table 2). Samples collected from two boulders in the lower third of this debris lobe north of the river, MF-04 and MF-05, returned much older, but disparate model ages of 5330 ± 1140 (6470-4190) yr B.P. and 7130 ± 1190 (8310-5940) yr B.P., respectively (Table 2). Because these ages disagree both with the younger overlapping ages from further upslope the debris field as well as with each other, and because there are no indications of geomorphic discontinuities between this portion of the lobe and the middle third of the debris field, I infer that these distal ages represent some form of inheritance from the pre-slide source zone. Furthermore, the possibility of the lower third being sourced from the north is precluded because of a difference in lithology but also because there is no reasonable source for the debris from that direction (Fig. 4). Finally, the relatively youthful morphology of this portion of the debris lobe is consistent with the younger CRN ages, and less so with the older ages.

The two younger debris lobes located in the upper third (proximal zone) near the source headwall are clearly defined by distinct landslide toes imaged on lidar hillshade imagery (Fig. 4). The only age control for this section is a single CRN boulder MF-03 (630 ± 400 [1030-230] yr B.P.) from the upper of the two lobes (Fig. 4). Although a single sample is not sufficient to confidently conclude a timing for this lobe, this boulder should represent the timing of this debris lobe because the boulder was embedded into the hillslope distal from the headwall (SI. 22), making it extremely unlikely that it was sourced from a secondary rockfall or was rotated in any way since its initial emplacement. The freshness of the boulder surface and lack of any apparent weathering of boulders in the area also suggests that post-depositional weathering has not significantly reset the exposure age.

5.1.4 The Van Zandt Landslide Complex

The Van Zandt deposit is composed of three lobes designated Debris Lobes 1, 2, and 3 (Fig. 5 Malick, 2018). The younger two lobes, Debris Lobes 2 and 3, are both well-dated by ^{14}C dating and although Debris Lobe 3 clearly overlaps (and thus postdates) Lobe 2, the ^{14}C ages are indistinguishable (Malick, 2018). Debris Lobe 2 is by far the largest of the three lobes and was therefore the focus of my study. CRN ages for two of the three boulders sampled from Debris Lobe 2 (VZLC-02 1580 ± 590 [2170-990] yr B.P., and VZLC-03 1550 ± 800 [2340-750] yr B.P.) fit within the age window (1330-1270 cal. yr B.P.) determined by Malick (2018) from ^{14}C dating of in-situ landslide debris preserved in sediment cores of bogs and from a gravel pit exposure (Table 1). Conversely, sample VZLC-01 (2110 ± 750 [2860-1350] yr B.P.) is slightly older than Malick's age constraints at both 1-σ and 2-σ (although only by ~100 yr at 2-σ). Despite this discrepancy, it is notable that this model age overlaps with the younger two CRN samples at 2-σ.

5.1.5 The Church Mountain Sturzstrom

The CMS deposit differs from the four other Nooksack basin deposits in a few crucial ways (e.g., different lithology and a much larger volume), but its proximity to the other landslides and its shared classification as a catastrophic long-runout rock avalanche suggests that it may have a similar trigger. Although large portions of the deposit have been removed by the North Fork Nooksack River, it appears to represent a single failure event. Several studies have provided ^{14}C dates for the event (Cary et al., 1992; Carpenter, 1993; Pringle et al., 1998), but I consider Pringle et al.'s (1998) age for the CMS deposit as the most reliable for the timing of the landslide emplacement (2700-2150 cal. yr B.P.; Table 1) because their analyses yielded identical results from two separate logs embedded in the slide debris and because of discrepancies in Carpenter's (1993) dating and results (see Pringle et al., 1998).

5.2 Potential Triggering Mechanisms

Determining the mechanism that causes a particular landslide to fail is difficult, especially for prehistoric landslides. Dating methods, such as ^{14}C, can constrain the timing of a particular event to within several decades in the best situations. The analytic and geologic uncertainties associated with CRN and ^{14}C dating, however, precludes definitively linking a particular landslide to a specific triggering event. Studies that do establish such a correlation generally rely on statistically robust data from large datasets with thousands of individual dated landslide deposits (e.g., LaHusen et al., 2020) or use precise dating methods, like dendrochronology with annual precision (e.g., Struble et al., 2020). Dendrochronology, however, is not applicable to the rock avalanche deposits in my study area because the deposits are all well-beyond the ages of any living trees. In addition, extensive historic logging has removed essentially all old-growth (>100-200 yr) trees near any of the slide deposits so there is no means to establish a master dendrochronologic chronology even if buried logs are found in a deposit. Nevertheless, the concentration of events and the best age control on the main collapses provide some insight into the concept that most if not all of these deposits may have been triggered by large seismic events.

5.2.1 Large Magnitude Earthquakes

Below, I compare the timings of seven collapse events with the timings of known paleoseismic events that affected the area. The collapse events I consider are: (1) Racehorse Creek, (2) Middle Fork – Event 1, (3) Middle Fork – Event 2, (4) Maple Falls – Event 1, (5) Maple Falls – Event 2, (6) Van Zandt – Debris Lobe 2, and (7) Church Mountain (Table 4).

The two most likely sources of large magnitude earthquakes with the potential to generate destabilizing ground accelerations in the study area are: (1) subduction zone earthquakes from the CSZ and (2) shallow crustal earthquakes from the Boulder Creek fault (ShakeMap 4.0; Worden et al., 2020). Here I compare the paleoseismic records for the CSZ from Goldfinger et al. (2012) and the Boulder Creek fault from Sherrod et al. (2013) to the timings of each of the seven dated collapse events in the Nooksack River basin. The timings for the seven landslide events and overlapping earthquakes are summarized in Table 4.

(1) For the Racehorse Creek deposit (4420-3990 cal. yr B.P.; Pringle et al., 1998), only CSZ event T9 (4280-3920 cal. yr B.P.; Goldfinger et al., 2012) overlaps with the timing of the landslide.
(2) Event 1 of the Middle Fork landslide (10170-9690 cal. yr B.P.; *this study*) overlaps with CSZ event T18 (9980-9560 cal. yr B.P.; Goldfinger et al., 2012).
(3) Event 2 of the Middle Fork landslide (4510-2700 yr B.P.; *this study*) overlaps with four distinct seismic events: CSZ event T9 (4280-3920 cal. yr B.P.; Goldfinger et al., 2012), CSZ event T8 (3600-3290 cal. yr B.P.; Goldfinger et al., 2012), CSZ event T7 (3160-2870 cal. yr B.P.; Goldfinger et al., 2012), and Boulder Creek Earthquake B (3190-2980 cal. yr B.P.; Sherrod et al., 2013).
(4) Event 1 of the Maple Falls landslide (4110-2600 yr B.P.; *this study*) overlaps with five earthquake events: CSZ event T9 (4280-3920 cal. yr B.P.; Goldfinger et al., 2012), CSZ event T8 (3600-3290 cal. yr B.P.; Goldfinger et al., 2012), CSZ event T7 (3160-2870 cal. yr B.P.; Goldfinger et al., 2012), CSZ event T6 (2670-2390 cal. yr B.P.), and Boulder Creek Earthquake B (3190-2980 cal. yr B.P.; Sherrod et al., 2013).

(5) Event 2 of the Maple Falls landslide (1030-230 yr B.P.; *this study*) overlaps with four earthquake events: CSZ event T3 (910-680 cal. yr B.P.; Goldfinger et al., 2012), CSZ event T2 (570-380 cal. yr B.P.; Goldfinger et al., 2012), CSZ event T1 (370-140 cal. yr B.P.), and Boulder Creek Earthquake C (910-740 cal. yr B.P.; Sherrod et al., 2013).

(6) Debris Lobe 2 of the VZLC (1330-1270 cal. yr B.P.; Malick, 2018) overlaps with CSZ event T4 (1350-1120 cal. yr B.P.; Goldfinger et al., 2012).

(7) The CMS (2700-2150 cal. yr B.P.; Pringle et al., 1998) overlaps with one earthquake event, CSZ event T6 (2670-2390 cal. yr B.P.; Goldfinger et al., 2012).

Although each dated landslide in this study overlaps with one or more seismic events, the uncertainties are too large to confidently conclude that seismicity is the most likely trigger for any of these landslides. Taken as a whole, however, the fact that all landslide events overlap with known paleoseismic events suggests that at least some may have been associated with seismicity. As many others have determined (e.g., Keefer, 1984; Zhang et al., 2011; Wartman et al., 2013; Coe et al., 2016; Zhang et al., 2016; Valagussa et al., 2018) large magnitude earthquakes are a well-known trigger for large rock avalanches. For the Nooksack deposits, the best available evidence in favor of a seismic trigger remains Debris Lobe 2 of the VZLC (Malick, 2018). This is due to a relatively narrow age range for both the timing of the landslide (1330-1270 cal. yr B.P.; Malick, 2018) and of the earthquake (CSZ event T4; 1350-1120 cal. yr B.P.; Goldfinger et al., 2012) and because Malick (2018) was able to recover and date organic material directly from the landslide diamicton.

5.2.2 Glacial Debuttressing

Because repeated glacial occupation and scour of the region is a primary cause for the steep slopes that are a primary pre-requirement for these landslides, debuttressing during deglaciation is a clear potential trigger for such failures. Most of the deposits are too young (late-Holocene) to fit easily with this concept, however, the deposit with the greatest potential to have been triggered by glacial debuttressing is Event 1 of the Middle Fork landslide, the oldest of the Nooksack rock avalanches, because it is the only landslide that occurred within a few thousand years of deglaciation (~15 ka; Clark and Clague, 2021). If the landslide event occurred shortly after glacial recession, then it is possible that the thick deposit of silts and clays at the base of bog core could have accumulated rapidly from the erosion of sediments on a freshly deglaciated, unvegetated surface, or alternatively from the landslide scar remaining relatively unvegetated during the early deglacial period.

5.2.3 Other Triggering Mechanisms

There are a variety of other mechanisms that have the potential to act as triggers for large landslides (Highland and Bobrowsky, 2008). The most common of these is intense or prolonged precipitation, especially in humid regions such as the Pacific Northwest (Mock, 1996). It is notable that a sizeable landslide adjacent to the Racehorse Creek landslide (SI. 28) was triggered by atmospheric river event in 2009 (Crider et al., 2009). Unfortunately, high-resolution records of prehistoric precipitation (e.g., tree-ring records, speleothems, etc.) do not exist for this locality, and in fact are rare in most settings. Furthermore, few records of prehistoric rainfall are of sufficient resolution to correlate a specific landslide event to a particular storm or even a particular wet season.

Due to the proximity of Mount Baker (~25 km east), volcanic activity must also be considered as a possible triggering mechanism. The two most recent eruptive periods of Mount Baker are the Schriebers Meadow eruptive period (9.8-9.1 ka) and the Mazama Park eruptive period (ca. 6.7 ka; Scott et al., 2020). Only the Schriebers Meadow period potentially overlaps with any of the landslides considered here, Event 1 of the Middle Fork landslide (>10,170-9,690 cal. yr B.P.). The distance between the landslides and Mount Baker, and the relatively low-magnitude shaking that occurs during eruptions, makes it unlikely that volcanic seismicity triggered any of the landslides considered in my study.

5.3 CRN Age Variability and Uncertainty

Results from CRN dating returned a relatively wide range of model ages and implications for the timings of the Nooksack basin deposits. Some boulders returned ages that aligned with independent ^{14}C dating and others were significantly different, both older and younger. For example, at the Maple Falls slide boulder pairs MF-01 and MF-02 agreed in their timings with means differing by only 30 years (Table 2). Conversely, boulder pair MF-04 and MF-05, collected from what appears to be a distal portion of the same geomorphic debris lobe (Fig. 4), differ from each other by close to 2000 years and differ from the mean of MF-01 and MF-02 by ~2000 and ~3800 years respectively (Table 2). Although the two pairs of boulders were collected just over 1 km from each other, there is no geomorphic indication that the debris north of the river represents a separate older mass wasting event (Fig. 4). The fact that the basal contact of the distal portion of the slide remains below the modern river level is also consistent with a relatively young age (late-Holocene) for the main slide (Maple Falls - Event 1). Furthermore, even if the distal deposits represent an older event, such a scenario does not explain the age difference between MF-04 and MF-05.

One reasonable explanation for the older model ages in the distal lobe is cosmogenic inheritance. During a catastrophic rock avalanche, a significant degree of turbulence and mixing of the debris would be expected (e.g., Guthrie et al., 2012). This turbulence would, in theory, result in a mass with a thoroughly mixed matrix of rock and debris. In this situation, cosmogenic inheritance in surficial boulders in the deposit should be minimal considering that any rock that was previously exposed within 1-2 m of the surface (the general penetration depth of cosmic rays) should be insignificant when compared with the volume of fresh, previously unexposed rock now at the surface. When comparing the surface volume of pre-exposed rock at or near the surface prior to failure to the total volume of rock debris after failure, my volumetric calculations based on the lidar data indicate that only ~5% of the overall rock mass would have any pre-exposure to cosmic radiation. Of the 16 samples collected in this study, four, or 25%, have ages that appear to be too old when compared to either agreeing CRN boulder pairs or independent ^{14}C ages. This effect could be explained by boulders "rafting" on top of debris during runout. Instead of a thoroughly mixed mass, such "rafting" may result in a debris mass with a greater proportion of rock that was at or near the surface prior to failure being exposed at the surface after failure. Although intriguing, more data would be needed to thoroughly test this concept. Another potential source of inheritance, caused by the much lower rate of muonogenic production of cosmogenic isotopes, may also be a factor in creating unusually old model CRN ages. This production pathway would only be important if repeated continental glaciation during the Pleistocene was substantially less effective at stripping bedrock than has largely been presumed in the region (e.g., Francis, 2019).

Another concern with the CRN dating results is that some boulders returned model exposure ages that are substantially younger than more reliable age control. This situation only occurs in the oldest deposit, the Event 1 of the Middle Fork landslide. Boulder MFN-04 has an age that is significant younger than the minimum established ages from ^{14}C dates at the base of sediment core MFNLS-01. Although care was taken during sampling to avoid any obviously eroded portions of any of the boulders and this sample was collected from the boulder's most prominent and least disturbed surface, the most plausible explanation for the young model age is post-depositional weathering and erosion of the sampled boulder. Because boulders in a rock-avalanche debris field have no definitive features that would indicate a lack of post-emplacement weathering (e.g., striae on glacial boulders), it is impossible to rule out this potential influence.

Despite the many uncertainties involved in this study, the age constraints on these large, long-runout landslides suggest that all could have been triggered by large seismic events. The age constraints on collapse ages for each landslide overlap with ages for known CSZ earthquakes or local Boulder Creek earthquakes, however, the uncertainties in the ages for both landslides and earthquakes, and the lack of good constraints on other possible triggers (especially heavy precipitation events) precludes ruling out other such events as triggers.

6.0 CONCLUSIONS

This study compares the morphology and timing of a suite of five prehistoric rock avalanche deposits in the middle reaches of the Nooksack River basin, northwest Washington State. The deposits have similar volumes (>10 x 10^6 m^3), long runouts that extend across the valley floors, and all but one involves highly deformed Eocene Chuckanut Formation bedrock. The goal of the study was to test if these common characteristics also reflect a common triggering mechanism.

The Middle Fork landslide appears to comprise two overlapping debris lobes (Event 1 and Event 2) that cover a combined 3.4 km^2 with an estimated volume of 34 x 10^6 m^3, a total relief of 1,120 m, and a H/L of 0.25. Two twigs collected from the base of a 6-meter-long sediment core (MFNLS-01) recovered from a large bog in the lower half of the debris field reveal a minimum limiting age of 10,170-9690 cal. yr B.P. for Middle Fork Event 1. CRN model ages from two boulders near the bog, MFN-04 and MFN-05 (7640 ± 1300 [8940-6330] yr B.P. and 9230 ± 1400 [10630-7830] yr B.P., respectively), broadly support this age constraint, although the younger date suggests that CRN ages for it (and possibly both boulders) have been partially reset by post-emplacement weathering. CRN ages for a pair of adjacent large boulders in the upper third of the deposit have statistically indistinguishable CRN model ages at 3610 ± 900 and 3580 ± 880 (combined 4510-2700) yr B.P. The lack of apparent weathering and the similarity of these two ages indicates that they are not a result of weathering and instead record a second, smaller landslide, Middle Fork Event 2. I note, however that there is not a clear morphologic boundary between the upper and lower deposits.

The Racehorse Creek Landslide is composed of a single debris lobe that covers approximately 2.7 km^2 and has an estimated volume of 19.5 x 10^6 m^3, a total relief of 580 m, and a H/L of 0.17. Three of four CRN-dated boulders in the debris field yielded ages (5080 ± 1130 [6210-3950] yr B.P., 4290 ± 1750 [6040-2540] yr B.P., and 3800 ± 900 [4700-2900] yr B.P.) that lie within uncertainties of the emplacement timing reported by Pringle et al. (1998; 4420-3990 cal. yr B.P.) and are also consistent with minimum limiting ^{14}C dating of bog sediment cores from my study (3360-3190 cal. yr B.P.).

The Maple Falls landslide is composed of at least two overlapping debris lobes that may represent distinct failure events and cover a combined 1.8 km^2 of area with an estimated volume of 15 x 10^6 m^3, a total relief of 840 m, and a H/L of 0.31. The primary deposit, Maple Falls Event 1, was most likely emplaced 3370 ± 740 (4110-2600) yr B.P., based on analytically overlapping CRN ages from a pair of boulders in the middle third of the main debris field. Two CRN ages from the lowest third of the debris field returned discordant ages (5330 ± 1140 [6470-4190] yr B.P. and 7130 ± 1190 [8310-5940] yr B.P.) that appear to reflect some inheritance from being near the surface in the pre-slide source region. If valid, such inheritance may imply an unexpected degree of undisturbed flow during the event. The upper third of the debris field contains two prominent overlapping lobes of open-network boulder deposits that record at least one and possibly two younger events. A single CRN model age from a boulder in the upper of these lobes suggests that this deposit (Event 2) is the youngest in the study: 630 ± 400 (1030-230 yr B.P.), although further dating is needed to confirm this age. It remains unclear if the lower of the two upper lobes records a third, intermediate-age event.

The VZLC is composed of three overlapping debris lobes that record a succession of bedrock failures. Combined, the debris lobes cover 4.7 km^2 and have an estimated volume of 74.6 x 10^6 m^3 (Malick, 2018). The emplacement ages of Debris Lobe 2 (1330-1270 cal. yr B.P.) and Debris Lobe 3 (1300-1285 cal. yr B.P.) are constrained based on ^{14}C dating of organics contained in the landslide diamicton (Malick, 2018). These tight age constraints provided an excellent opportunity to test the reliability of CRN dating of these landslides. For the test, I collected CRN samples from three large boulders on Debris Lobe 2. The younger two of these ages (1580 ± 590 [2170-990] yr B.P and 1550 ± 800 [2340-750] yr B.P.) are consistent with, although significantly less precise than, the age established by Malick (2018). The third sample (2110 ± 750 [2860-1350] yr B.P.) is slightly older than Malick's age constraint, even at 2-sigma.

The CMS deposit appears to consist of a single large debris lobe (Pringle et al., 1998; Mickelson et al., 2020). Although occurring in close proximity to other landslides in this study, the CMS involves different bedrock (Paleozoic metasedimentary and metavolcanic rocks of the Chilliwack Group; Mickelson et al., 2020) and is significantly larger than the others. It has a minimum surface area of ~9 km^2 and an estimated volume of 280 x 10^6 m^3 (Carpenter, 1993). The most reliable emplacement age for the deposit is 2700-2150 cal. yr B.P. (Pringle et al., 1998), and thus potentially overlaps only with Event 1 of the Maple Falls deposit, the closest landslide in my study.

The wide range of emplacement ages for the Nooksack basin rock avalanches indicates they experienced different triggering events. The most likely triggers for these slides are (1) seismicity from the CSZ or the nearby Boulder Creek fault, (2) heavy rainfall or precipitation events, and (3) glacial debuttressing. Each of the landslide events documented here have ages that overlap with one or more seismic events from the CSZ or the Boulder Creek fault. The relatively broad dating uncertainties of the slide events, however, preclude having confidence in assigning seismicity as the most likely trigger for the slides. Given the historic observations of large landslides in the region (e.g., Oso; Keaton et al., 2014), precipitation in particular remains an equally viable triggering mechanism for some or all of these slides. Lack of detailed precipitation proxy records in the region, however, prevents testing this possibility. Given mid- to late-Holocene ages for most of the landslides, glacial debuttressing is only a viable triggering option for the oldest dated landslide, Middle Fork Event 1. The difference in timing between deglaciation (~15 ka) and the minimum timing established from the Middle Fork bog (~11 ka) suggests that this mechanism may also not be particularly likely. Other possible triggering mechanisms (e.g., eruptions of Mt. Baker, fluvial undercutting) do not appear viable based the age control for the events and the geographic setting of the source zones.

A primary limitation to this study was the resolution of the various dating techniques. Unlike at the VZLC (Malick, 2018), I was unable to obtain datable organic matter directly linked to the emplacement of the deposits I studied. Similarly, although the CRN exposure ages appear to provide a viable method of dating such landslide deposits, the analytic uncertainties preclude correlating them to individual triggering events with any confidence. Future studies could address this limitation by analyzing greater numbers of CRN samples that could help reduce the age uncertainties through statistical analysis of probability distributions, and future exposures (e.g., stream cuts, human excavations) may provide organic samples directly related to emplacement of the deposits (e.g., VZLC).

Literature Cited

Adams, J., 1990, Paleoseismicity of the Cascadia subduction zone—Evidence from turbidites off the Oregon-Washington margin: Tectonics, v. 9, p. 569–583.

Anderson, R.S., Molnar, P., and Kessler, M.A., 2006, Features of glacial valley profiles simply explained: Journal of Geophysical Research, v. 111, p. F01004, doi:10.1029/2005JF000344.

Atwater, B.F., Tuttle, M.P., Schweig, E.S., Rubin, C.M., Yamaguchi, D.K., Hemphill-Haley, E., 2004, Earthquake recurrence inferred from paleoseismology, Developments in Quarternary Science, v. 1, p. 331-350, doi:10.1016/S1571-0866(03)01015-7.

Atwater, B.F., and Hemphill-Haley, E., 1997, Recurrence Intervals for Great Earthquakes of the Past 3,500 Years at Northeastern Willapa Bay, Washington, U.S. Geological Survey Professional Paper 1576

Atwater, B.F., Carson, B., Griggs, G.B., Johnson, H.P., and Salmi, M.S., 2014, Rethinking turbidite paleoseismology along the Cascadia subduction zone: Geology, v. 42, p. 827–830, doi:10.1130/G35902.1.

Badger, T.C., 2002, Fracturing within anticlines and its kinematic control on slope stability: Environmental & Engineering Geoscience, v. 8, p. 19–33, doi:10.2113/gseegeosci.8.1.19.

Balco, G., Stone, J.O., Lifton, N.A. and Dunai, T.J., 2008, A complete and easily accessible means of calculating surface exposure ages or erosion rates from 10Be and 26Al measurements. Quaternary geochronology, 3(3), pp.174-195.

Balco, G., 2011, Contributions and unrealized potential contributions of cosmogenic-nuclide exposure dating to glacier chronology, 1990–2010: Quaternary Science Reviews, v. 30, p. 3–27, doi:10.1016/j.quascirev.2010.11.003.

Ballantyne, C.K., 2002. Paraglacial geomorphology. Quaternary Science Reviews 21: 1935–2017.

Blais-Stevens, A., and Clague, J.J., 2001, Paleoseismic signature in late Holocene sediment cores from Saanich Inlet, British Columbia: Marine Geology, v. 175, p. 131–148.

Booth, D.B., Troost, K.G., Clague, J.J., and Waitt, R.B., 2003, The Cordilleran Ice Sheet, *in* Developments in Quaternary Sciences, Elsevier, v. 1, p. 17–43, doi:10.1016/S1571-0866(03)01002-9.

Brock, F., Higham, T., Ditchfield, P., & Ramsey, C., 2010, Current Pretreatment Methods for AMS Radiocarbon Dating at the Oxford Radiocarbon Accelerator Unit (Orau), Radiocarbon, 52(1), 103-112, doi:10.1017/S0033822200045069.

Burns, W.J., and Madin, I.P., 2009, Protocol for Inventory Mapping of Landslide Deposits from Light Detection and Ranging (lidar) Imagery, Special Paper 42, Oregon Department of Geology and Mineral Industries, p. 36.

Burns, W.J., and Mickelson, K.A., 2016, PROTOCOL FOR DEEP LANDSLIDE SUSCEPTIBILITY MAPPING, Special Paper 48, Oregon Department of Geology and Mineral Industries, p. 69.

Carpenter, M.R., 1993, The Church Mountain sturzstrom (mega-landslide), near Glacier, Washington: Western Washington University Master of Science thesis, 71 pp.

Cary, C. M.; Easterbrook, D. J.; Carpenter, M. R., 1992, Postglacial mega-landslides in the North Cascades near Mt. Baker, Washington [abstract]: Geological Society of America Abstracts with Programs, v. 24, no. 5, p. 13.

Castleton, J.J., Moore, J.R., Aaron, J., Christi, M., Ivy-Ochs, S., 2016, Dynamics and legacy of 4.8 ka rock avalanche that dammed Zion Canyon, Utah, USA, GSA Today, Vol. 26, no. 6, pp. 4-9, doi:10.1130/GSATG269A.1.

Chmeleff, J., von Blankenburg, F., Kossert, K., & Jakob, D., 2010, Determination of the ^{10}Be half-life by multicollector ICP-MS and liquid scintillation counting. Nuclear Instruments and Methods in Physics Research Section B - Beam Interactions with Materials and Atoms, 268, 192–199.

Clark, D.H., and Clague, J.J., 2021, Glaciers, isostasy, and eustasy in the Fraser Lowland: A new interpretation of Late Pleistocene glaciation across the international boundary, Geological Society of America, Untangling the Quaternary Period—A Legacy of Stephen C. Porter, pp. 259-278.

Coe, J.A., Baum, R.L., Allstadt, K.E., Kochevar, B.F., Schmitt, R.G., Morgan, M.L., White, J.L., Stratton, B.T., Hayashi, T.A., and Kean, J.W., 2016, Rock-avalanche dynamics revealed by large-scale field mapping and seismic signals at a highly mobile avalanche in the West Salt Creek valley, western Colorado: Geosphere, v. 12, p. 607–631, doi:10.1130/GES01265.1.

Cook, T., 2017, What causes rock avalanches?, *Eos, 98*, https://doi.org/10.1029/2017EO071747. Published on 24 April 2017.

Cossart, E. and Fort, M., 2008, Consequences of landslide dams on alpine river valleys: examples and typology from the French Southern Alps, Norsk Geografisk Tidsskrift-Norwegian Journal of Geography, vol. 62(2), pp.75-88. https://doi.org/10.1080/00291950802094882.

Crider, J.G., 2009, THE 2009 RACEHORSE CREEK LANDSLIDE: FORENSIC DYNAMICS OF A LARGE, COMPLEX CATASTROPHIC MASS MOVEMENT: Geological Society of America Abstracts with Programs. Vol. 41, No. 7, p.498

Crosta, G.B., Frattini, P., 2001, Rainfall thresholds for triggering soil slips and debris flow, Proceedings of the 2nd EGS Plinius Conference on Mediterranean Storms, CNR GNDCI, Vol. 2547, p. 463-487.

Crozier, M. J., 1986, Landslides: Causes, Consequences and Environment, Croom Helm, 252 pp.
De Blasio, F.V., and Elverhøi, A., 2008, A model for frictional melt production beneath large rock avalanches: Journal of Geophysical Research, v. 113, p. F02014, doi:10.1029/2007JF000867.

Dragovich, J. D.; Norman, D. K.; Haugerud, R. A.; Pringle, P. T., 1997a, Geologic map and interpreted geologic history of the Kendall and Deming 7.5-minute quadrangles, western Whatcom County, Washington: Washington Division of Geology and Earth Resources Open File Report 97-2, 39 p., 3 pl.

Engebreston, D.C.; Easterbrook, D.J.; Kovanen, D.J., 1996. Triggering of very large, deep-seated, bedrock landslides by concentrated, shallow earthquakes in the North Cascades, WA [abstract]: Geological Society of America Abstracts with Programs, v. 28, no

Fischer, L., Amann, F., Moore, J.R., Huggel, C., 2010, Assessment of periglacial slope stability for the 1988 Tschierva rock avalanche (Piz Morteratsch, Switzerland), Engineering Geology, vol. 116(1–2), p. 32-43, https://doi.org/10.1016/j.enggeo.2010.07.005.

Francis, S.W., 2019, Quantifying the magnitude and spatial variability of bedrock erosion beneath the Sisters Glacier, Washington, using cosmogenic 3He concentrations. https://cedar.wwu.edu/wwuet/857/.

Gallach, X., Ravanel, L., Egli, M. et al., 2018, Timing of rockfalls in the Mont Blanc massif (Western Alps): evidence from surface exposure dating with cosmogenic 10Be, Landslides 15, 1991–2000, https://doi.org/10.1007/s10346-018-0999-8.

Goguel, J. (1978), Scale-dependent rockslide mechanisms, with emphasis on the role of pore fluid vaporization, in Rockslides and Avalanches, edited by B. Voight, pp. 693– 706, Elsevier, Amsterdam.

Goldfinger, C., Nelson, C.H., Morey, A.E., Johnson, J.R., Patton, J., Karabanov, E., Gutierrez-Pastor, J., Eriksson, A.T., Gracia, E., Dunhill, G., Enkin, R.J., Dallimore, A., and Vallier, T., 2012, Turbidite event history—Methods and implications for Holocene paleoseismicity of the Cascadia subduction zone: U.S. Geological Survey Professional Paper 1661–F, 170 p, 64 figures, available at http://pubs.usgs.gov/pp/pp1661/f

Goldfinger, C., Nelson, C.H., and Johnson, J.E., 2003a, Deep-water turbidites as Holocene earthquake proxies—The Cascadia subduction zone and northern San Andreas fault systems: Annali Geofisica, v. 46, p. 1169–1194.

Goldfinger, C., Nelson, C.H., and Johnson, J.E., 2003b, Holocene earthquake records from the Cascadia subduction zone and northern San Andreas fault based on precise dating of offshore turbidites: Annual Reviews of Earth and Planetary Sciences, v. 31, p. 555–577.

Goldfinger, C., Grijalva, K., Burgmann, R., and 8 others, 2008, Late Holocene rupture of the northern San Andreas Fault and possible stress linkage to the Cascadia subduction zone: Bulletin of the Seismological Society of America, v. 98, p. 861–889.

Guthrie, R. H., Friele, P., Allstadt, K., Roberts, N., Evans, S. G., Delaney, K. B., Roche, D., Clague, J. J., and Jakob, M., 2012, The 6 August 2010 Mount Meager rock slide-debris flow, Coast Mountains, British Columbia: characteristics, dynamics, and implications for hazard and risk assessment: Nat. Hazards Earth Syst. Sci., 12, 1277–1294, https:/doi.org/10.5194/nhess-12-1277-2012, 2012.

Habib, P., 1975, Production of gaseous pore pressure during rock slides, Rock Mech. Rock Eng., 7, 193– 197.

Harp, E. L. and Jibson, R. W., 1996, Landslides triggered by the 1994 Northridge, California earthquake. Seismological Society of America Bulletin, v. 86, p. 319– 332.

Heim, Albert, 1932, Bergsturz und Menschenleben: Zurich, Fretz & Wasmuth Verlag, 218 p.

Hewitt, K., Clague, J.J., and Orwin, J.F., 2008, Legacies of catastrophic rock slope failures in mountain landscapes: Earth-Science Reviews, v. 87, p. 1–38, doi:10.1016/j.earscirev.2007.10.002.

Highland, L., 2003, An account of preliminary landslide damage and losses resulting from the February 28, 2001, Nisqually, Washington, Earthquake, US Department of the Interior, US Geological Survey.

Highland, L.M., and Bobrowsky, Peter, 2008, The landslide handbook – A guide to understanding landslides: Reston, Virginia, U.S. Geological Survey Circular 1325, p. 129.

Hsü, K. J., 1975, Catastrophic debris streams (sturzstroms) generated by rockfalls, Geological Society of America Bulletin, vol. 86(1), pg. 129-140, https://doi.org/10.1130/0016-7606(1975)86<129:CDSSGB>2.0.CO;2

Hungr, O., and Evans, S.G., 2004, Entrainment of debris in rock avalanches: An analysis of a long run-out mechanism: Geological Society of America Bulletin, v. 116, p. 1240, doi:10.1130/B25362.1.

Hungr, O., Leroueil, S., and Picarelli, L., 2014, The Varnes classification of landslide types, an update: Landslides, v. 11, p. 167–194, doi:10.1007/s10346-013-0436-y.

Hyde, J. H. and Crandell, D. R., 1979, Postglacial volcanic deposits at Mount Baker, Washington, and potential hazards from future eruptions, Geological Survey Professional Paper 1022-C, No.: I 19.16:1022-C.

Iverson, R.M., George, D.L., Allstadt, K., Reid, M.E., Collins, B.D., Vallance, J.W., Schilling, S.P., Godt, J.W., Cannon, C.M., Magirl, C.S., Baum, R.L., Coe, J.A., Schulz, W.H., Bower, J.B., 2015, Landslide mobility and hazards: implications of the 2014 Oso disaster, Earth and Planetary Science Letters, vol. 412, pg. 197-208, ISSN 0012-821X, doi.org/10.1016/j.epsl.2014.12.020.

Ivy-Ochs, S., Poschinger, A.V., Synal, H.-A., Maisch, M., 2009, Surface exposure dating of the Flims landslide, Graubünden, Switzerland, Geomorphology, Vol. 103, Issue 1, pg. 104-112, ISSN 0169-555X, https://doi.org/10.1016/j.geomorph.2007.10.024.

Johnson, B.C., Campbell, C.S., and Melosh, H.J., 2016, The reduction of friction in long runout landslides as an emergent phenomenon: Journal of Geophysical Research: Earth Surface, v. 121, p. 881–889, doi:10.1002/2015JF003751.

Johnson, S.Y., 1984, Stratigraphy, age, and paleogeography of the Eocene Chuckanut Formation, northwest Washington: Canadian Journal of Earth Sciences, v. 21, p. 92–106, doi:10.1139/e84-010.

Keaton, J. R. Wartman, J., Anderson, S., Benoit, J., deLaChapelle, J., Gilbert, R., Montgomery, D..R., 2014, “The 22 March Oso Landslide, Snohomish County, WA; GEER Report Summary”. NSF Geotechnical Extreme Events Reconnaissance, 172 pp.

Keefer, D.K., 1984, Landslides caused by earthquakes: Geological Society of America Bulletin, v. 95, p. 406 - 421, 7 figs., 7 tables.

Keefer, D.K., 1994, The importance of earthquake-induced landslides to long-term slope erosion and slope-failure hazards in seismically active regions, Geomorphology and natural hazards, pp. 265-284 https://doi.org/10.1016/B978-0-444-82012-9.50022-0.

Kelsey, H. M., B. L. Sherrod, R. J. Blakely, and R. A. Haugerud, 2012, Holocene faulting in the Bellingham forearc basin: Upper-plate deformation at the northern end of the Cascadia subduction zone, J. Geophys. Res., 117, B03409, doi:10.1029/2011JB008816.

Korup, O., Seidemann, J., Mohr, C.H, 2019, Increased landslide activity on forested hillslopes following two recent volcanic eruptions in Chile, Nature Geoscience, 12, p. 284–289. https://doi.org/10.1038/s41561-019-0315-9.

Kovanen, D. J., 1996, Extensive late-Pleistocene alpine glaciation in the Nooksack River Valley, North Cascades, Washington: Western Washington University Master of Science thesis, 186 p.

Kramer, S.L., 1996, Geotechnical earthquake engineering: New Jersey, Prentice-Hall, 653 p.

LaHusen, S.R., Duvall, A.R., Booth, A.M., Grant, A., Mishkin, B.A., Montgomery, D.R., Struble, W., Roering, J.J., and Wartman, J., 2020, Rainfall triggers more deep-seated landslides than Cascadia earthquakes in the Oregon Coast Range, USA: Science Advances, v. 6, p. eaba6790, doi:10.1126/sciadv.aba6790.

Lapen, J. T., 2000, Geologic map of the Bellingham 1:100,000 quadrangle, Washington, Washington Department of Geology and Earth Resources, Open File Report 2000-5.

Larson, P.B., 2015, The Oso Landslide: Disaster Management Law in the Space Age, William & Mary Environmental Law and Policy Review, vol. 40, p. 335.

Leith, K., Moore, J. R., Loew, S., Krautblatter, M., 2013, Progressive rock slope failure resulting from fluvial incision and far-field stress changes in alpine landscapes, AGU Fall Meeting Abstracts, NH21A-1507, https://ui.adsabs.harvard.edu/abs/2013AGUFMNH21A1507L.

Lin, G. W., Chen, H., Hovius, N. et al., 2008, Effects of earthquake and cyclone sequencing on landsliding and fluvial sediment transfer in a mountain catchment. Earth Surface Processes and Landforms, 33, 1354–1373, doi:10.1002/esp1716.

Malick, Geoff, 2018, Geologic Development and Ongoing Activity of the Van Zandt Landslide Complex, Northwest WA, USA: Thesis (M.S), Western Washington University, Bellingham, WA.

Marc, O., Behling, R., Andermann, C., Turowski, J.M., Illien, L., Roessner, S., and Hovius, N., 2019, Long-term erosion of the Nepal Himalayas by bedrock landsliding: the role of monsoons, earthquakes and giant landslides: Earth Surface Dynamics, v. 7, p. 107–128, doi:10.5194/esurf-7-107-2019.

Marrero, S.M., Phillips, F.M., Borchers, B., Lifton, N., Aumer, R., Balco, G., 2016, Cosmogenic nuclide systematics and the CRONUScalc program, Quaternary Geochronology, Vol. 31, Feb. 2016, p. 160-187, doi.org/10.1016/j.quageo.2015.09.005.

McColl, S.T., 2012, “Paraglacial Rockslope Stability”: Thesis (PhD), University of Canterbury, Christchurch, New Zealand.

McDonough, P.W. ed., 2002, Nisqually, Washington, Earthquake of February 2001: Lifeline Performance, ASCE Publications, vol. 20.

McNutt, S.R., and Roman, D.C., 2015, Chapter 59 - Volcanic Seismicity, in Sigurdsson, H., McNutt, S.R., Houghton, B., Rymer, H., and Stix, J., The Encyclopedia of Volcanoes (Second Edition), Academic Press ISBN 9780123859389, p. 1011-1034, https://doi.org/10.1016/B978-0-12-385938-9.00059-6.

Melosh, H. J., 1979, Acoustic fluidization: A new geological process?, J. Geophys. Res., 84, 7513– 7520.

Meunier, P., Hovius, N. and Haines, A. J., 2007, Regional patterns of earthquake-triggered landslides and their relation to ground motion. Geophysical Research Letters, 34, L20408, doi:10.1029/2007GL031337.

Mickelson, K. A.; Contreras, T. A.; Gallin, W. N.; Jacobacci, K. E.; Slaughter, S. L., 2020, Landslide inventory of western Whatcom County, Washington: Washington Geological Survey Report of Investigations 42, 7 p. text, with an accompanying Esri file geodatabase.

Mock, C.J., 1996, Climatic Controls and Spatial Variations of Precipitation in the Western United States: Journal of Climate, v. 9, p. 1111–1125, doi:10.1175/1520-0442(1996)009<1111:CCASVO>2.0.CO;2.

Moen, W. S., 1962, Geology and mineral deposits of the north half of the Van Zandt quadrangle, Whatcom County, Washington: Washington Division of Mines and Geology Bulletin 50, 129 p., 4 pl.

Mustoe, G.E., Dillhoff, R.M., and Dillhoff, T.A., 2007, Geology and paleontology of the early Tertiary Chuckanut Formation, in Stelling, P., and Tucker, D.S., eds., Floods, Faults, and Fire: Geological Field Trips in Washington State and Southwest British Columbia: Geological Society of America Field Guide 9, p. 121–135, doi: 10.1130/2007.fl d009(06)

Nelson, C.H., Goldfinger, C. Vallier, T.L. McGann, M.L., and Kashgarian, M., l996, North to south variation in Cascadia Basin turbidite event history—Implications for paleoseismicity: Geological Society of America Abstracts with Programs, v. 28, no. 5, p. 95.

Nelson, C.H., and Goldfinger, C., 1999, Turbidite event stratigraphy and implications for Cascadia Basin paleoseismicity: Eos, Transactions of the American Geophysical Union, v. 80, p. 733.

Nishiizumi, K., Imamura, M., Caffee, M.W., Southon, J.R., Finkel, R.C. and McAninch, J., 2007, Absolute calibration of 10Be AMS standards. Nuclear Instruments and Methods in Physics Research Section B: Beam Interactions with Materials and Atoms, 258(2), pp.403-413.

Perkins, J.P., Roering, J.J., Burns, W.J., Struble, W., Black, B.A., Schmidt, K.M., Duvall, A. and Calhoun, N., 2018, Hunting for landslides from Cascadia's great earthquakes, Eos, 99(10.1029). https://doi.org/10.1029/2018EO103689.

Personius, S.F., Briggs, R.W., Nelson, A.R., Schermer, E.R., Maharrey, J.Z., Sherrod, B.L., Spaulding, S.A., and Bradley, L.-A., 2014, Holocene earthquakes and right-lateral slip on the left-lateral Darrington–Devils Mountain fault zone, northern Puget Sound, Washington: Geosphere, v. 10, p. 1482–1500, doi:10.1130/GES01067.1.

Petley, D.N. and Allison, R.J., 1997, The mechanics of deep-seated landslides, Earth Surface Processes and Landforms: The Journal of the British Geomorphological Group, vol. 22(8), pp. 747-758 https://doi.org/10.1002/(SICI)1096-9837(199708)22:8<747::AID-ESP767>3.0.CO;2-%23.

Porter, S.C., and Swanson, T.W., 1998, Radiocarbon Age Constraints on Rates of Advance and Retreat of the Puget Lobe of the Cordilleran Ice Sheet during the Last Glaciation: Quaternary Research, v. 50, p. 205–213, doi:10.1006/qres.1998.2004.

Pringle, P.T., Schuster, R.L., and Logan, R.L., 1998, New radiocarbon ages of major landslides in the Cascade Range, Washington, Washington Geology, v.26, p. 31-39.

Reimer, P., Austin, W., Bard, E., Bayliss, A., Blackwell, P., Bronk Ramsey, C., . . . Talamo, S., 2020, The IntCal20 Northern Hemisphere Radiocarbon Age Calibration Curve (0–55 cal kBP). Radiocarbon, 62(4), 725-757. doi:10.1017/RDC.2020.41

Riedel, J.L., Haugerud, R.A., and Clague, J.J., 2007, Geomorphology of a Cordilleran Ice Sheet drainage network through breached divides in the North Cascades Mountains of Washington and British Columbia: Geomorphology, v. 91, p. 1–18, doi:10.1016/j.geomorph.2007.01.021.

Roccati, A., Faccini, F., Luino, F., Ciampalini, A., & Turconi, L., 2019, Heavy rainfall triggering shallow landslides: A susceptibility assessment by a GIS-approach in a Ligurian Apennine Catchment Italy, Water, v. 11(3), p. 605. https://doi.org/10.3390/w11030605

Scott, K.M., Tucker, D.S., Riedel, J.L., Gardner, C.A., and McGeehin, J.P., 2020, Latest Pleistocene to present geology of Mount Baker Volcano, northern Cascade Range, Washington: U.S. Geological Survey Professional Paper 1865, 170 p., https://doi.org/10.3133/pp1865.

Sepúlveda, S.A., Murphy, W., Jibson, R.W., and Petley, D.N., 2005, Seismically induced rock slope failures resulting from topographic amplification of strong ground motions: The case of Pacoima Canyon, California: Engineering Geology, v. 80, p. 336–348, doi:10.1016/j.enggeo.2005.07.004.

Sharma, P., Kubik, P.W., Fehn, U., Gove, H.E., Nishiizumi, K., Elmore D., 1990, Development of 36Cl standards for AMS, Nuclear Instruments and Methods in Physics Research Section B: Beam Interactions with Materials and Atoms, v. 52, 3–4, p. 410-415, ISSN 0168-583X, https://doi.org/10.1016/0168-583X(90)90447-3.

Sherrod, B. L., Barnett, E., Schermer, E., Kelsey, H.M., Hughes, J., Foit, F.F., Weaver, C.C., Haugerud, R., and Hyatt. T., 2013, Holocene Tectonics and Fault Reactivation in the Foothills of the North Cascade Mountains, Washington. Geosphere, July, GES00880.1.

Slaughter, S.L., Burns W.J., Mickelson, K.A., Jacobacci K.E., Biel, A., and Contreras, T.A., 2017, Protocol for Landslide Inventory Mapping from Lidar Data in Washington State, Bulletin 82, Washington Geological Survey, p. 35.

Struble, W.T., Roering, J.J., Black, B.A., Burns, W.J., Calhoun, N., and Wetherell, L., 2020, Dendrochronological dating of landslides in western Oregon: Searching for signals of the Cascadia A.D. 1700 earthquake: GSA Bulletin, v. 132, p. 1775–1791, doi:10.1130/B35269.1.

Stuiver, M., Reimer, P.J., and Reimer, R.W., 2019, CALIB 7.1 [WWW program] at http://calib.org, accessed 2019-2-16.

Valagussa, A., Marc, O., Frattini, P., and Crosta, G.B., 2019, Seismic and geological controls on earthquake-induced landslide size: Earth and Planetary Science Letters, v. 506, p. 268–281, doi:10.1016/j.epsl.2018.11.005.

Varnes, D.J., 1978, Slope movement types and processes. In: Schuster RL, Krizek RJ (eds) Landslides, analysis and control, special report 176: Transportation research board, National Academy of Sciences, Washington, DC., pp. 11–33.

Veblen, T.T. and Ashton, D.H., 1978, Catastrophic influences on the vegetation of the Valdivian Andes, Chile. Plant Ecology, vol. 36(3), pp.149-167. https://doi.org/10.1007/BF02342598.

Voight, B., Janda, R.J., Glicken, H., Douglass, P.M., 1983, Nature and mechanics of the Mount St Helens rockslide-avalanche of 18 May 1980, Géotechnique 33, No. 3, p. 243-273.

WA DNR, 2014, Shallow Landslide Hazard Forecast Map: https://www.dnr.wa.gov/slhfm (accessed January 2019).

Wartman, J., Dunham, L., Tiwari, B., Pradel, D., 2013, Landslides in Eastern Honshu Induced by the 2011 Tohoku Earthquake, Bulletin of the Seismological Society of America, v. 103 (2B): p. 1503–1521, doi: https://doi.org/10.1785/0120120128

Washington Geological Survey, 2017, Seismic scenario catalog—GIS data, August 2017: Washington Geological Survey, version 1.0, originally created March 2010. https://data-wadnr.opendata.arcgis.com/documents/seismic-scenario-catalog/about.

Washington House of Representatives, 2015, SB 5088, Concerning a Geological Hazards Assessment, p. 4, http://leg.wa.gov/House/Committees/Documents/sinedie2015.pdf (accessed January 2019).

Waythomas, C.F., 2013, Landslides at stratovolcanoes initiated by volcanic unrest, in Clague, J.J. and Stead, D. eds., Landslides, Cambridge, Cambridge University Press, p. 37–49.

Worden, C.B., Thompson, E.M., Hearne, M., Wald, D.J., 2020, ShakeMap Manual Online: technical manual, user’s guide, and software guide, U. S. Geological Survey, http://usgs.github.io/shakemap/, doi:10.5066/F7D21VPQ.

Wieczorek, G.F., 1996, Landslide triggering mechanisms, *in* Turner A.K., and Schuster, R.L., eds., Landslides— investigation and mitigation: Washington, D.C., Transportation Research Board, National Research Council, National Academy Press, Special Report 247, p. 76–90.

Wright, H.E., 1967, A square-rod piston sampler for lake sediments. Sediment. Res. 37, 975–976.

Yin, Y., Sun, P., Zhu, J. et al., 2011, Research on catastrophic rock avalanche at Guanling, Guizhou, China. Landslides, vol. 8, p. 517–525, https://doi.org/10.1007/s10346-011-0266-8.

Zdanowicz, C.M., Zielinski, G.A., and Germani, M.S., 1999, Mount Mazama eruption: Calendrical age verified and atmospheric impact assessed: Geology, v. 27, no. 7, p. 621-624, https://doi.org/10.1130/0091-7613(1999)027<0621:MMECAV>2.3.CO;2

Zhang, M., Yin, Y., Wu, S., Zhang, Y., Han, J., 2011, Dynamics of the Niumiangou Creek rock avalanche triggered by 2008 Ms 8.0 Wenchuan earthquake, Sichuan, China: Landslides, v. 8, p. 363–371, doi:10.1007/s10346-011-0265-9.

Zhang, M., Yin, Y., McSaveney, M., 2016, Dynamics of the 2008 earthquake-triggered Wenjiagou Creek rock avalanche, Qingping, Sichuan, China: Engineering Geology, v. 200, p. 75–87, doi:10.1016/j.enggeo.2015.12.008.

Tables

Site	Sample ID	Lab code	Material, core depth, or sample location	Reference	^{14}C age[1] (yr)	± yr (1σ)	Calibrated age ranges[2] 2σ (yr B.P.)			
							Min	Max	Prob.	Median prob.
Racehorse Creek	M	D-AMS 038112	Small twig ~0.83 m below bog surface; sediment core RHCLS-03; RHC small bog	*This study*	1480	21	1309	1390	1.000	1358
	V	D-AMS 038114	~5 cm long wood ~1.86 m below bog surface; sediment core RHCLS-05; RHC large bog	*This study*	3065	26	3185 3209	3189 3361	0.009 0.991	3285
	34c	Beta-96308	Sample from innermost 10 rings of cedar log having about 65 rings and buried in silt under Racehorse Creek rockslide deposit	Pringle et al. (1998)	3840	70	3993 4079	4038 4421	0.034 0.966	4250
Middle Fork Nooksack	F	D-AMS 038115	Small twig ~2 cm above refusal layer; ~6.13 m below bog surface; sediment core MFNLS-01	*This study*	8816	41	9686 9986 10060	9964 10043 10146	0.773 0.071 0.157	9855
	P8-71A	D-AMS 038116	Small twig ~4 cm above refusal layer; ~6.11 m below bog surface; sediment core MFNLS-01	*This study*	8855	39	9759	10167	1.000	9983
Van Zandt[3] *(Lobe 3)*	KA-01*	176215	Terminal growth ring of *in situ* intact log	Malick, 2018	1270	35	1077 1121 1175	1095 1163 1287	0.028 0.140 0.832	1218
	RL-03*	N114149	Small twig (2.5 mm long) in diamicton	Malick, 2018	1460	60	1282 1433 1449 1485	1421 1444 1475 1515	0.917 0.009 0.037 0.037	1351
Van Zandt[3] *(Lobe 2)*	RT-01*	175467	Terminal growth ring of *in situ* log with bark	Malick, 2018	1375	25	1193 1273 1324	1198 1314 1344	0.012 0.898 0.090	1296
	RT-04	175468	Outer growth ring of *in situ* fragmented log	Malick, 2018	1400	25	1288	1346	1.000	1308
	BV-05	N114154	Small twig (2.5 mm long) in diamicton	Malick, 2018	1385	30	1194 1275	1196 1348	0.004 0.996	1301
	BV-07	N114145	Wood fragment in diamicton	Malick, 2018	1550	35	1359	1520	1.000	1439
	WL-01	N114158	Small twig (3.0 mm long) in diamicton	Malick, 2018	1355	25	1178 1189 1263	1186 1208 1308	0.034 0.113 0.853	1288
	WL-04	N114157	Wood fragment in diamicton	Malick, 2018	1555	30	1371	1521	1.000	1448
Church Mountain Sturzstrom	mbr	Unknown	Age from Cary and others (1992). Wood from Douglas fir buried in rockslide-debris avalanche deposit, right bank Glacier Creek at Mount Baker Rim.	Cary and others (1992)	2890	90	2784 2841 3299	2829 3251 3325	0.035 0.947 0.018	3033
	gal	Unknown	Age from Carpenter (1993) from wood at Gallup Creek.	Carpenter (1993)	2450	80	2350	2723	1.000	2533
	mbr2	Unknown	Age from Carpenter (1993) from wood sample at Mount Baker Rim.	Carpenter (1993)	2710	80	2711 3014 3040	3007 3035 3058	0.984 0.008 0.007	2829
	CMA-92-1	Beta-58566	Sample from outer 10 rings under bark of a cedar log lying under CMA-92-2	Pringle et al. (1998)	2340	60	2153 2296 2592 2637	2264 2515 2614 2697	0.162 0.743 0.028 0.067	2376
	CMA-92-2	Beta-58567	Sample from outer 15 rings under bark of a Douglas fir sample *mbr* above (Pringle et al., 1998).	Pringle et al. (1998)	2340	60	2153 2296 2592 2637	2264 2515 2614 2697	0.162 0.743 0.028 0.067	2376

[1] Laboratory ^{14}C age, one standard deviation.

[2] 2-σ calibrated age ranges and probabilities. yr B.P. (before CE 1950; Calib v.8.2 Reimer et al., 2020).

[3] Van Zandt (Lobe 3) and Van Zandt (Lobe 2) of Malick (2018).

*Most reliable samples, as identified by Malick (2018).

Table 1 – Compiled Radiocarbon (^{14}C) ages from the Nooksack basin rock avalanche deposits.

Sample	Lab ID	Latitude	Longitude	Elevation (m amsl)	Mass Qtz (g)	^{10}Be/^{9}Be (10^{-14}) [1]	Shielding	^{10}Be (10^{4} atm g^{-1}/qtz)	Exposure age (yr Before 2021) [2]	Adjusted Exposure age (yr Before 1950) 2-σ [3]
RHC-01	202100407	48.8841066	-122.1458748	138	20.6385	5.362	0.986704	4.341	8877 ± 793	8806 ± 1586
RHC-02	202100408	48.8841806	-122.1458135	139	18.8052	2.895	0.998180	2.565	5135 ± 564	5082 ± 1128
RHC-03	202100410	48.8837500	-122.1447000	149	12.4904	1.651	0.998180	2.205	4363 ± 874	4292 ± 1748
RHC-06	202100421	48.8795616	-122.1456477	125	21.7989	2.475	0.987783	1.897	3871 ± 450	3800 ± 900
MFN-02	202100411	48.8300593	-122.0923034	757	12.6432	2.323	0.975177	3.070	3676 ± 450	3605 ± 900
MFN-03	202100412	48.8295946	-122.0921602	756	13.3644	2.445	0.968474	3.047	3650 ± 442	3579 ± 884
MFN-04	202100413	48.8317389	-122.1204972	200	22.0189	5.443	0.985122	4.111	7707 ± 651	7636 ± 1302
MFN-05	202100414	48.8294717	-122.1217763	186	23.1533	6.884	0.993252	4.952	9300 ± 699	9229 ± 1398
MF-01	202100415	48.9114468	-122.0540288	390	22.1496	2.814	0.985738	2.128	3439 ± 370	3368 ± 740
MF-02	202100417	48.9108500	-122.0541833	402	21.8967	2.765	0.991888	2.107	3379 ± 353	3308 ± 706
MF-03	202100418	48.9067883	-122.0510944	544	17.6431	0.5503	0.991300	0.5197	703 ± 200	632 ± 400
MF-04	202100419	48.9231587	-122.0588639	176	21.4929	3.599	0.995393	2.797	5405 ± 570	5334 ± 1140
MF-05	202100420	48.9226995	-122.0599739	176	21.9845	4.986	0.995432	3.785	7196 ± 593	7125 ± 1186
VZLC-01	202100423	48.7997180	-122.1656863	142	21.8862	1.369	0.951706	1.046	2176 ± 376	2105 ± 752
VZLC-02	202100424	48.8003511	-122.1667259	155	21.9733	1.103	0.989528	0.8350	1654 ± 295	1583 ± 590
VZLC-03	202100425	48.8010708	-122.1681467	162	16.7385	0.8315	0.994804	0.8261	1618 ± 397	1547 ± 794

[1] Isotopic analysis was conducted at PRIME Laboratory; ratios were normalized against standard 07KNSTD3110 with an assumed ratio of 2850 x 10^{-15} (Nishiizumi et al., 2007).

[2] Exposure ages calculated using the CRONUS calculator (Balco et al., 2008) and assuming a ^{10}Be half-life of 1.36 ± 0.07 Myr (Nishiizumi et al., 2007), an attenuation length scale of 160 g/cm^{2}, rock density of 2.552 g/cm^{3}, and the spallation scaling scheme of Lal (1991) and Stone (2000).

[3] CRN ages adjusted to "years before 1950" (yr B.P.) to compare with calibrated ^{14}C years B.P. Uncertainties reported to 2-σ.

Table 2 – Cosmogenic Radionuclide (CRN) exposure dating results for rock samples (n=16) collected from boulders on four Nooksack River basin rock avalanche deposits: Racehorse Creek (RHC), Middle Fork Nooksack (MFN), Maple Falls (MF), and Van Zandt Landslide Complex (VZLC).

Source Zone	**Racehorse Creek**	**Middle Fork**	**Maple Falls**
Area (km^2)	0.73	0.75	0.38
Void Volume (m^3)	20.3 x 10^6	32 x 10^6	11.4 x 10^6
Maximum Depth (m)	60	100	50
Bedrock Orientation (strike/dip)	230/28	135/51	315/38
Debris Field			
Area (km^2)	2.7	4.0	1.8
Volume (m^3)	19.5 x 10^6	34 x 10^6	15 x 10^6
Maximum Apparent Thickness (m)	30	80	50
Max. Runout (km)	3.3	4.4	2.8
H/L (m/m)	0.17	0.25	0.31

Table 3 – Summary data table for the Racehorse Creek, Middle Fork Nooksack and Maple Falls landslides. See section 4.0 Results for more details. H/L = height-to-length ratio.

Landslide Event	(Timing)	Overlapping Earthquake	(Timing)
RHC	(4420-3990 cal. yr B.P.)[1]	CSZ - T9	(4280-3920 cal. yr B.P.)[2]
MFN - Event 1	(10170-9690 cal. yr B.P.)[*]	CSZ - T18	(9980-9560 cal. yr B.P.)[2]
MFN - Event 2	(4510-2700 yr B.P.)[*]	CSZ - T9	(4280-3920 cal. yr B.P.)[2]
		CSZ - T8	(3600-3290 cal. yr B.P.)[2]
		CSZ - T7	(3160-2870 cal. yr B.P.)[2]
		BCF - B	(3190-2980 cal. yr B.P.)[3]
MF - Event 1	(4110-2600 yr B.P.)[*]	CSZ - T9	(4280-3920 cal. yr B.P.)[2]
		CSZ - T8	(4280-3920 cal. yr B.P.)[2]
		CSZ - T7	(3160-2870 cal. yr B.P.)[2]
		CSZ - T6	(2670-2390 cal. yr B.P.)[2]
		BCF - B	(3190-2980 cal. yr B.P.)[3]
MF - Event 2	(1030-230 yr B.P.)[*]	CSZ - T3	(910-680 cal. yr B.P.)[2]
		CSZ - T2	(570-380 cal. yr B.P.)[2]
		CSZ - T1	(370-140 cal. yr B.P.)[2]
		BCF - C	(910-740 cal. yr B.P.)[3]
VZLC - Debris Lobe 2	(1330-1270 cal. yr B.P.)[4]	CSZ - T4	(1350-1120 cal. yr B.P.)[2]
CMS	(2700-2150 cal. yr B.P.)[1]	CSZ - T6	(2670-2390 cal. yr B.P.)[2]

1 – Pringle et al., 1998.
2 – Goldfinger et al., 2012.
3 – Sherrod et al., 2013.
4 – Malick, 2018.
** – This study.*

Table 4 – The best available timings for the six dated landslide events of the Nooksack basin rock avalanche deposits. Events included are the Racehorse Creek (RHC), Middle Fork (MFN) - Event 1, Middle Fork (MFN) - Event 2, Maple Falls (MF) - Event 1, Maple Falls (MF) - Event 2, Van Zandt (VZLC) - Debris Lobe 2, and Church Mountain (CMS).

Figures

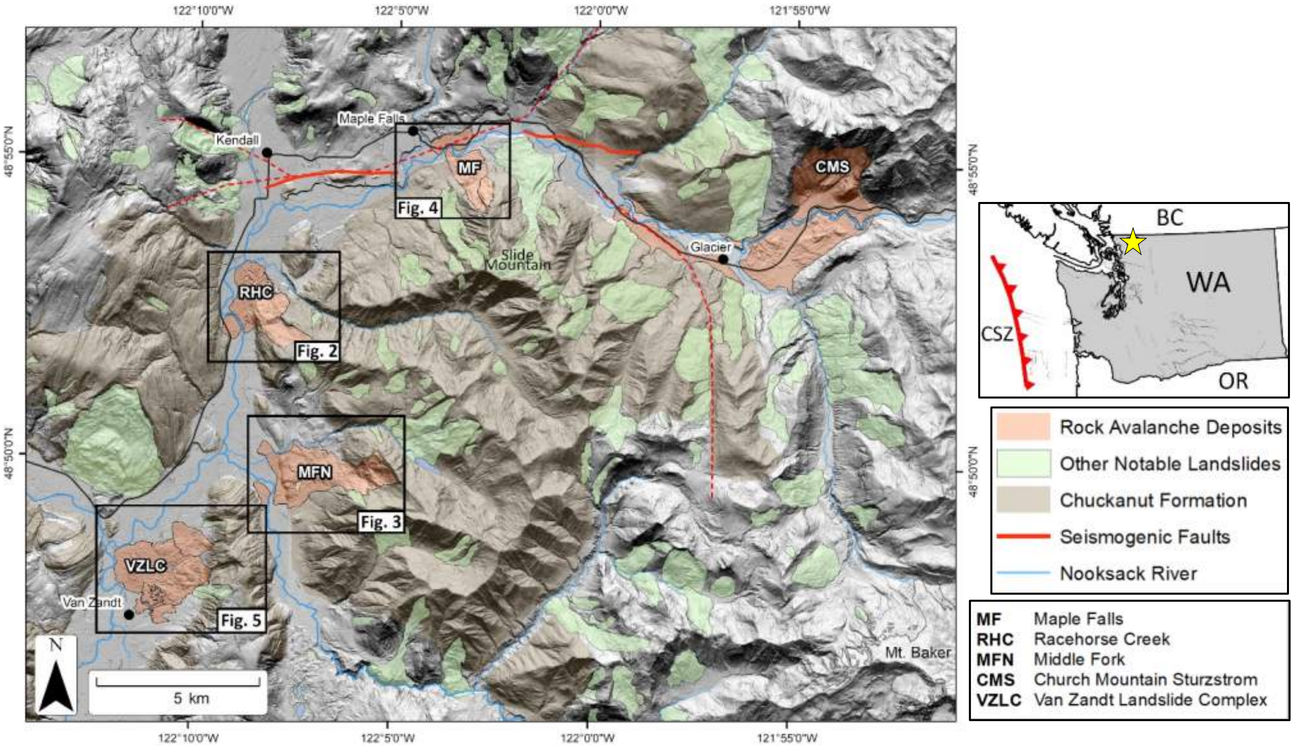

Figure 1 - Lidar hillshade map showing large landslide deposits in the northern portion of the Nooksack River basin. The rock avalanche deposits considered in this study are highlighted in orange, other notable landslides are shown in green (Mickelson et al., 2020). Seismogenic faults, including the Boulder Creek fault (Sherrod et al., 2013) and the Cascadia Subduction Zone interface (inset map; Goldfinger et al., 2008), are indicated by red lines. Also shown are Mount Baker Highway (black line), the three forks of the Nooksack River (blue lines), and the location of the stratovolcano Mount Baker (bottom-right). Lidar data (2017 North Puget Sound; WGS, 2017).

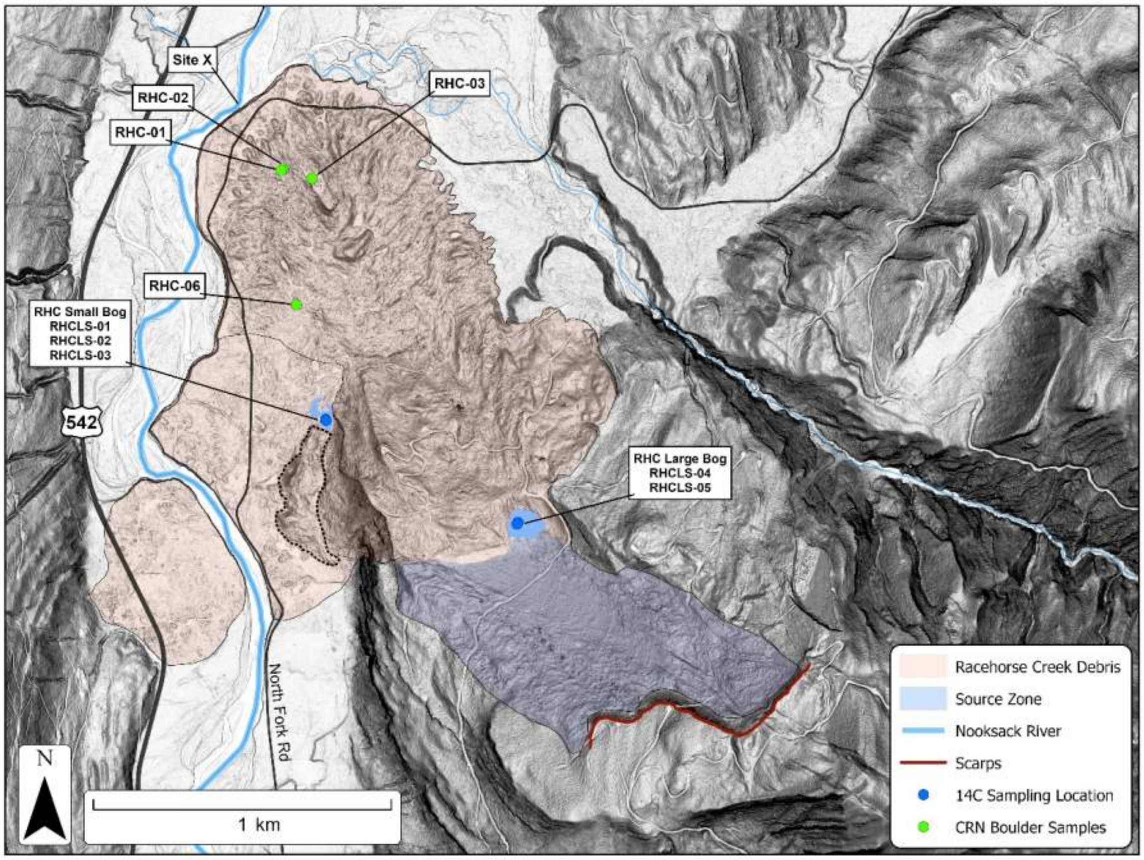

Figure 2 – Lidar slopeshade map of the Racehorse Creek landslide deposit. Shaded areas indicate the debris field (pink) and the source zone (purple). Bog coring locations are indicated by blue circles and locations of boulders for CRN dating are shown with green circles. Dashed line indicates a debris mound located within the lateral debris mass that is referred to in the text. Lidar data (2017 North Puget Sound; WGS, 2017).

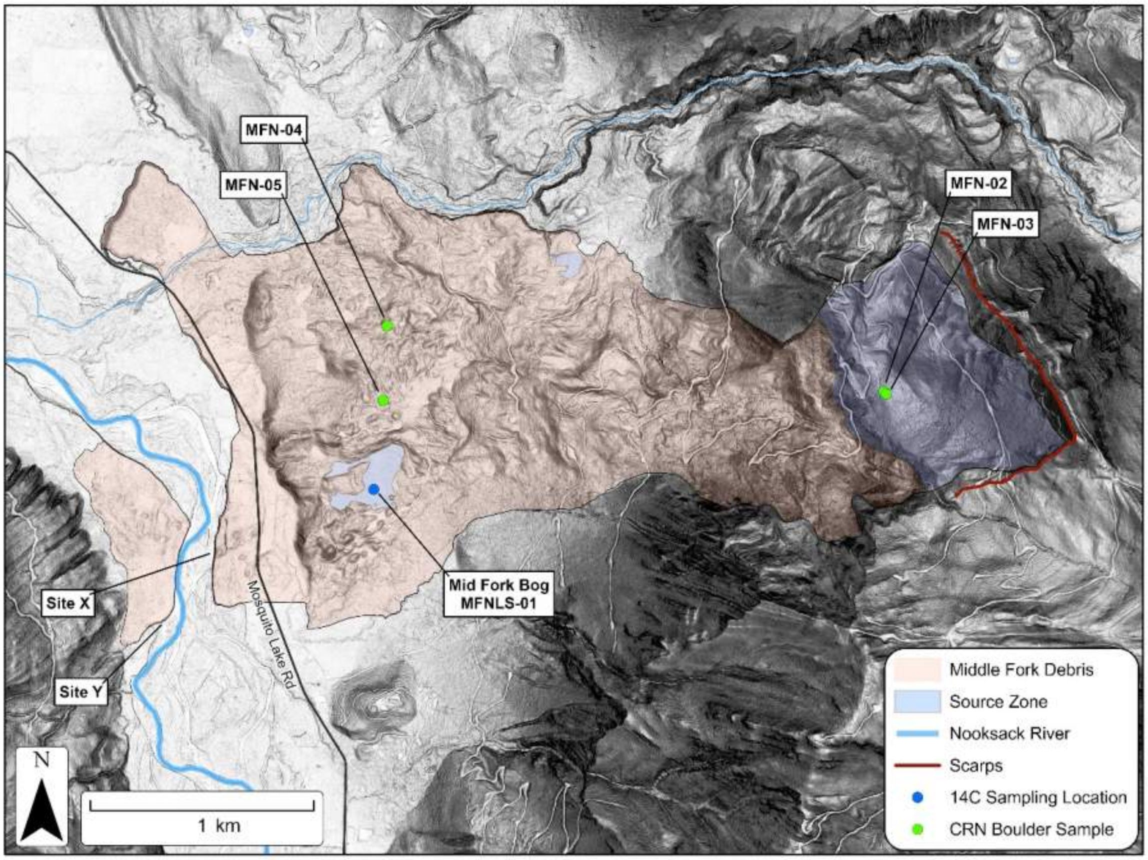

Figure 3 –Lidar slopeshade map of the Middle Fork landslide deposit. Shaded areas indicate the debris field (pink) and the source zone (purple). The location of the Middle Fork bog is indicated by blue shading, and the location of the sediment core MFNLS-01 is shown with a blue circle. CRN boulder locations are shown with green circles. Site X and Site Y are river cut-bank debris exposure locations referenced in text. Lidar data (2017 North Puget Sound; WGS, 2017).

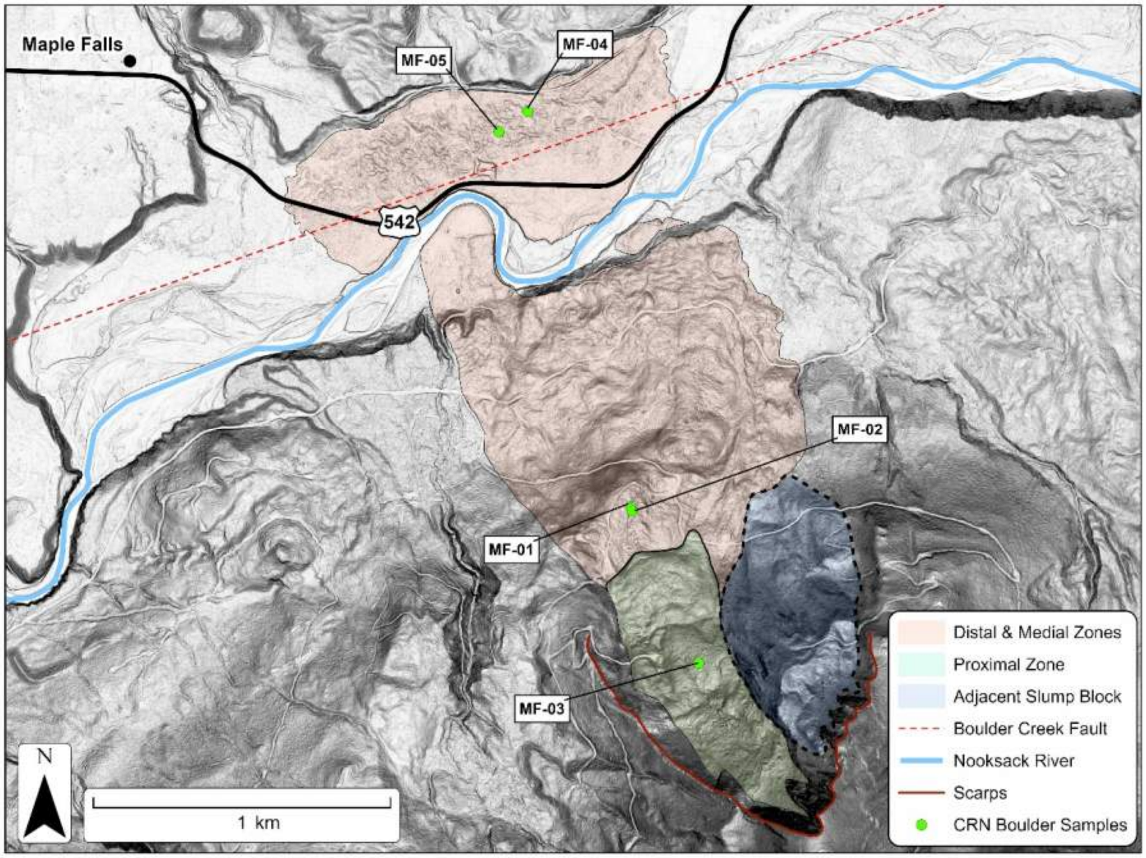

Figure 4 – Lidar slopeshade map of the Maple Falls landslide deposit. Shading indicates the debris field divided into distal and medial zones (pink), the proximal zone (green), and an adjacent slump block (purple). The approximate location of the Boulder Creek Fault (Sherrod et al., 2013) is indicated by the red dashed line. CRN boulder locations are shown with green circles. Lidar data (2017 North Puget Sound; WGS, 2017).

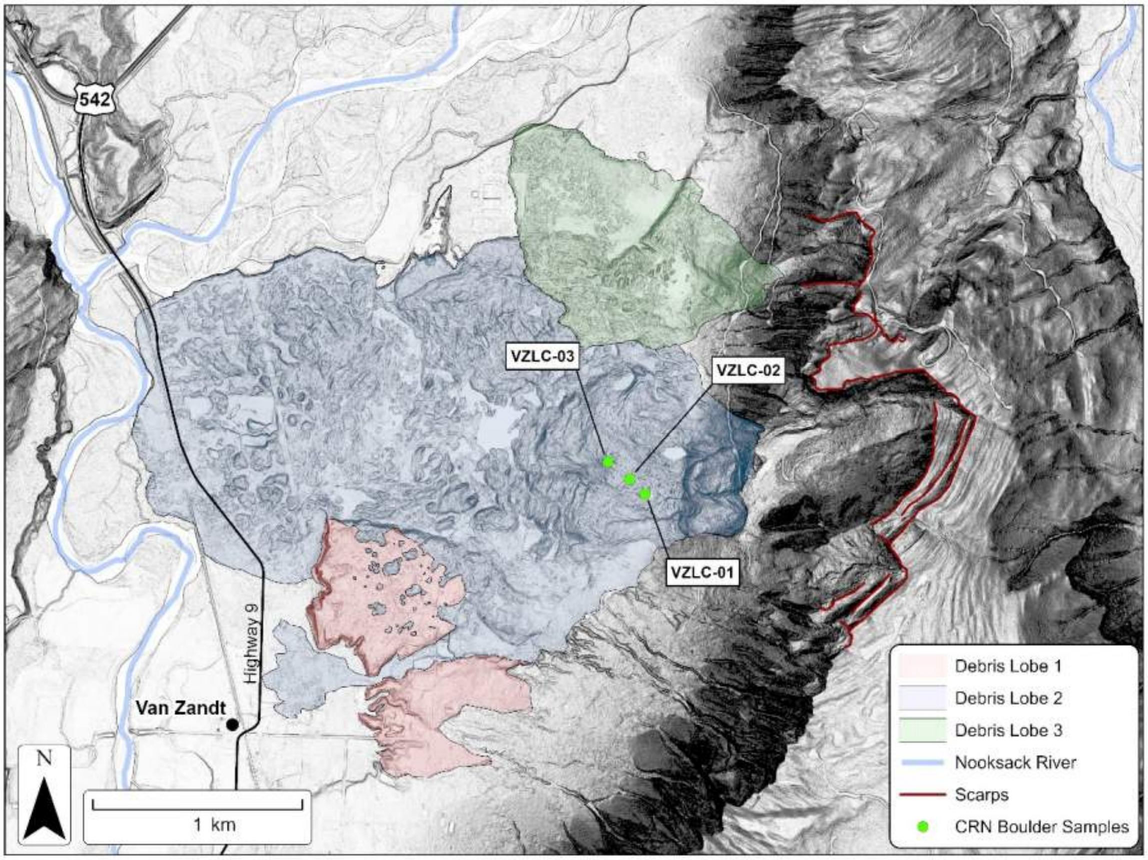

Figure 5 - The Van Zandt Landslide Complex (VZLC) as mapped by Malick (2018). The three lobes of the debris field Debris Lobe 1 (pink), Debris Lobe 2 (blue), and Debris Lobe 3 (green). CRN samples collected during this study are indicated by green circles. Lidar data (2017 North Puget Sound; WGS, 2017).

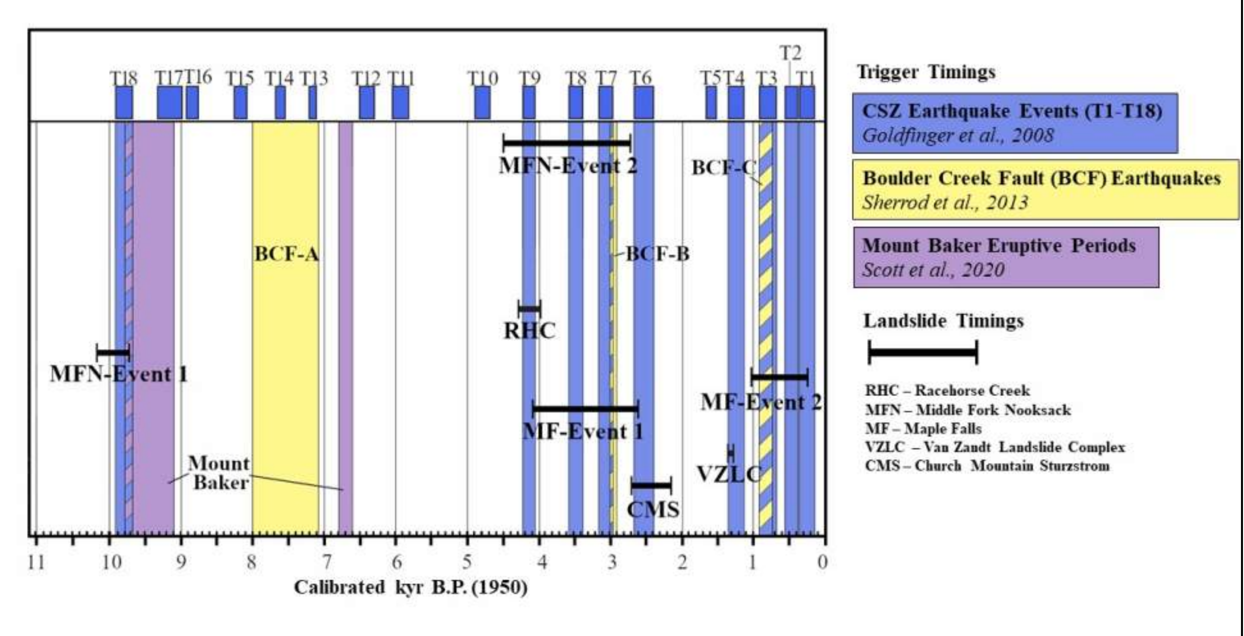

Figure 6 –Best available landslide timing constraints (horizontal black bars) overlain on timings of potential triggering mechanisms (vertical bars). Bar width indicates 2-σ analytic uncertainties. Cascadia Subduction Zone (CSZ) earthquakes (Events T1-T18) by Goldfinger et al. (2012) shown in blue. Bars are extended down to show overlap with landslide timings (see Table 4). Boulder Creek Fault (BCF) Earthquakes A, B, and C, (Sherrod et al., 2013) are shown in yellow. Two major post-glacial eruptive periods of Mount Baker shown in purple (Scott et al., 2020). Van Zandt Landslide Complex (VZLC) timings are provided by Malick (2018). Church Mountain Sturzstrom (CMS) timings are provided by Pringle et al. (1998), and Racehorse Creek timings are provided by Pringle et al. (1998).

Appendix A – Supplementary CRN data

ID	Holder	Name	^{10}Be/^{9}Be (10^{-15})	Uncertainty (10^{-15})	% Uncertainty	Max ^{9}Be Current (nanoAmps)	Min ^{9}Be Current (nanoAmps)	Avg. ^{9}Be Current (nanoAmps)	Fraction of Standard Current	Total ^{10}Be counts
202100407	162253	RHC-01	55.67	4.30	7.7	4737	3123	4276	0.643	172
202100408	162254	RHC-02	31.01	2.92	9.4	5016	3785	4698	0.706	115
202100409	162255	UVM-A	137.30	6.54	4.8	4918	3464	4392	0.660	473
202100410	162256	RHC-03	18.57	3.18	17.1	5455	4631	5182	0.779	69
202100411	162257	MFN-02	25.29	2.63	10.4	4955	4534	4766	0.716	94
202100412	162258	MFN-03	26.50	2.74	10.3	4757	4109	4568	0.687	95
202100413	162259	MFN-04	56.48	4.07	7.2	4807	3492	4472	0.672	199
202100414	162260	MFN-05	70.90	4.44	6.3	5189	4367	4821	0.725	266
202100415	162261	MF-01	30.20	2.77	9.2	5290	4878	5111	0.768	121
202100416	162262	BLK	2.06	0.65	31.6	5433	3925	4881	0.734	10
202100417	162263	MF-02	29.71	2.62	8.8	5541	4591	5164	0.776	131
202100418	162264	MF-03	7.56	1.41	18.6	5024	4526	4861	0.730	29
202100419	162265	MF-04	38.05	3.49	9.2	4951	2734	3937	0.592	121
202100420	162266	MF-05	51.92	3.61	6.9	5482	4929	5209	0.783	213
202100421	162267	RHC-06	26.81	2.65	9.9	5211	4384	4912	0.738	104
202100422	162268	UVM-A	152.49	6.35	4.2	5337	5053	5192	0.780	625
202100423	162269	VZLC-01	15.75	2.21	14.1	4350	3087	4056	0.609	51
202100424	162270	VZLC-02	13.08	1.81	13.8	5213	4806	5104	0.767	53
202100425	162271	VZLC-03	10.37	1.91	18.4	4709	3845	4498	0.676	37

Table 1 - ^{10}Be-CRN Accelerator Mass Spectrometry (AMS) results. Table prepared by Thomas Woodruff at Purdue Rare Isotope Measurement (PRIME) Lab. Significant Digits: If leading digit in uncertainty is 1 or 2 retain 2 digits otherwise retain 1. Ratios have same number of digits as corresponding uncertainty. References: Sharma P., et al (1990). Nucl. Inst. And Meth. B, 52(3-4), 410-415.

Sample Name	Theta (space-delineated degree list)	Horizon (space-delineated degree list)	Direction of Dip (degrees)	Dip Angle (degrees)	Snow Shielding	Latitude (decimal degrees)	Longitude (decimal degrees)	Elevation (meters)	Pressure (hPa)	Atmospheric Pressure or Elevation (select one)	Shielding
RHC-01	0 45 90 135 180 225 270 315	2 9 11 12 5 5 9 8	249	25	-	48.9114468	-122.0540288	138	-	Elevation	0.986704
*RHC-02	0 45 90 135 180 225 270 315	2 9 11 12 5 5 9 8	0	0	-	48.9108500	-122.0541833	139	-	Elevation	0.998180
*RHC-03	0 45 90 135 180 225 270 315	2 9 11 12 5 5 9 8	0	0	-	48.9067883	-122.0510944	149	-	Elevation	0.998180
RHC-06	0 45 90 135 180 225 270 315	0 5 10 12 3 7 10 7	145	24	-	48.8294717	-122.1217763	125	-	Elevation	0.987783
MFN-02	0 45 90 135 180 225 270 315	9 26 28 18 18 2 1 2	338	22	-	48.9231587	-122.0588639	757	-	Elevation	0.975177
MFN-03	0 45 90 135 180 225 270 315	8 21 29 20 19 3 2 5	235	30	-	48.9226995	-122.0599739	756	-	Elevation	0.968474
MFN-04	0 45 90 135 180 225 270 315	15 18 21 25 7 9 6 6	178	14	-	48.8841066	-122.1458748	200	-	Elevation	0.985122
*MFN-05	0 45 90 135 180 225 270 315	11 9 20 19 5 7 6 6	0	0	-	48.8841806	-122.1458135	186	-	Elevation	0.993252
MF-01	0 45 90 135 180 225 270 315	8 4 9 20 26 16 9 6	10	23	-	48.8837500	-122.1447000	390	-	Elevation	0.985738
MF-02	0 45 90 135 180 225 270 315	9 7 3 20 18 15 12 9	0	0	-	48.8795616	-122.1456477	402	-	Elevation	0.991888
MF-03	0 45 90 135 180 225 270 315	9 7 3 20 18 15 12 9	250	11	-	48.8300593	-122.0923034	544	-	Elevation	0.991300
MF-04	0 45 90 135 180 225 270 315	13 11 9 14 17 2 5 8	150	9	-	48.8295946	-122.0921602	176	-	Elevation	0.995393
MF-05	0 45 90 135 180 225 270 315	13 11 9 14 17 2 5 8	0	0	-	48.8317389	-122.1204972	176	-	Elevation	0.995432
VZLC-01	0 45 90 135 180 225 270 315	0 17 24 17 5 5 5 5	242	38	-	48.7997180	-122.1656863	142	-	Elevation	0.951706
VZLC-02	0 45 90 135 180 225 270 315	0 19 18 22 14 5 5 5	0	0	-	48.8003511	-122.1667259	155	-	Elevation	0.989528
VZLC-03	0 45 90 135 180 225 270 315	0 7 20 16 10 5 5 5	0	0	-	48.8010708	-122.1681467	162	-	Elevation	0.994804

Table 2 - Topographic Shielding Input: CRONUS Earth Topographic Shielding Calculator v.2.1; http://cronus.cosmogenicnuclides.rocks/2.1/html/topo/. Samples indicated with an asterisk (*) were collected from the edge or "crest" of a boulder. Cosmogenic influence may be attenuated from self-shielding effects.

Sample Name	Quartz Mass (g)	Mass of ^{9}Be Added (µg)*	AMS Cathode Number	Uncorrected ^{10}Be/^{9}Be Ratio**	Uncorrected ^{10}Be/^{9}Be Ratio Uncertainty**	Background-Corrected ^{10}Be/^{9}Be Ratio	Background-Corrected ^{10}Be/^{9}Be Ratio Uncertainty	10Be Concentration (atoms g^{-1})	^{10}Be Concentration Uncertainty (atoms g^{-1})
RHC-01	20.6385	250.0	162253	5.567E-14	4.298E-15	5.362E-14	4.347E-15	4.341E+04	3.519E+03
RHC-02	18.8052	249.4	162254	3.101E-14	2.917E-15	2.895E-14	2.989E-15	2.565E+04	2.648E+03
RHC-03	12.4904	249.7	162256	1.857E-14	3.182E-15	1.651E-14	3.248E-15	2.205E+04	4.338E+03
RHC-06	21.7989	250.1	162267	2.681E-14	2.647E-15	2.475E-14	2.726E-15	1.897E+04	2.090E+03
MFN-02	12.6432	250.0	162257	2.529E-14	2.628E-15	2.323E-14	2.708E-15	3.070E+04	3.578E+03
MFN-03	13.3644	249.3	162258	2.650E-14	2.740E-15	2.445E-14	2.817E-15	3.047E+04	3.511E+03
MFN-04	22.0189	248.9	162259	5.648E-14	4.068E-15	5.443E-14	4.120E-15	4.111E+04	3.112E+03
MFN-05	23.1533	249.3	162260	7.090E-14	4.440E-15	6.884E-14	4.487E-15	4.952E+04	3.228E+03
MF-01	22.1496	250.6	162261	3.020E-14	2.767E-15	2.814E-14	2.843E-15	2.128E+04	2.150E+03
MF-02	21.8967	249.7	162263	2.971E-14	2.622E-15	2.765E-14	2.701E-15	2.107E+04	2.059E+03
MF-03	17.6431	249.4	162264	7.561E-15	1.407E-15	5.503E-15	1.551E-15	5.197E+03	1.465E+03
MF-04	21.4929	250.0	162265	3.805E-14	3.490E-15	3.599E-14	3.551E-15	2.797E+04	2.759E+03
MF-05	21.9845	249.7	162266	5.192E-14	3.608E-15	4.986E-14	3.666E-15	3.785E+04	2.783E+03
VZLC-01	21.8862	250.4	162269	1.575E-14	2.212E-15	1.369E-14	2.306E-15	1.046E+04	1.763E+03
VZLC-02	21.9733	249.0	162270	1.308E-14	1.808E-15	1.103E-14	1.922E-15	8.350E+03	1.456E+03
VZLC-03	16.7385	248.9	162271	1.037E-14	1.908E-15	8.315E-15	2.016E-15	8.261E+03	2.003E+03

*^{9}Be was added through a beryl carrier made at University of Vermont with a concentration of 304 µg mL^{-1}.

**Isotopic analysis was conducted at PRIME Laboratory; ratios were normalized against standard 07KNSTD3110 with an assumed ratio of 2850 x 10-15 (Nishiizumi et al., 2007).

Table 3 - Corrected and uncorrected ^{10}Be concentrations for CRN exposure dating samples. Table prepared by University of Vermont - Community Cosmogenic Facility (UVM-CCF).

```
RHC-01 48.8841066 -122.1458748 138 std 6.0 2.65 0.9851 0 2020;
RHC-01 Be-10 quartz 4.341E+04 3.519E+03 07KNSTD;
RHC-02 48.8841806 -122.1458135 139 std 3.0 2.65 0.9973 0 2020;
RHC-02 Be-10 quartz 2.565E+04 2.648E+03 07KNSTD;
RHC-03 48.8837500 -122.1447000 149 std 2.0 2.65 0.9637 0 2020;
RHC-03 Be-10 quartz 2.205E+04 4.338E+03 07KNSTD;
MFN-02 48.8300593 -122.0923034 757 std 3.0 2.65 0.9738 0 2020;
MFN-02 Be-10 quartz 3.070E+04 3.578E+03 07KNSTD;
MFN-03 48.8295946 -122.0921602 756 std 2.0 2.65 0.9667 0 2020;
MFN-03 Be-10 quartz 3.047E+04 3.511E+03 07KNSTD;
MFN-04 48.8317389 -122.1204972 200 std 2.0 2.65 0.9840 0 2020;
MFN-04 Be-10 quartz 4.111E+04 3.112E+03 07KNSTD;
MFN-05 48.8294717 -122.1217763 186 std 4.0 2.65 0.9926 0 2020;
MFN-05 Be-10 quartz 4.952E+04 3.228E+03 07KNSTD;
MF-01 48.9114468 -122.0540288 390 std 2.0 2.65 0.9848 0 2020;
MF-01 Be-10 quartz 2.128E+04 2.150E+03 07KNSTD;
```

```
MF-02 48.9108500 -122.0541833 402 std 3.0 2.65 0.9912 0 2020;
MF-02 Be-10 quartz 2.107E+04 2.059E+03 07KNSTD;
MF-03 48.9067883 -122.0510944 544 std 4.0 2.65 0.9905 0 2020;
MF-03 Be-10 quartz 5.197E+03 1.465E+03 07KNSTD;
MF-04 48.9231587 -122.0588639 176 std 3.0 2.65 0.9949 0 2020;
MF-04 Be-10 quartz 2.797E+04 2.759E+03 07KNSTD;
MF-05 48.9226995 -122.0599739 176 std 2.0 2.65 0.9950 0 2020;
MF-05 Be-10 quartz 3.785E+04 2.783E+03 07KNSTD;
RHC-06 48.8795616 -122.1456477 125 std 1.5 2.65 0.9870 0 2020;
RHC-06 Be-10 quartz 1.897E+04 2.090E+03 07KNSTD;
VZLC-01 48.7997180 -122.1656863 142 std 2.0 2.65 0.9498 0 2020;
VZLC-01 Be-10 quartz 1.046E+04 1.763E+03 07KNSTD;
VZLC-02 48.8003511 -122.1667259 155 std 1.5 2.65 0.9889 0 2020;
VZLC-02 Be-10 quartz 8.350E+03 1.456E+03 07KNSTD;
VZLC-03 48.8010708 -122.1681467 162 std 1.5 2.65 0.9943 0 2020;
VZLC-03 Be-10 quartz 8.261E+03 2.003E+03 07KNSTD;
```

Production rate calibration:

```
06-PUG-003-COL 48.01962 -122.42713 60 std  2.2 2.70 1.0000 9.68e-05 2006;
06-PUG-003-COL true_t WHIDBEY 15500 500;
06-PUG-003-COL Be-10 quartz 7.162e+04 1.354e+03 07KNSTD;
```

Table 4 – Raw data input and production rate calibration data used for the online exposure age calculator of Balco (2008). Enter in Production Rate Calibration Input page (https://hess.ess.washington.edu/math/v3/v3_cal_in.html) http://calibration.ice-d.org/site/WHIDBEY.

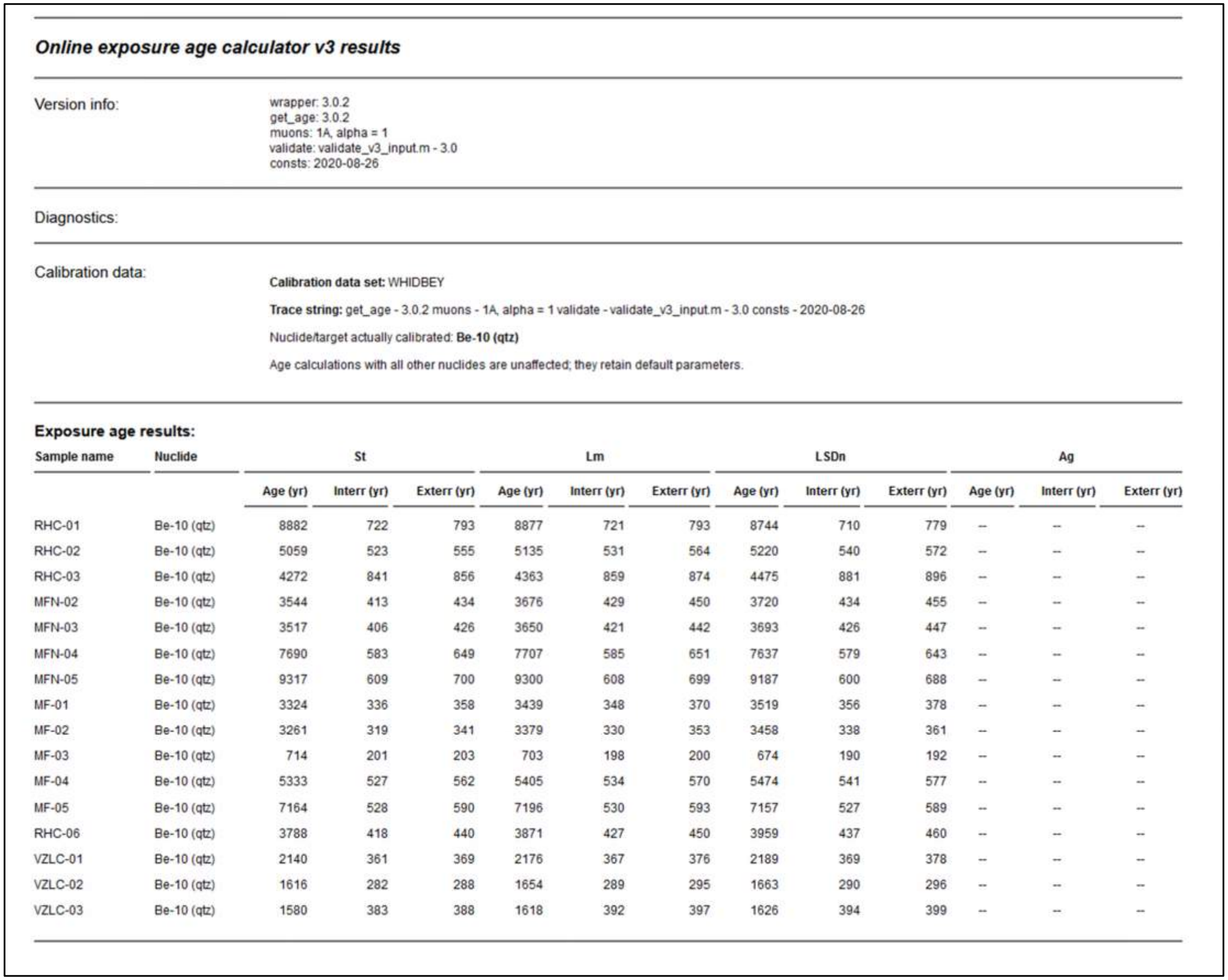

Online exposure age calculator v3 results

Version info:

wrapper: 3.0.2
get_age: 3.0.2
muons: 1A, alpha = 1
validate: validate_v3_input.m - 3.0
consts: 2020-08-26

Diagnostics:

Calibration data:

Calibration data set: WHIDBEY

Trace string: get_age - 3.0.2 muons - 1A, alpha = 1 validate - validate_v3_input.m - 3.0 consts - 2020-08-26

Nuclide/target actually calibrated: **Be-10 (qtz)**

Age calculations with all other nuclides are unaffected; they retain default parameters.

Exposure age results:

Sample name	Nuclide	St			Lm			LSDn			Ag		
		Age (yr)	Interr (yr)	Exterr (yr)	Age (yr)	Interr (yr)	Exterr (yr)	Age (yr)	Interr (yr)	Exterr (yr)	Age (yr)	Interr (yr)	Exterr (yr)
RHC-01	Be-10 (qtz)	8882	722	793	8877	721	793	8744	710	779	--	--	--
RHC-02	Be-10 (qtz)	5059	523	555	5135	531	564	5220	540	572	--	--	--
RHC-03	Be-10 (qtz)	4272	841	856	4363	859	874	4475	881	896	--	--	--
MFN-02	Be-10 (qtz)	3544	413	434	3676	429	450	3720	434	455	--	--	--
MFN-03	Be-10 (qtz)	3517	406	426	3650	421	442	3693	426	447	--	--	--
MFN-04	Be-10 (qtz)	7690	583	649	7707	585	651	7637	579	643	--	--	--
MFN-05	Be-10 (qtz)	9317	609	700	9300	608	699	9187	600	688	--	--	--
MF-01	Be-10 (qtz)	3324	336	358	3439	348	370	3519	356	378	--	--	--
MF-02	Be-10 (qtz)	3261	319	341	3379	330	353	3458	338	361	--	--	--
MF-03	Be-10 (qtz)	714	201	203	703	198	200	674	190	192	--	--	--
MF-04	Be-10 (qtz)	5333	527	562	5405	534	570	5474	541	577	--	--	--
MF-05	Be-10 (qtz)	7164	528	590	7196	530	593	7157	527	589	--	--	--
RHC-06	Be-10 (qtz)	3788	418	440	3871	427	450	3959	437	460	--	--	--
VZLC-01	Be-10 (qtz)	2140	361	369	2176	367	376	2189	369	378	--	--	--
VZLC-02	Be-10 (qtz)	1616	282	288	1654	289	295	1663	290	296	--	--	--
VZLC-03	Be-10 (qtz)	1580	383	388	1618	392	397	1626	394	399	--	--	--

Table 5 – Raw data output from the online exposure age calculator of Balco (2008) found at https://hess.ess.washington.edu/.

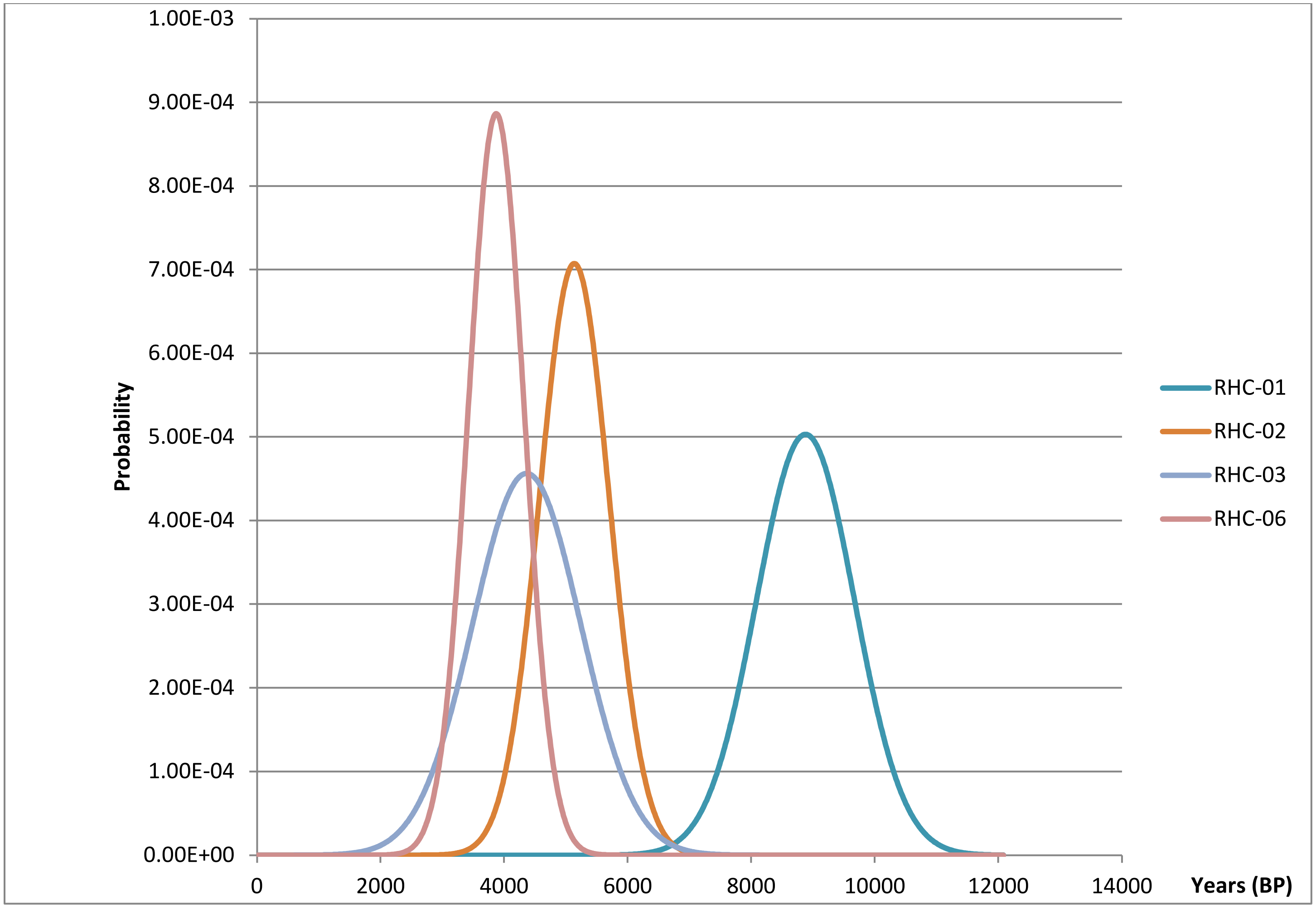

Figure 1 – Probability distribution functions of ^{10}Be-CRN samples collected from the Racehorse Creek landslide.

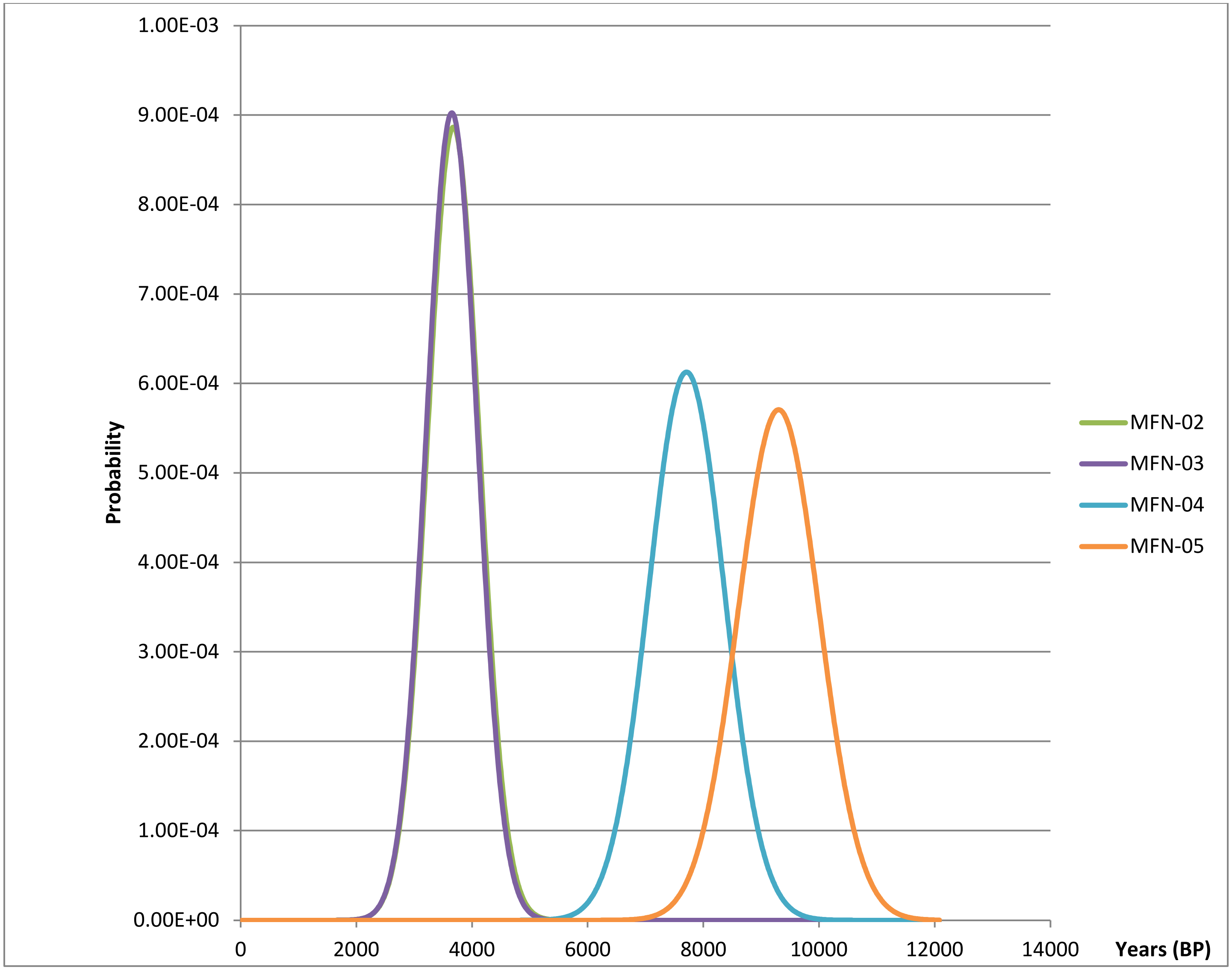

Figure 2 - Probability distribution functions of ^{10}Be-CRN samples collected from the Middle Fork landslide.

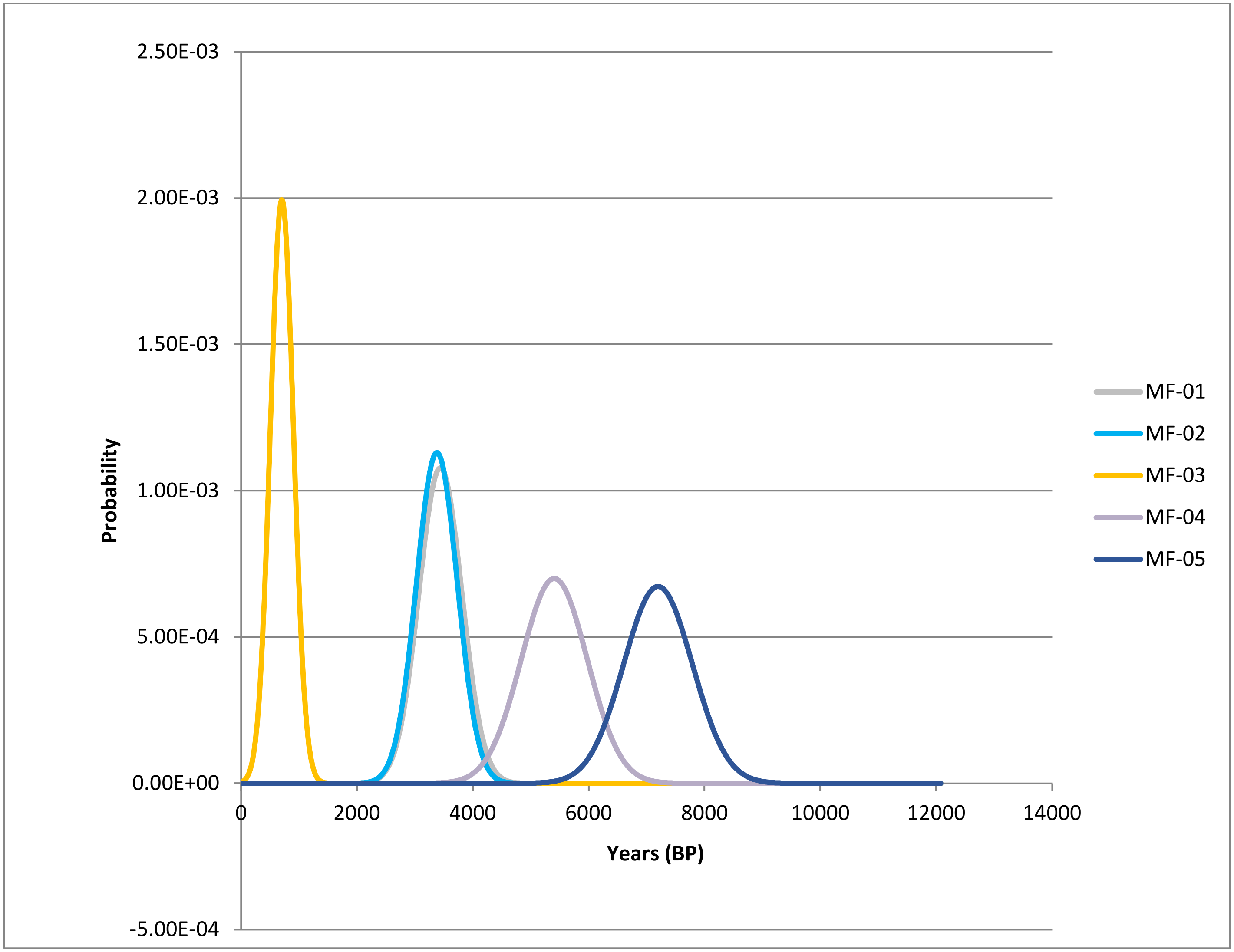

Figure 3 – Probability distribution functions of ^{10}Be-CRN samples collected from the Maple Falls landslide.

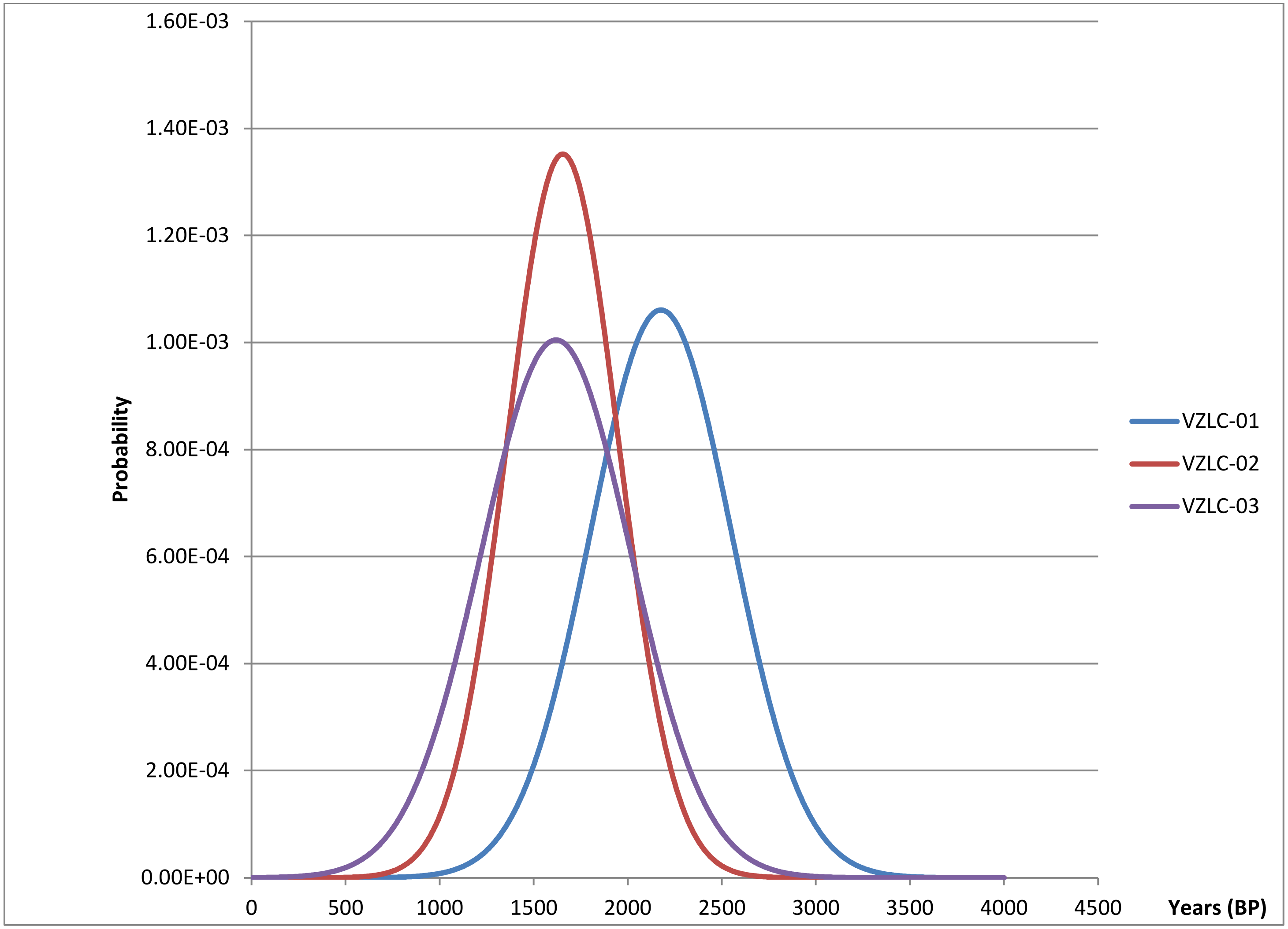

Figure 4 - Probability distribution functions of ^{10}Be-CRN samples from the Van Zandt Landslide Complex (VZLC).

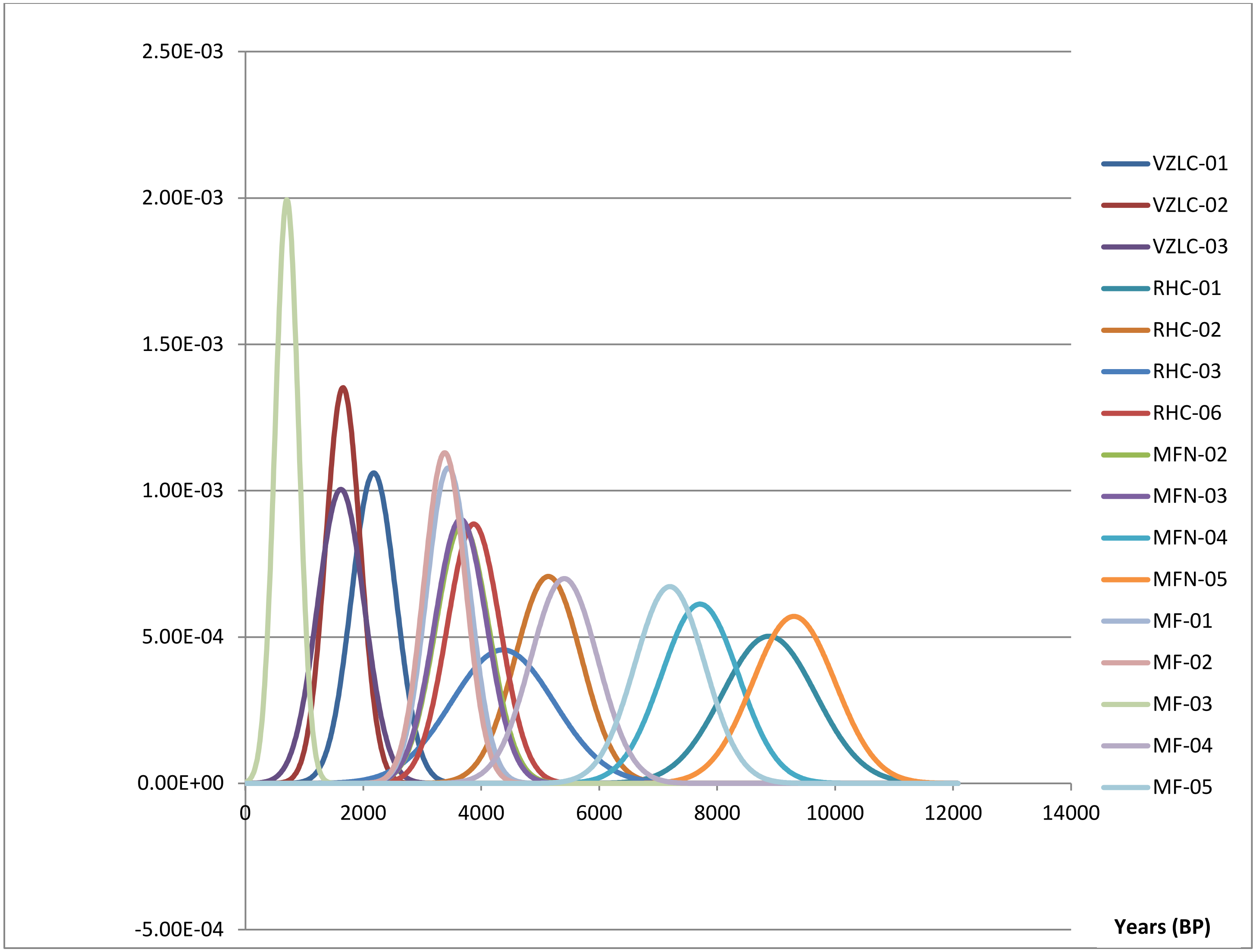

Figure 5 – Probability distribution functions of all collected ^{10}Be-CRN samples for this study.

Supplemental Images

SI 1. Racehorse Creek landslide debris exposure along the North Fork Nooksack River.

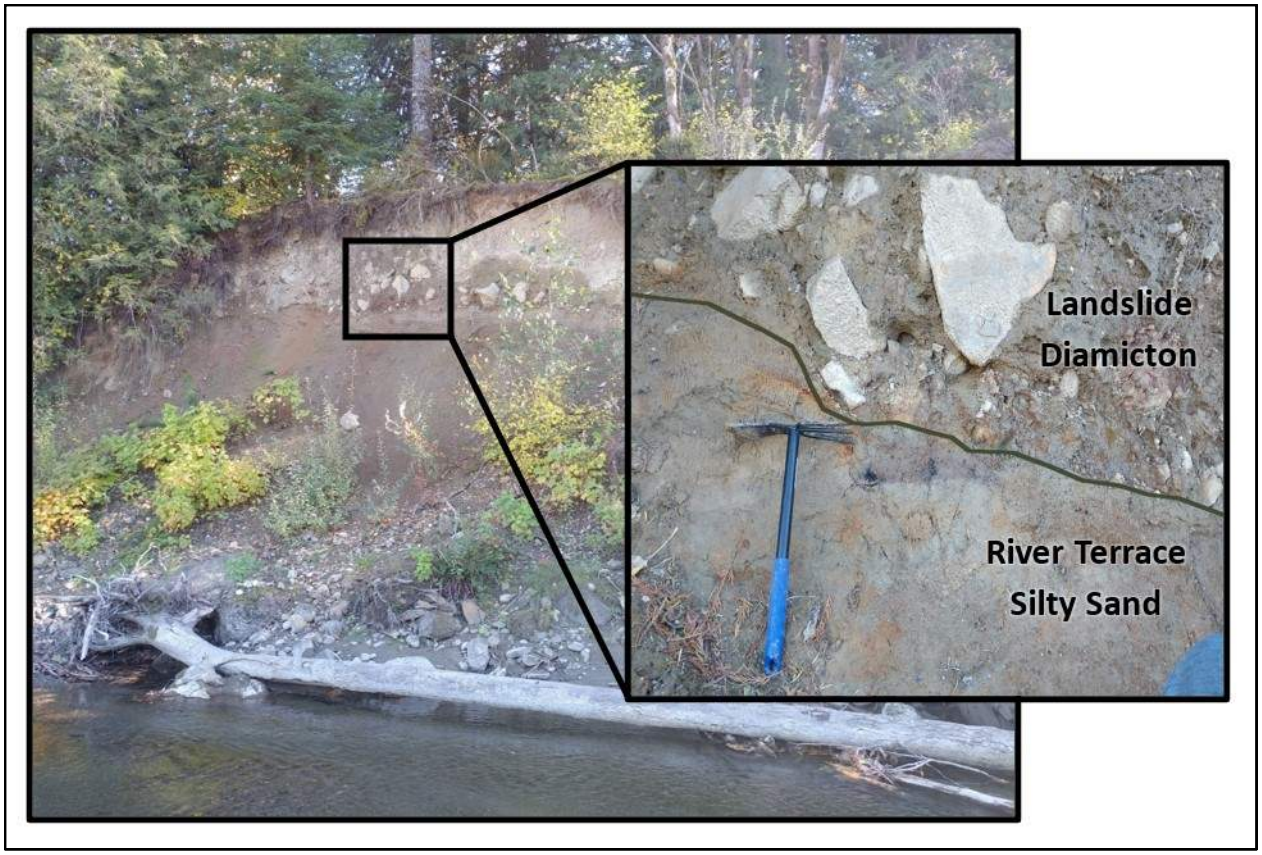

SI 2. Racehorse Creek landslide debris exposed along the North Fork Nooksack River. Landslide diamicton overlying Nooksack River alluvium.

SI 3. Boulder field at the Racehorse Creek Landslide deposit.

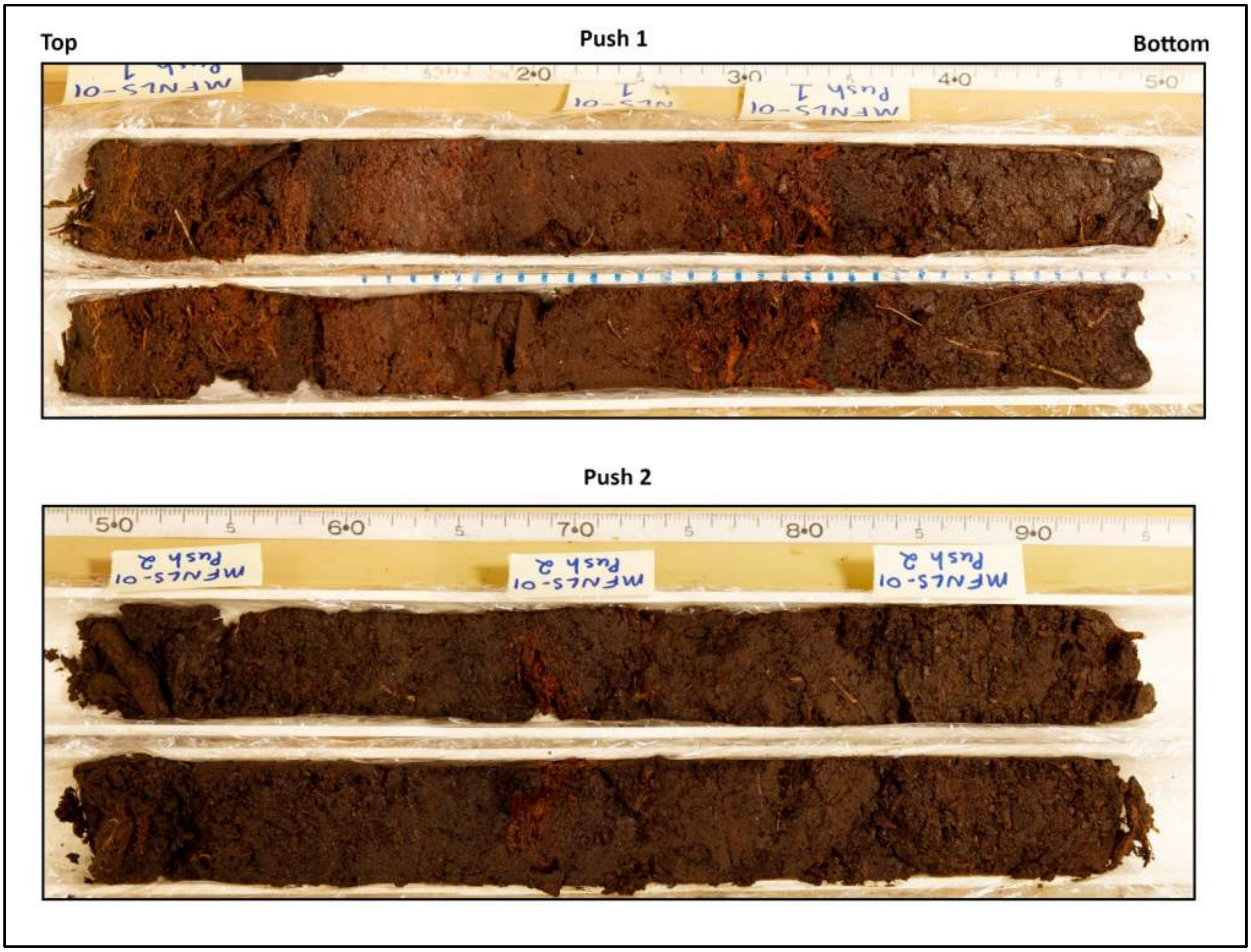

SI 4a. Bog sediment core MFNLS-01 collected from the Middle Fork bog. Pushes 1 and 2. Mud and organics.

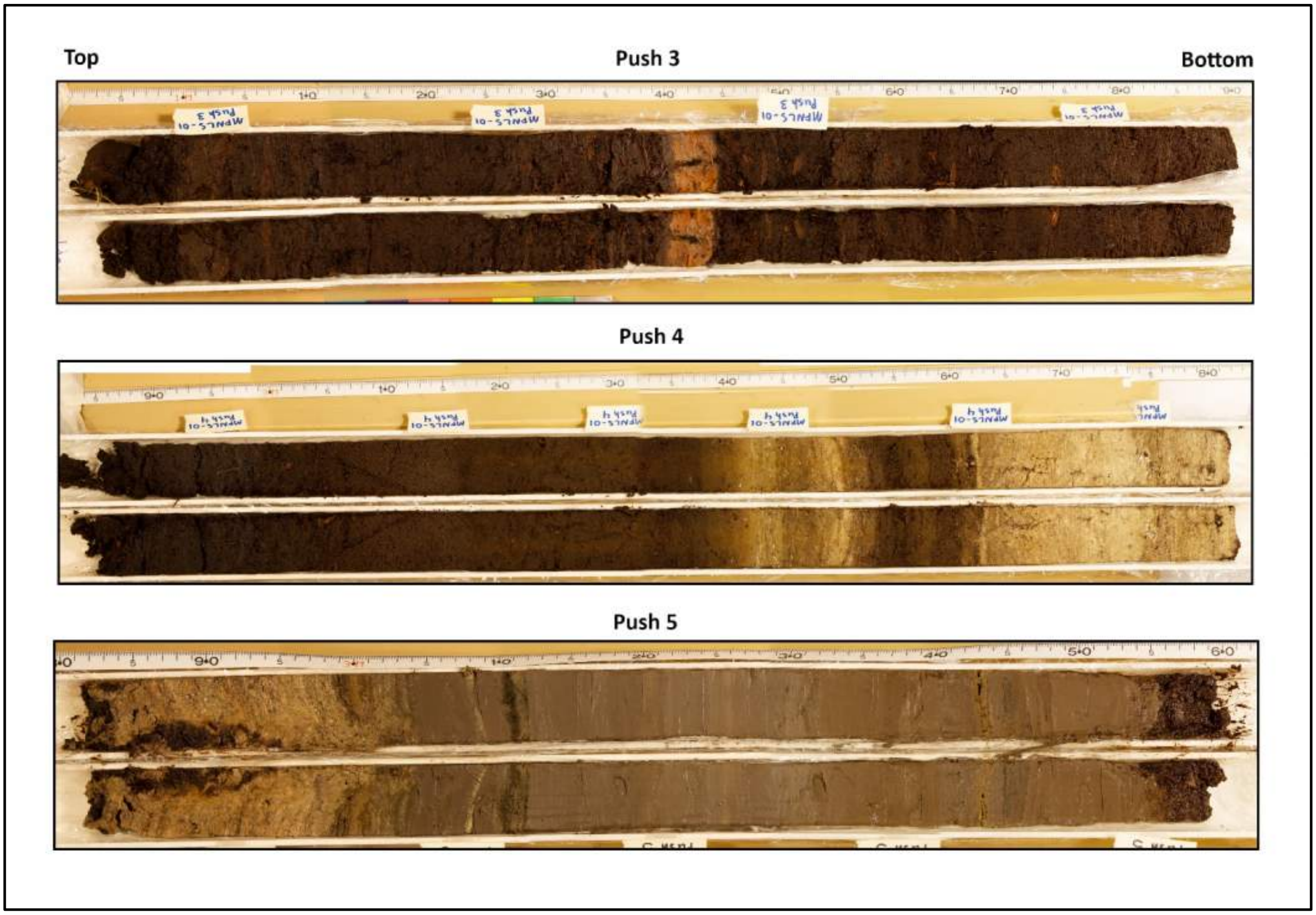

SI 4b. Bog sediment core MFNLS-01. Pushes 3 through 5. Pale-orange layer in Push 3 is Mazama ash. Push 4 transitions from organic-rich muds to whitish-tan carbonates and shell fragments. Push 5 transitions to thinly laminated silts and clays.

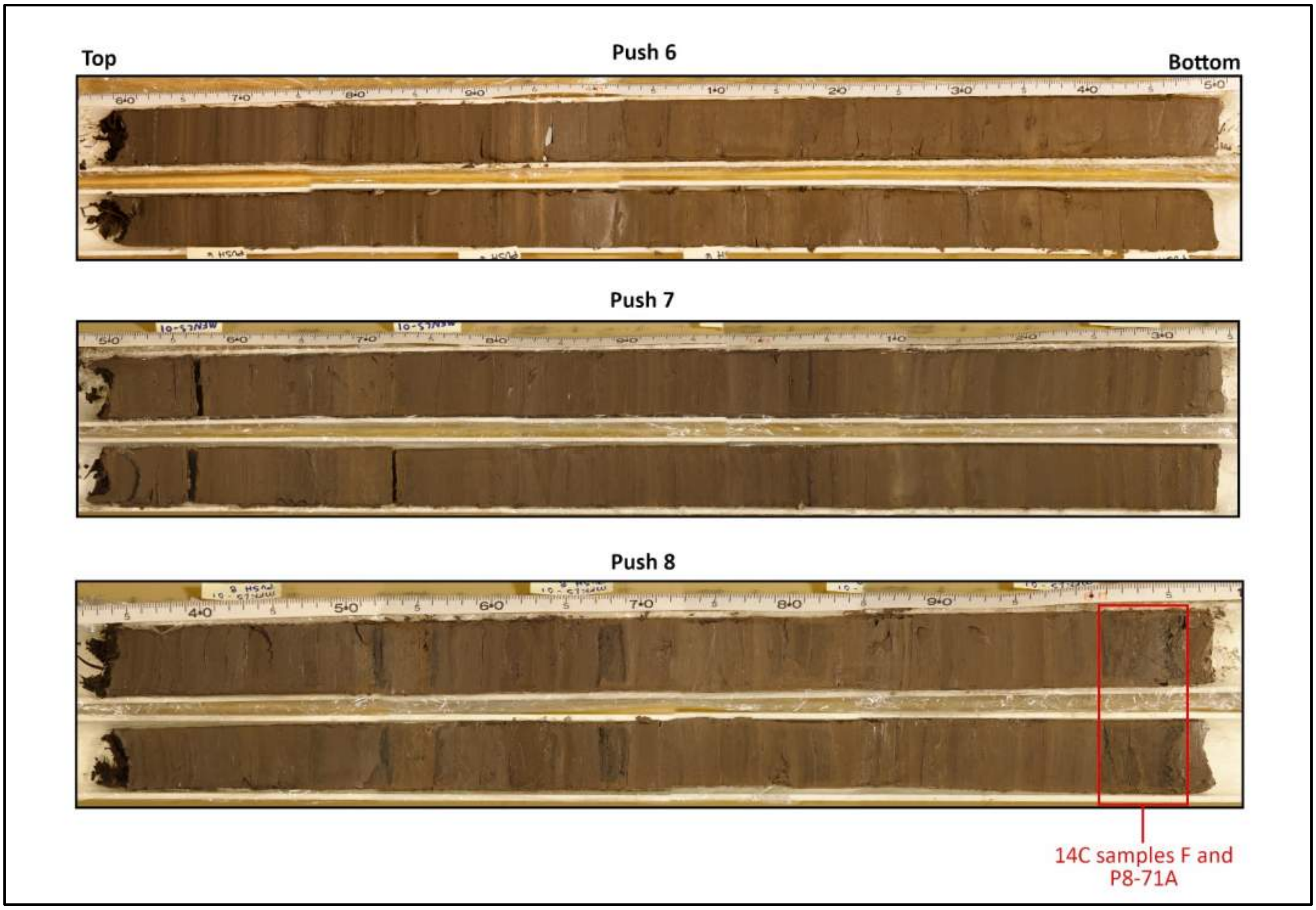

SI 4c. Bog sediment core MFNLS-01. Pushes 6 through 8. Roughly 3-meters of thinly laminated silts and clays. Radiocarbon samples F and P8-71A were collected from the bottom ~4 cm of the core.

SI 5. Bog sediment core MFNLS-01. Push 3 Mazama ash.

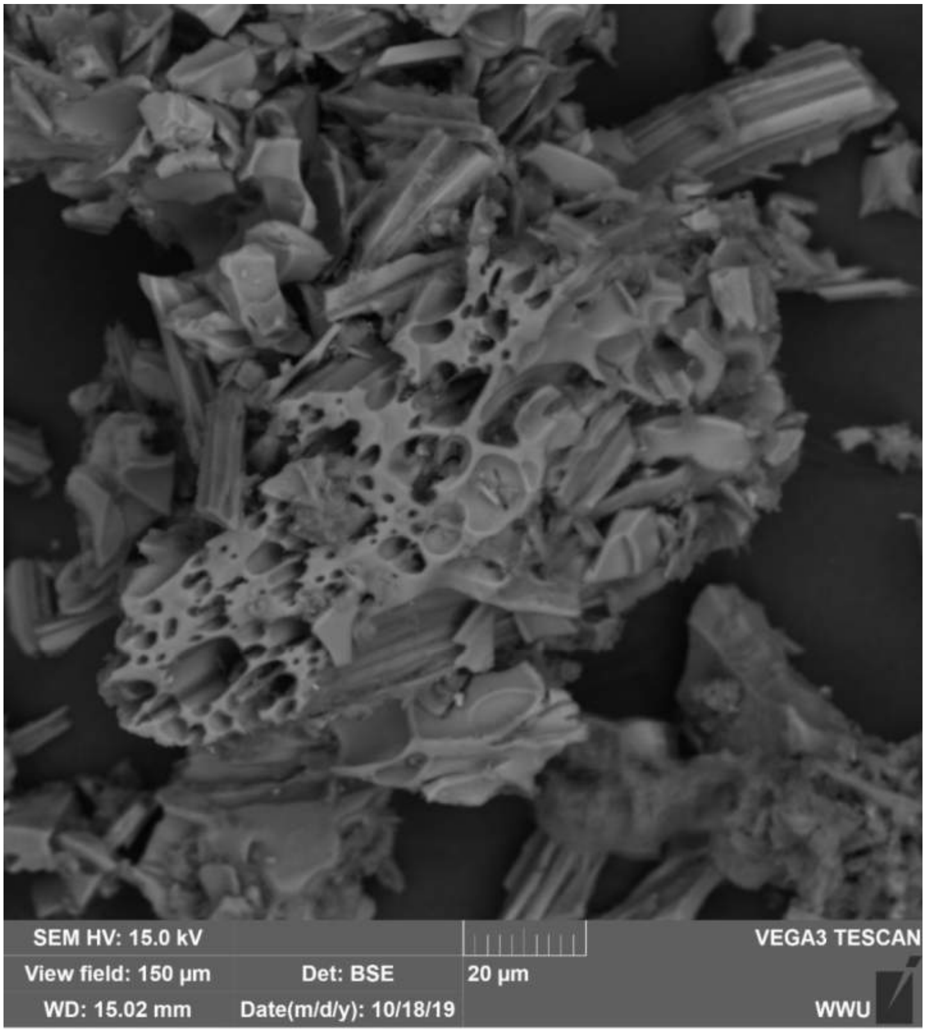

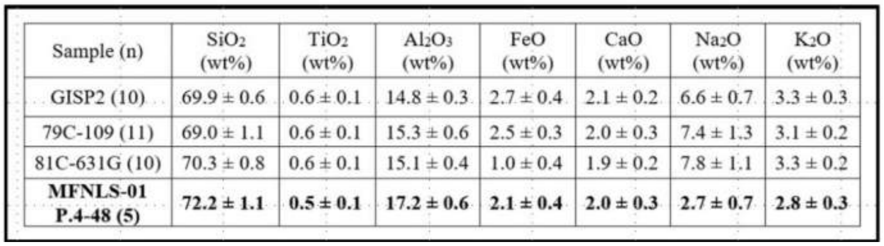

Sample (n)	SiO_2 (wt%)	TiO_2 (wt%)	Al_2O_3 (wt%)	FeO (wt%)	CaO (wt%)	Na_2O (wt%)	K_2O (wt%)
GISP2 (10)	69.9 ± 0.6	0.6 ± 0.1	14.8 ± 0.3	2.7 ± 0.4	2.1 ± 0.2	6.6 ± 0.7	3.3 ± 0.3
79C-109 (11)	69.0 ± 1.1	0.6 ± 0.1	15.3 ± 0.6	2.5 ± 0.3	2.0 ± 0.3	7.4 ± 1.3	3.1 ± 0.2
81C-631G (10)	70.3 ± 0.8	0.6 ± 0.1	15.1 ± 0.4	1.0 ± 0.4	1.9 ± 0.2	7.8 ± 1.1	3.3 ± 0.2
MFNLS-01 P.4-48 (5)	**72.2 ± 1.1**	**0.5 ± 0.1**	**17.2 ± 0.6**	**2.1 ± 0.4**	**2.0 ± 0.3**	**2.7 ± 0.7**	**2.8 ± 0.3**

SI 6. SEM imagery of a sample of Mazama ash collected from sediment core MFNLS-01. Table displaying compositional analyses of major oxides for Mazama ash samples collected from various cores (adapted from Zdanowics et al., 1999). The oxide composition of the ash collected from MFNLS-01 (bold) aligns with published literature from Zdanowics et al., 1999.

SI 7. Debris exposure in the Middle Fork landslide along the Middle Fork Nooksack River at Site X (Figure 3).

SI 8. Middle Fork lahar deposit overlying landslide debris of the Middle Fork landslide at Site Y (Figure 3).

SI 9. White ash layer overlying landslide debris of the Middle Fork landslide along the east bank of the Middle Fork River (south of Site X; Figure 3). Mazama ash confirmed through SEM-EDX major oxide analysis.

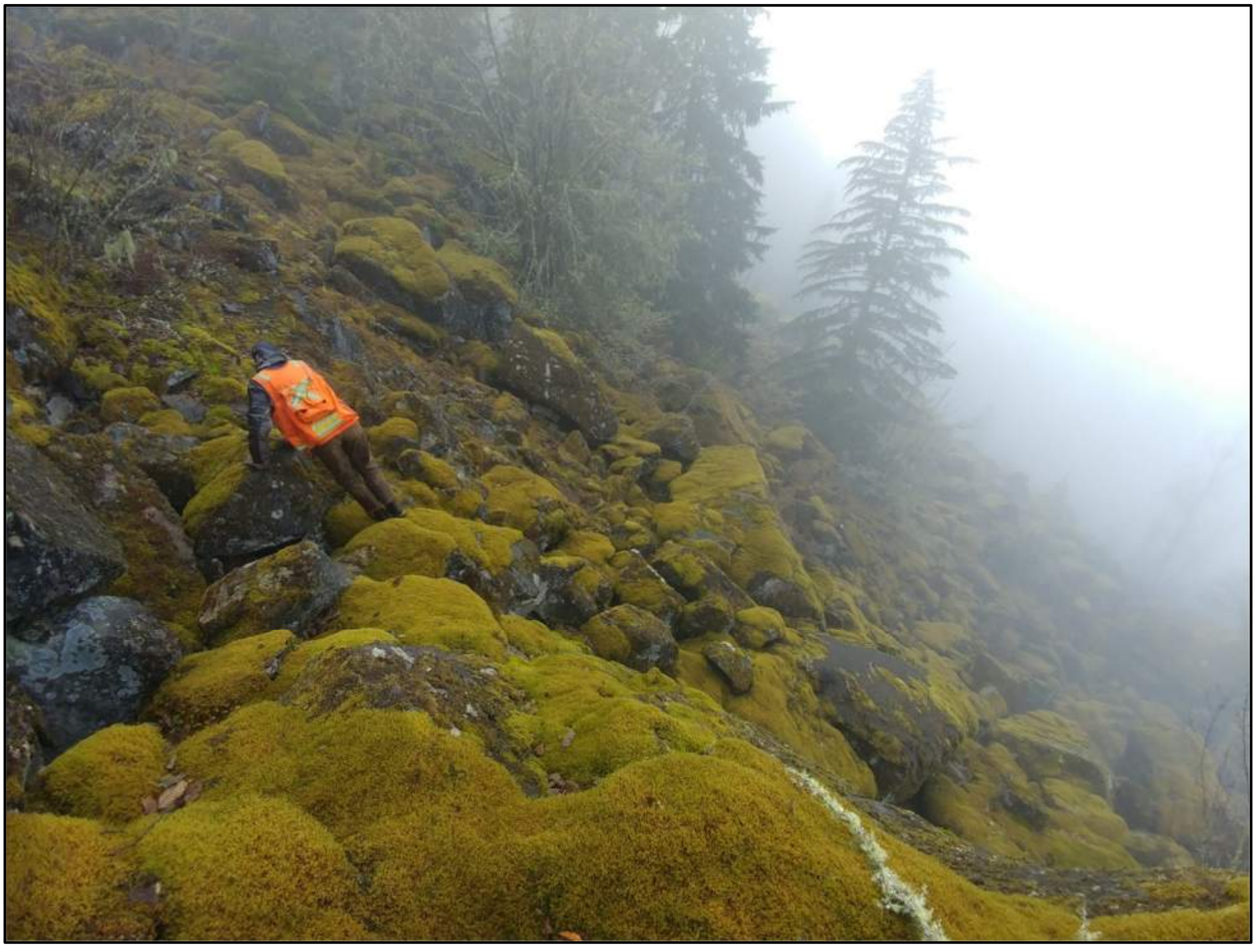

SI 10. Mossy boulder field near the headwall of the Maple Falls landslide.

SI 11. CRN boulder RHC-01.

SI 12. CRN boulder RHC-02.

SI 13. CRN boulder RHC-03.

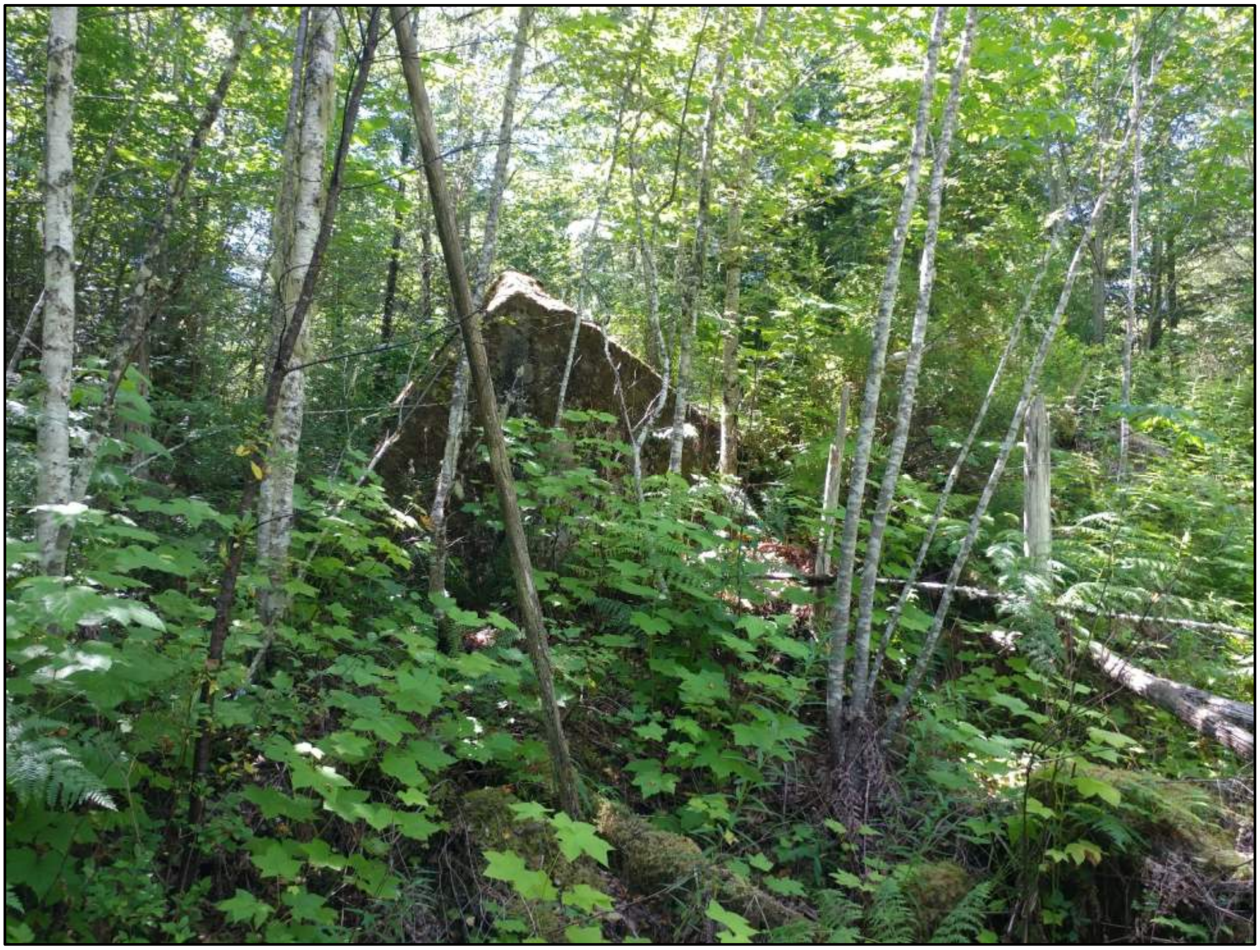

SI 14. CRN boulder RHC-06.

SI 15. CRN boulder MFN-02.

SI 16. CRN boulder MFN-03.

SI 17. CRN boulder MFN-04.

SI 18. CRN boulder MFN-05.

SI 19. River exposure of Maple Falls landslide debris along the North Fork Nooksack River.

SI 20. CRN boulder MF-01.

SI 21. CRN boulder MF-02.

SI 22. CRN boulder MF-03.

SI 23. CRN boulder MF-04.

SI 24. CRN boulder MF-05.

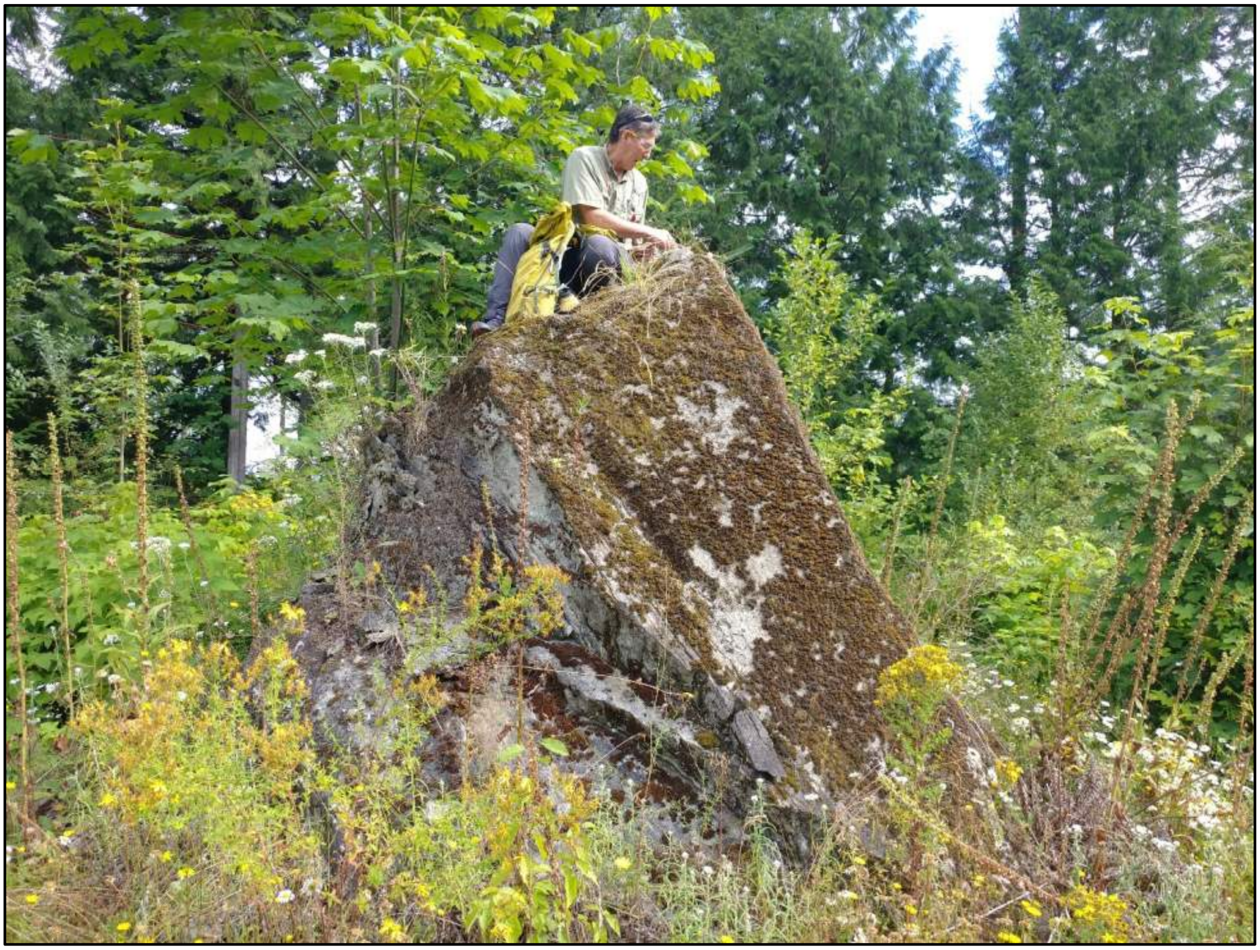

SI 25. CRN boulder VZLC-01.

SI 26. CRN boulder VZLC-02.

SI 27. CRN boulder VZLC-03.

SI 28. Source hollow for the 2009 Racehorse Creek landslide event.